# Carbohydrate-based Nanomaterials for Imaging and Drug Delivery

Inaugural-Dissertation
to obtain the academic degree
Doctor rerum naturalium (Dr. rer. nat.)

submitted to the Department of Biology, Chemistry and Pharmacy
of Freie Universität Berlin

by

Silvia Varela Aramburu

from Castellón de la Plana, Spain

March 2018

This work was performed between October 2013 and November 2017 under the supervision of Prof. Dr. Peter H. Seeberger in the Department of Biomolecular Systems, Max Planck Institute of Colloids and Interfaces Potsdam, and the Institute of Chemistry and Biochemistry, Freie Universität Berlin.

1st Reviewer: Prof. Dr. Peter H. Seeberger

2nd Reviewer: Prof. Dr. Rainer Haag

Date of defense: 9th July, 2018

# Declaration

This is to certify that the entire work in this thesis has been carried out by Ms. Silvia Varela Aramburu. The assistance and help received during the course of investigation have been fully acknowledged.

---------- ----------

(Date, Place) (Signature)

# Acknowledgements

I foremost want to express my gratitude to Prof. Dr. Peter H. Seeberger for providing me the opportunity to work in his group, and for his trust, support and supervision.

I am also grateful to Prof. Dr. Rainer Haag for agreeing to review this thesis.

I want to thank all former and current members of the Nano/Carbohydrate Materials group, especially my boss Dr. Martina Delbianco for her patience, fruitful discussions, and Thursdays afternoon, Dr. Priya Bharate, Zhou Ye and Dr. Chian-Hui Lai for their invaluable help in the lab and for creating a very pleasant working atmosphere.

I would like to thank Dr. Oren Moscovitz for his support in the biology part of this thesis and for making science exciting. I also want to thank Suzan Almeida, Rebeca Fortes, Andreia Marta and Soeun Gim for being part of the malaria project.

I want to acknowledge my collaborators from external institutions: Dr. Richard Wirth (Deutsches GeoForschungsZentrum) for HRTEM analysis, Dr. Holger Stephan, Dr. Kritee Pant and Garima Singh (Helmholtz Zentrum Dresden), for the biodistribution studies, Prof. Dr. Luisa de Cola, Dr. Leana Travaglini, Dr. Valentina Giglio, Dr. Laura Maggini and John Ddungu (ISIS, Strasbourg) for providing different nanomaterials, and Dr. Nishith Gupta and Laura Radtke (Humboldt University) for the *T. gondii* studies

I want to thank the technicians Uwe Vogel, Eva Settels, Olaf Niemeyer, Jeannette Steffen, Rona Pitschke and Heike Runge for the help with experiments. I am also grateful to Dorothee Böhme for the help with administrative tasks.

I would like to thank Dr. Martina Delbianco, Ankita Malik, Dr. Oren Moscovitz, Dr. Priya Bharate and Dr. Jamal Malik for proofreading parts of this thesis. I also want to thank Dr. Bartholomäus Pieber for translating the summary of this thesis.

I am deeply grateful to all my colleagues and friends of the BMS department, especially Ankita, Antonella, Maria A., Andreia A., Kathir, Bart, Stella, Matt, Jamal, Pietro, Rich, Mauro, Fei-Fei, Mónica, Alonso, Andrew, Renée, Jiawei, Hyun Il and Mara.

Last but not least, I want to express my deepest gratitude to my parents, my sister Ana, Tristán and especially Martín for all his help, patience and constant support during this period.

# List of publications

## A) Scientific publications

1. Straightforward and robust synthesis of monodisperse surface-functionalized gold nanoclusters. S. Varela-Aramburu, R. Wirth, C.-H. Lai, G. Orts-Gil, P. H. Seeberger, *Beilstein J. Nanotechnol.* 2016, **7**, 1278–1283.

2. Carbohydrates in supramolecular chemistry. M. Delbianco, P. Bharate, S. Varela-Aramburu, P. H. Seeberger, *Chem. Rev.* 2016, **116**, 1693–1752.

3. Reshaping silica particles: Mesoporous nanodiscs for bimodal delivery and improved cellular uptake. V. Giglio, S. Varela-Aramburu, L. Travaglini, F. Fiorini, P. H. Seeberger, L. Maggini, L. de Cola, *Chem. Eng. J.* 2018, **340**, 148-154.

4. Analysis of carbohydrate−carbohydrate interactions using sugar-functionalized silicon nanoparticles for cell imaging. C.-H. Lai, J. Hütter, C.-W. Hsu, H. Tanaka, S. Varela-Aramburu, L. De Cola, B. Lepenies, P. H. Seeberger, *Nano Lett.* 2016, **16**, 807−811.

5. Tumor-targeted drug delivery with mannose-functionalized nanoparticles self-assembled from amphiphilic β-cyclodextrins. Z. Ye, Q. Zhang, S. Wang, P. Bharate, S. Varela-Aramburu, M. Lu, P. H. Seeberger, J. Yin, *Chem. Eur. J.* 2016, **22**, 15216 – 15221.

## B) Scientific Conferences and Symposia

1. COST Multiglyconano Symposium, Bangor, United Kingdom (2015): "One-pot synthesis of stable, non-toxic glycosylated gold nanoclusters" (Oral presentation + Poster).

2. NanoTracking Symposium, Lipari, Italy (2015): "Synthesis of ultrasmall glycosylated nanoparticles" (Oral presentation).

3. Functional Biointerfaces International Symposium, Berlin, Germany (2016): "Straightforward and robust synthesis of monodisperse surface-functionalized gold nanoclusters" (Poster).

4. NanoTracking Symposium, Dresden, Germany (2016): “Synthesis, radiolabeling and cellular uptake of carbohydrate-based gold nanoclusters” (Oral presentation).

5. RIKEN - Max Planck Symposium, Berlin, Germany (2016): “Straightforward and robust synthesis of monodisperse surface-functionalized gold nanoclusters for biomedical applications” (Poster).

# Table of contents

# List of abbreviations

| | |
|---|---|
| APTES | (3-aminopropyl)triethoxysilane |
| AuNPs | Gold nanoparticles |
| BBB | Blood brain barrier |
| BTPS | Bis(triethoxysilyl-propyl)disulphide |
| CCIs | Carbohydrate-carbohydrate interactions |
| CM | Culture medium |
| ConA | Concanavalin A |
| CPIs | Carbohydrate-protein interactions |
| CSLM | Confocal scanning laser microscopy |
| CTAB | Cetyltrimethylammonium bromide |
| DAPI | 4',6-diamidino-2-phenylindole |
| DIC | Differential interference contrast |
| DIPEA | *N,N*-Diisopropylethylamine |
| DLS | Dynamic light scattering |
| DMF | Dimethylformamide |
| DMSO | Dimethylsulfoxide |
| DNA | Deoxyribonucleic acid |
| DOXO | Doxorubicin |
| EDC | *N*-ethyl-*N*'-(diethylaminopropyl)-carbodiimide |
| EDTA | Ethylenediaminetetraacetic acid |
| EM | Electron microscopy |

| | |
|---|---|
| ESEM | Environmental scanning electron microscopy |
| EtOAc | Ethyl acetate |
| EtOH | Ethanol |
| FA | Folic acid |
| FACS | Fluorescent-activated cell sorting |
| FBS | Fetal bovine serum |
| FITC | Fluorescein isothiocyanate |
| FTIR | Fourier transform infrared |
| Gal | Galactose |
| Glc | Glucose |
| GPI | Glycosylphosphatidylinositol |
| GSH | Glutathione |
| HEPES | 4-(2-hydroxyethyl)piperazine-1-ethanesulfonic acid |
| Hex | Hexane |
| HFF | Human foreskin fibroblast |
| ICP-AES | Inductively coupled plasma atomic emission spectrometer |
| IR | Infrared |
| iRBCs | Infected red blood cells |
| KSAc | Potassium thioacetate |
| MACS | Magnetic-activated cell sorting |
| Man | Mannose |
| MeOH | Methanol |
| MRI | Magnetic resonance imaging |

| | |
|---|---|
| MSNs | Mesoporous silica nanoparticles |
| NCs | Gold nanoclusters |
| NHS | *N*-hydroxysuccinimide |
| NIR | Near infrared |
| NMR | Nuclear magnetic resonance |
| NOTA | 1,4,7-triazacyclononane-*N,N',N''* triacetic acid |
| NPs | Nanoparticles |
| NR | Nile red |
| OTACl | Octadecyltrimethylammonium chloride |
| PBS | Phosphate-buffered saline |
| PET | Positron electron tomography |
| PFA | Paraformaldehyde |
| RBCs | Red blood cells |
| RhB | Rhodamine B |
| RT | Room temperature |
| SAM | Self-assembled monolayer |
| SAXS | Small-angle X-ray scattering |
| SEM | Scanning electron microscopy |
| STEM | Scanning transmission electron microscopy |
| Sulfo-NHS | *N*-hydroxysulfosuccinimide |
| TEM | Transmission electron microscopy |
| TEOS | Tetraethyl orthosilicate |
| THPC | Tetrakis(hydroxymethyl)phosphonium chloride |
| X | |

| | |
|---|---|
| TLC | Thin layer chromatography |
| TMOS | Tetramethyl orthosilicate |
| UV | Ultraviolet |
| WHO | World health organization |
| XPS | X-ray photoelectron spectroscopy |

# Summary

As glycans are exposed on the surface of living cells, they are instrumental in biological processes such as cell-cell interactions, cell growth and cell differentiation. Multivalent carbohydrate-based nanomaterials help clarify these processes by mimicking the biological activity of carbohydrates. Moreover, nanomaterials have high potential for the imaging of diseases or biological processes, and can be further engineered for controlled and targeted drug delivery.

In the first part of this dissertation, a straightforward and robust room temperature one-pot synthesis of ultrasmall gold nanoparticles (2 nm) was developed using thio-glucose as a reducing and stabilizing agent (Chapter 2). The resultant monodisperse gold nanoparticles showed high stability and could be further functionalized using two different conjugation methods. These non-cytotoxic nanoclusters were radiolabeled for biodistribution studies *in vivo*, showing accumulation in almost all organs and clearance after 24 h.

The developed ultrasmall glycosylated gold nanoparticles were utilized to target the protozoan parasites *Plasmodium falciparum* and *Toxoplasma gondii* (Chapter 3). These parasites contain cysteine-rich domains in their surface proteins and could potentially capture gold nanoparticles through the well-known thiol-gold affinity. The gold nanoparticles were able to efficiently bind all the blood stages of *P. falciparum*, and both intracellular and extracellular *T. gondii*. Drug conjugation was performed for further *in vitro* and *in vivo* inhibition studies.

Flat discoidal mesoporous silica nanoparticles were synthesized and their biological applications were investigated (Chapter 4). These novel materials were internalized by HeLa cancer cells and showed increased intracellular drug delivery as compared to spherical analogues. Moreover, the introduction of cleavable disulfide moieties within the mesoporous silica framework enabled investigation of the impact of increasing cleavable bonds on the breakability and efficacy of these materials as nanovectors.

Multivalent glycosylated nanoparticles were synthesized to image biological processes (Chapter 5). Ultrasmall fluorescent silicon nanoparticles were functionalized with glucose

and a radiotracer in order to study the blood brain barrier crossing *in vivo*. Also, plasmonic gold nanoparticles were conjugated with a collection of carbohydrates for carbohydrate-protein interactions studies between green algae and cyanobacteria.

In conclusion, the design and engineering of glycosylated nanoparticles allows mimicking biological processes, obtaining unknown information through imaging techniques, and producing targeted nanocarriers for controlled drug delivery.

# Zusammenfassung

Glykane sind auf der Oberfläche von lebenden Zellen zu finden und dadurch maßgeblich für biologische Prozesse wie beispielsweise die Interaktion von Zellen, Zellwachstum und deren Differenzierung verantwortlich. Multivalente, kohlenhydrat-basierte Nanomaterialien ermöglichen Studien für eine bessere Klassifizierung dieser Prozesse, da diese die biologischen Aktivitäten von Kohlenhydraten imitieren können. Zusätzlich sind Nanomaterialien sehr vielversprechend für die Entwicklung von bildgebenden Verfahren für biologische Prozesse und können für gezielten Wirkstofftransport eingesetzt werden.

Im ersten Teil dieser Dissertation wird eine einfache und robuste Ein-Topf-Synthese von ultrakleinen Gold Nanopartikeln (2 nm) unter milden Bedingungen (Raumtemperatur) präsentiert, bei welcher Thioglukose sowohl als Reduktionsmittel als auch als Stabilisator verwendet wird (Kapitel 2). Die resultierenden monodispersen Gold-Nanopartikel zeichnen sich durch eine hohe Stabilität aus und konnten mit zwei verschiedenen Konjugationsmethoden modifiziert werden. Die nicht-zytotoxischen Nanokluster wurden mit radioaktiven Substanzen markiert und für *in vivo* Biodistributionsstudien verwendet, bei welchen eine Akkumulierung in fast allen Organen gefolgt von deren Ausscheidung innerhalb von 24 h beobachtet wurde.

Die ultrakleinen, glykosylierten Gold Nanopartikel wurden zum Targeting der protozoischen Parasiten *Plasmodium falciparum* und *Toxoplasma gondii* verwendet (Kapitel 3). Diese besitzen cysteinreiche Domänen in ihren Oberflächenproteinen wodurch aufgrund der hohen Affinität von Gold und Thiolen eine zielgerichtete Bindung möglich ist. Die Gold-Nanopartikel konnten alle Blutstadien von *P. falciparum,* sowie *T. gondii* (intra- und extrazelluläre) effizient binden. Des Weiteren wurden Wirkstoffkonjugate für *in vitro* und *in vivo* Inhibitionsstudien hergestellt.

Flache, scheibenförmige Nanopartikel aus mesoporösem Silica wurden hergestellt und auf deren biologische Anwendbarkeit getestet (Kapitel 4). Diese neuartigen Materialen wurden von HeLa Krebszellen internalisiert und zeigten einen besseren interzellulären Wirkstofftransport als deren sphärische Analoga. Der Einbau von Disulfideinheiten

innerhalb des mesoporösen Silica-Gerüsts ermöglichte die Untersuchung des Einflusses der steigenden Zahl von spaltbaren Bindungen auf die Brüchigkeit dieser Verbindungen und deren Einsetzbarkeit als Nanovektoren.

Die Entwicklung bildgebender Verfahren zum Studium biologischer Prozesse wurde anhand multivalenter glykosylierter Nanopartikel durchgeführt (Kapitel 5). Im speziellen wurden ultrakleine, fluoreszierende Silikon-Nanopartikel mit Glukose und einem Radiotracer funktionalisiert und für *in vivo* Untersuchungen zur Überwindung der Blut-Hirn-Schranke verwendet. Des Weiteren wurden plasmonische Gold-Nanopartikel mit einer Auswahl an Kohlenhydraten konjugiert, um Kohlenhydrat-Protein-Interaktionen zwischen grünen Algen und Cyanobakterien zu visualisieren.

Zusammenfassend wurde in der vorgelegten Arbeit gezeigt, dass glykosylierte Nanopartikel für die Nachahmung von biologischen Prozessen, die Entwicklung von bildgebenden Verfahren und für gezielten Wirkstofftransport eingesetzt werden können.

# 1. Introduction

## 1.1. Nanomaterials

Nanomaterials are materials that have at least one dimension between 1 and 100 nm.[1] In particular, nanoparticles (NPs) are objects in this size range that behave as a whole unit in terms of transport and properties. The size of NPs is comparable to the dimensions of biomolecules, such as glycans or proteins (Figure 1.1). Hence, the combination of nanomaterials with biomolecules allows for mimicking biological entities and understanding biological processes.[2]

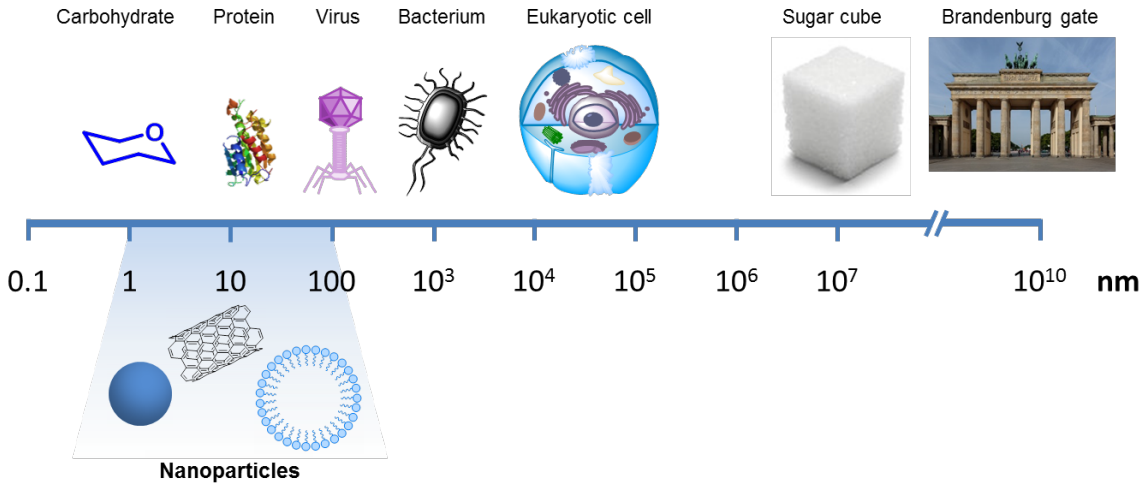


**Figure 1.1.** Nanoparticles have a size between 1 and 100 nm, which is comparable to the size of biomolecules.

Due to their size, nanomaterials differ significantly from both bulk materials and their atomic components, as they present high surface to volume ratio and quantum-size effects in the case of metal nanoparticles.[3-4] For spherical NPs, the specific surface area increases with decreasing diameter (Figure 1.2).[5] Since the specific surface area (the surface area of a material per unit of mass) increases, the number of atoms at the surface increases drastically as well, where for example in a 2-nm NPs, 70% of the atoms are located on the surface. For this reason, ultrasmall NPs (size range from 1 to 3 nm) have completely different physicochemical and pharmacokinetic features compared to larger nanoparticles

as the size becomes comparable to single molecules.[5-6] In addition to size, other properties like surface charge, material composition and shape have a strong influence in the pharmacokinetic properties and in renal clearance of ultrasmall NPs.[7]

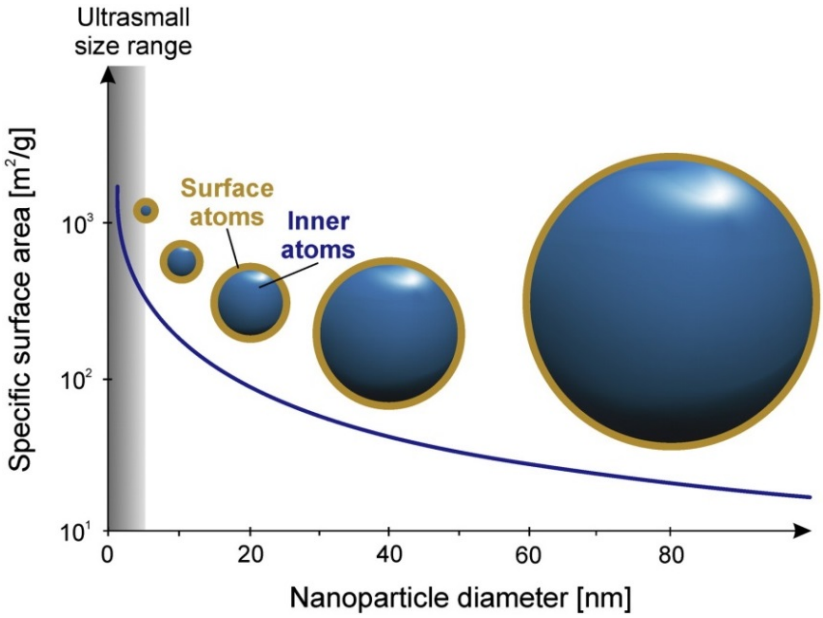


**Figure 1.2.** The specific surface area as well as the surface atoms of nanoparticles increases with decreasing diameter. Reprinted from Zarschler *et al.*[5] Copyright (2016), with permission from Elsevier.

## 1.1.1. Types of nanoparticles

Many different materials have been used to synthesize NPs for biomedical applications, such as metals (gold,[8] silver[9]), silica[10] and silicon[11], carbon (carbon nanotubes,[12] fullerenes,[13] graphene[14]), polymers[15] dendrimers,[16] magnetic,[17] or semiconductive materials[18].

### 1.1.1.1. Metal nanoparticles

Metal NPs, especially those based on gold, have very special photophysical properties due to the quantum-size effect, and are hence exploited in biotechnology applications. The quantum-size effect takes place in metal NPs when the de Broglie wavelength of the valence electrons is of the same order as the NP size. In this case, the NPs follow the rules of quantum mechanics as they behave as zero-dimensional quantum boxes.[19] When an electromagnetic field interacts with free conduction electrons of the NPs, the electrons start to oscillate in phase with the electromagnetic field inducing a dipole within the NP. To

compensate this dipole formation, a restoring force in the NP results in a resonance frequency, the so called surface plasmon resonance (Figure 1.3).[20] This oscillation depends on the NP size, shape, surface ligand and charge, as well as the temperature and the surrounding medium, and it is also very sensitive to the proximity of other NPs. The surface plasmon band is very characteristic for gold, silver and copper NPs. However, it is absent in both ultrasmall NPs ($d < 2$ nm) and bulk material.

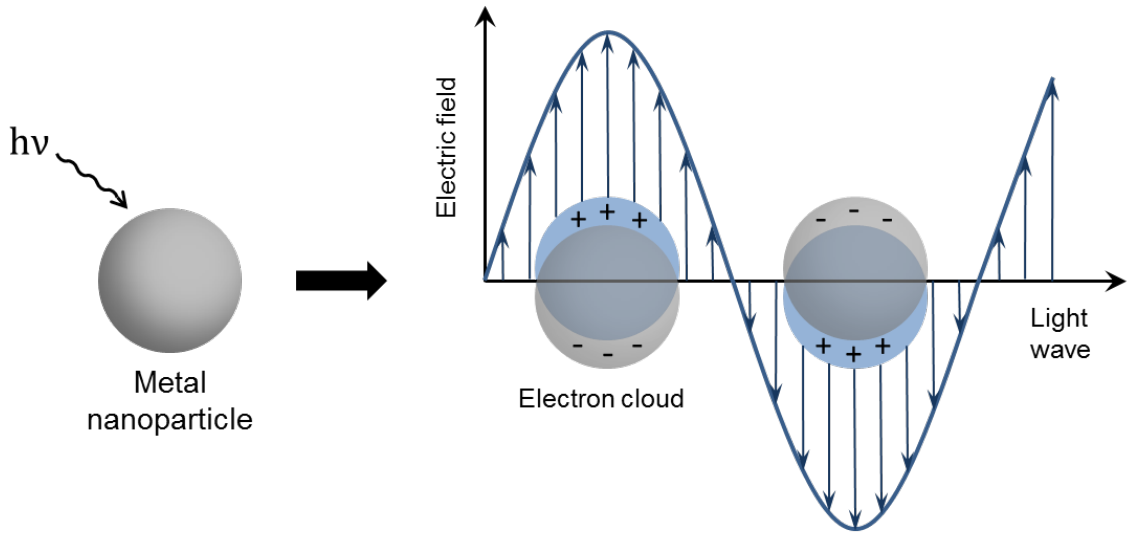


**Figure 1.3.** Schematic representation of the interaction of an electromagnetic field with a metal nanoparticle that produces the oscillation of conduction electrons inducing a dipole within the nanoparticle.

Gold nanoparticles (AuNPs) have been widely used for biomedical applications due to their size and shape, optoelectronic properties, biocompatibility, low cytotoxicity as well as easy functionalization.[21] As the surface plasmon resonance depends on the proximity among the NPs, particle aggregation results in a broadening and a shift to red frequencies of the plasmon band that can be visible through a change in color (from red to blue). This property has been exploited for biosensing applications, monitoring the interaction of a ligand present on the AuNP surface with a specific receptor that produces AuNPs aggregation (Figure 1.4).[22] This aggregation can be monitored with a UV/Vis spectroscopy or even by the naked eye, allowing NPs to be used in biodiagnostic assays. Such biosensors have already been used in pregnancy tests, (First Response®) in the 1990s.[23] The use of AuNPs allows for a better understanding of the binding specificities between different biomolecules using a rapid and high-throughput method based on the measurement of surface plasmon resonances.[24]

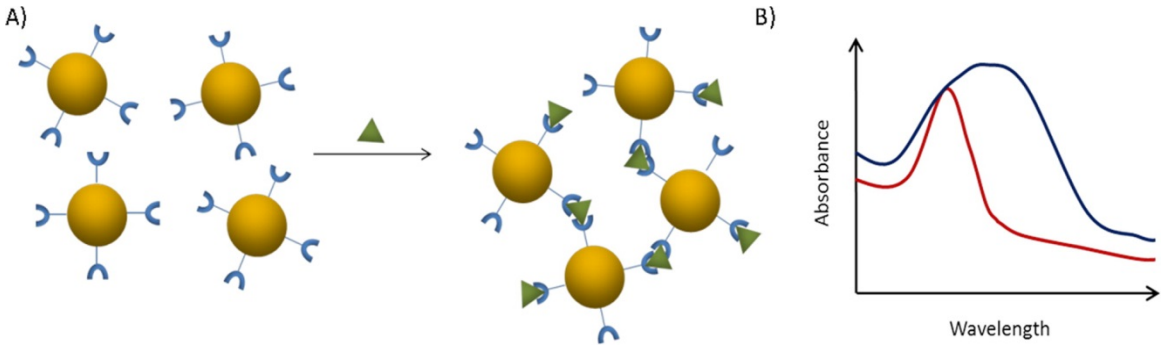


**Figure 1.4.** a) Schematic representation of the aggregation of gold nanoparticles upon biomolecular addition. b) UV/Vis absorbance spectrum of well-dispersed gold (red) and aggregated (blue) nanoparticles. Reprinted with permission from Delbianco *et al.*[22]

Many methods have been established to control the size,[25-27] shape[28] and surface functionalization[19] of AuNPs. A perfect control on both size and shape is highly important in biomedical applications as it determines the wavelength where the plasmon band has its maximum. An emerging application of AuNPs in nanomedicine is photothermal therapy as it enables to selectively perform hyperthermia in tumors and avoid damaging healthy tissue.[29] This process takes place when plasmonic NPs accumulate in tumors and are further irradiated with a laser source that has a wavelength in the maximum of the NP surface plasmon resonance. The absorbed light is converted into heat that produces irreversible damage to the tumor tissue. Since the size and shape of AuNPs is controllable, the surface plasmon resonance is usually tuned to the near-infrared (NIR) window to ensure that minimum light is absorbed by hemoglobin and water allowing for a deeper tissue penetration.[30] The typical AuNPs used for hyperthermia applications are nanoshells,[31] nanorods,[32] nanocages[33] and nanostars,[34] as the geometry allows for obtaining small AuNPs with a plasmon resonance band in the NIR window.

The functionalization of AuNPs with biomolecules can be complicated due to the complexity of these structures. Surface functionalization of AuNPs usually occurs through ligand exchange reactions where thiol functionalized moieties are used to displace adsorbed ligands. In this way, the loading efficiency can be controlled by the amount of thiols added, and the introduction of two or more thiol ligands allows for multiple conjugation.[35] Functionalization can be done through covalent or non-covalent conjugations.[21] Covalent conjugations can be achieved through a direct thiol displacement on the gold surface if the selected biomolecule has an available thiol moiety.[36] If the thiol group is not present, covalent bond formation can be performed on AuNPs through coupling reactions[37] or click

reactions.[38] The covalent bond provides a stable structure permitting the use of NPs for applications such as imaging. After a first covalent conjugation, a non-covalent conjugation can be further exploited for biofunctionalization through weak interactions such as hydrogen bonding,[39] electrostatic interactions[40] and hydrophobic interactions.[41] These conjugations are mostly used in drug delivery to facilitate the release of cargo.

### 1.1.1.2. Silica and silicon nanoparticles

Silica NPs, made of silicon dioxide, are a powerful tool for biological applications due to their easy synthesis and functionalization, biocompatibility and low cytotoxicity.[42-43] Many methods have been used to control the size, shape and pore size of silica NPs. In 1968, Stöber reported a pioneering method to prepare monodisperse silica nanoparticles of controlled size.[44] This synthesis uses silicates in a mixture of water, alcohol and ammonia to produce different sized NPs, depending on the precursor concentrations. This method was further modified to synthesize mesoporous silica nanoparticles (MSNs), silica NPs that contain pores with diameters between 2 and 50 nm, by introducing polymer templates (often surfactants) that interfere in silica precursor growth. The variation of this polymer template as well as the concentration used, allows for control over pore size, structure and particle cristalinity.[42] Hollow silica nanoparticles have been produced by utilizing a polymer template (such as polystyrene particles) coated with polyelectrolytes, through the layer by layer assembly technique, to facilitate silica adsorption. The removal of the polystyrene template through calcination permits the formation of hollow silica particles.[45]

Surface functionalization of silica NPs can be performed using two strategies: through a co-condensation strategy during the synthesis of the NPs that is preferable for internal functionalization of the mesopores; or through a surface modification after the synthesis. The surface functionalization can be achieved by condensation of the available hydroxyl groups with halosilanes to incorporate functional groups such as amines or thiols that can be further reacted with the desired compounds.[42, 46]

Silica NPs have been widely used for drug delivery and imaging. In particular, MSNs have been used as nanocarriers because of the high drug loading capacities and the controlled drug release through the mesoporous structure. This structure can be modified to host the selected molecules that are further released under physiological conditions. The *in vivo*

phamacokinetics can also be controlled by synthesizing monodisperse samples as well as tuning the size and structure.[47] MSNs have also been widely used for imaging applications as it was shown that they are optically transparent allowing for the use of tracers without interferences.[43, 48] Contrast agents such as metal[49] and magnetic NPs,[50] organic dyes[51] or quantum dots[52] were encapsulated in MSNs.

Silicon NPs have recently attracted attention in biomedical applications as they exhibit size depending optical properties, easy surface conjugation and low toxicity.[53] The optoelectronic properties of silicon NPs arise when the particle size is between 1 and 5 nm, and hence, these NPs are usually used in the ultrasmall range.[54-55] *In vivo* studies revealed that silicon NPs are faster biodegraded when compared to other optically active materials.[11]

### 1.1.1.3. Carbon-based nanomaterials

Graphite consists of stacked layers of hexagonal $sp^2$-carbon and is the starting material for the synthesis of carbon-based nanomaterials. These nanomaterials have unique physical properties such as high electrical and thermal conductivity as well as mechanical strength.[56] The most common carbon based materials are carbon nanotubes, fullerenes and graphene (Figure 1.5).

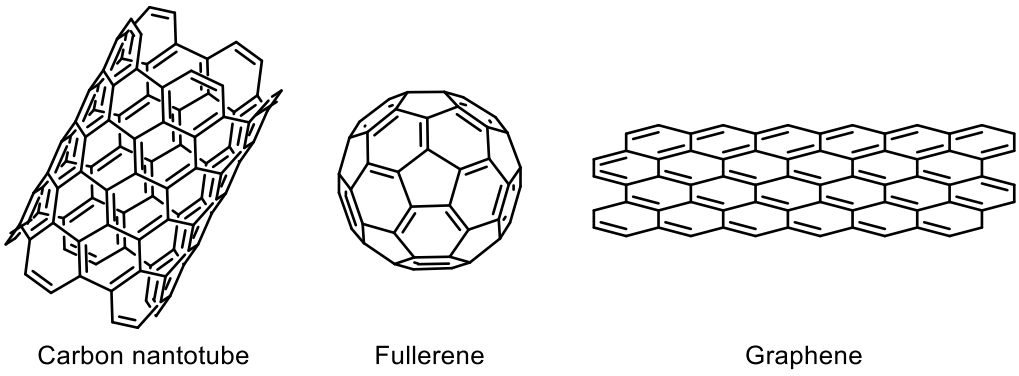


**Figure 1.5.** Structure of different carbon based nanomaterials.

Carbon nanotubes are composed of a rolled up graphene sheet that forms a seamless cylinder. They can be single-walled if they have only one layer or multi-walled if they are formed by multiple concentric layers of graphite.[57] Carbon nanotubes have metallic, semiconducting and superconducting electron transport properties. They have been therefore used in many biomedical studies such as diagnostic tools, biosensors and even as

drug delivery devices and for tissue engineering.[58] Nevertheless, carbon nanotubes are not soluble in most solvents and therefore need to be functionalized to be used in biological media.[12] Carbon nanotubes can be conjugated to drugs, carbohydrates, peptides or nucleic acids for intracellular delivery.[59]

Fullerenes are carbon cage molecules in the shape of a soccer ball composed of 60 carbon atoms distributed in twelve pentagons and 20 hexagons. Both inner and outer surfaces are covered with a sea of electrons.[60] The poor solubility in aqueous solutions can be overcome by chemical and supramolecular functionalization to increase the solubility in polar solvents.[61] Similarly to carbon nanotubes, drugs, carbohydrates, peptides and nucleic acids can be conjugated to fullerenes for delivery purposes.[62]

Graphene is a honeycomb-like monolayer of carbon atoms and is the basic building block for other carbon based materials such as carbon nanotubes. Since its discovery in 2004, graphene has raised interest in the biomedical field due to its physical, chemical and mechanical properties.[14, 63] Its flat morphology and excellent mechanical properties render graphene not only highly useful for delivery applications and photothermal therapy,[64] but also for tissue engineering.[65]

### 1.1.1.4. Polymers and dendrimers

Polymeric NPs are used for biomedical applications due to the versatility of the structures used to build the scaffolds that can host and deliver a cargo to a targeting point in response to external stimuli or under certain physiological conditions.[15] The responsiveness of polymeric NPs can be controlled by introducing different functionalities in the scaffold that react under change of pH, reducing or oxidizing conditions or upon enzymes.[15, 66]

Dendrimers are highly branched three-dimensional polymeric molecules composed by identical fragments, dendrons, that originate from a core.[67] The stepwise synthetic growth allows for obtaining extremely monodisperse samples in contrast to conventional polymers where a mixture of particles is obtained. Completely control on the structure and composition can be achieved, permitting to exactly modify the physical and chemical properties of dendrimers.[16] Dendrimers can be conjugated with different functionalities depending on the biomedical application, using many different strategies.

### 1.1.1.5. Magnetic nanoparticles

The most commonly used magnetic NPs for biomedical applications are the biocompatible and biodegradable ferrite colloids magnetite ($Fe_3O_4$) and maghemite ($\gamma$-$Fe_2O_3$).[17, 68] When these NPs are small enough (typically 3-50 nm), each NP is composed of a single magnetic domain and behaves like a giant paramagnetic atom with a very fast response to applied magnetic fields.[69] These superparamagnetic NPs can be used for MRI contrast enhancement, tissue engineering, drug delivery, hyperthermia and cell separation, and are specially interesting since they do not retain magnetism even after removal of the magnetic field.[70]

There are several strategies to synthesize iron oxide NPs: physical methods that include gas-phase deposition and electron beam lithography; microbial methods and wet chemical methods such as sol-gel and oxidation syntheses, co-precipitation, hydrothermal reactions, etc.[17] After the synthesis, the magnetic NPs need to be functionalized to prevent aggregation, as in magnetic suspensions also the magnetic dipolar forces between particles may lead to particle aggregation. The stabilization can be achieved by introducing functionalities that give electrostatic and steric repulsions between NPs.[68]

Covalent bioconjugation of NPs can be done with amines, carboxyls, aldehydes and thiols exposed on the nanoparticle surface.[68] Magnetic NPs for drug delivery can be designed by loading the drug on the NP surface or by introducing a shell that increases the loading capabilities.[17] Magnetic NPs can also be used in hyperthermia applications by injection into a tissue and applying an alternating magnetic field that generates heat due to the magnetic hysteresis loss. Similarly to photothermal therapy using plasmonic NPs, magnetic NPs can destroy tumors without damaging healthy tissue.[17]

### 1.1.1.6. Quantum dots

Quantum dots are luminescent semiconductor nanoparticles made of binary compounds such as selenides or sulfides of metals such as cadmium or zinc.[22] The optical properties depend on the quantum dot size and can be tuned.[18] Moreover, quantum dots have a broader excitation band and sharp emission bands, allowing for multicomponent analysis using a single excitation wavelength (Figure 1.6).[22, 71] Quantum dots are usually synthesized at high temperature in the presence of thiol derivatives such as ZnS or CdS to improve the

fluorescent quantum yield, as well as to protect them from photo-oxidation and to minimize cytotoxicity.[72]

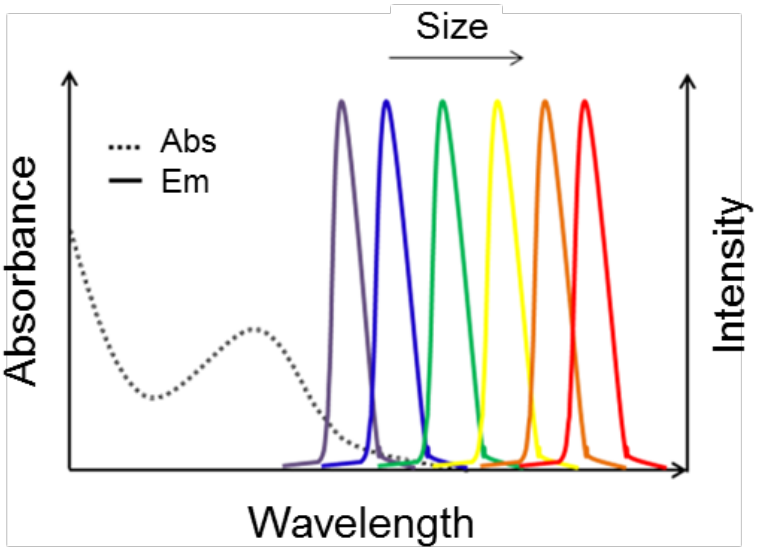


**Figure 1.6.** Absorbance and emission profiles of quantum dots with different sizes. Reprinted with permission from Delbianco *et al.*[22]

Before their use in biological systems, quantum dots need to be coated to improve the stability, make them water soluble and maintain the fluorescence. So far, quantum dots have been used for imaging applications, such as in contrast agents, due to their promising optical properties that can be tuned to the NIR window. Nevertheless, some limitations such as high toxicity, make them a good complement to existing organic fluorophores rather than a replacement.[18]

## 1.1.2. Nanoparticle characterization

### 1.1.2.1. Nanoparticle size, shape and surface charge

The size of nanoparticles is extremely important as it determines the biodistribution and retention of the NPs in tissues.[73] Dynamic light scattering (DLS) measures the Brownian motion of NPs in suspension, which is the random motion of particles in a fluid due to their collision with fluid molecules. The Brownian motion can be related to the hydrodynamic radius (*d (H)*) through the Stokes-Einstein equation (1), where the velocity of the Brownian

motion is defined by the translational diffusion coefficient ($D$), $k$ is the Boltzmann's constant, $T$ is the absolute temperature and $\eta$ is the viscosity.

$$d(H) = \frac{kT}{3\pi\eta D} \qquad (1)$$

DLS measures the mean particle size and homogeneity of size distribution, expressed with the polydisperse index (PDI). The main limitation of DLS is the measurement of samples containing several size distributions, as the signal of smaller particles is lost because the signal intensity of a particle with radius $r$ is proportional to $r^6$, and therefore will be masked by larger particles (Figure 1.7).[73]

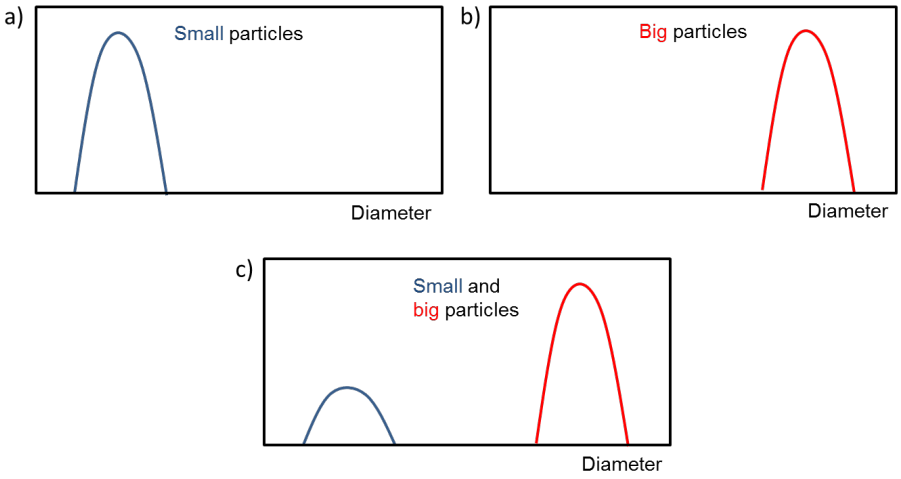


**Figure 1.7.** Dynamic light scattering measurements when the sample contains a) small particles, b) big particles, and c) small and big particles.

Small-angle X-ray scattering (SAXS) measures the variation of the electron density in a sample. SAXS can give information about the NP size distribution, shape and surface structure such as pore size.[74] The interaction of the X-ray radiation with a material causes a small deviation of the incident direction, known as small-angle scattering.[75] Depending on these angular ranges, SAXS can give size information between 1 and 100 nm. Nevertheless, this technique, as well as DLS, should be combined with supporting techniques such as electron microscopy to get information of both size and shape of NPs.

Electron microscopy (EM) uses a beam of accelerated electrons and electromagnetic lenses to generate images. These images have higher resolution than those obtained with optical microscopy due to the shorter wavelength of electrons compared to photons.[76]

Scanning electron microscopy (SEM) uses incident electrons that interact with the sample to gain information about the surface topography and composition. Due to the interaction of these electrons with the sample, several electrons are emitted, such as secondary electrons that are inelastic scattering electrons. The detection of these secondary electrons, emitted from the sample surface, is the most common mode in SEM and allows for surface imaging with a resolution smaller than 1 nm.[76] A limitation of SEM and all EM techniques is the destructive sample preparation that also needs to be stable in high vacuum. Moreover, to detect the surface electrons, the surface of the sample needs to be electrically conductive and therefore might need to be coated with an ultrathin layer of a conducting material, usually gold, through low vacuum sputter or high vacuum evaporation. A method to overcome the problems of high vacuum during sample preparation and measurements is the use of environmental SEM (ESEM) that allows for imaging of wet, uncoated samples. This technique permits to image in their natural state without further modifications.[77]

In transmission electron microscopy (TEM), the incident electrons are transmitted through the sample. As the incident electrons interact with the ultrathin specimen, they are transformed into unscattered electrons, elastically scattered electrons or inelastically scattered electrons. The scattered and unscattered electrons are focused by electromagnetic lenses and projected on a screen to generate an electron diffraction, an amplitude-contrast image, a phase-contrast image or a shadow image of varying darkness depending on the density of unscattered electrons.[78] TEM provides better spatial resolution compared to SEM and has the possibility to couple analytical techniques to obtain a better analysis.[79] Scanning TEM (STEM) allows for imaging of samples completely submerged in a liquid permitting observation with high contrast without the addition of contrast agents.[80] Another method to study biological samples without destroying the native environment is using cryo-electron microscopy (cryo-EM), which uses cryogenic temperatures. Cryo-EM allows for imaging of biological samples without dehydration or fixation.[81] Moreover, the collection of multiple images in cryo-EM at different angles permits the formation of 3D images.

The surface charge of a NP can be measured using the zeta (ζ) potential which determines the stability of the NP suspension. Strongly charged NPs (above 30 mV or below -30 mV) are more stable thanks to electrostatic repulsions. ζ potential is the electric potential at the slipping plane between the dispersed medium and the layer attached to the NP and can be determined by measuring the electrophoretic mobility.[73] The ζ potential of a sample

depends on many parameters such as ionic strength, pH and composition of the dispersed medium. Similar to DLS, the main limitation of ζ potential measurements is that the results of larger NPs will mask the value of smaller particles.[73]

### 1.1.2.2. Nanoparticle surface chemistry

Surface modification of NPs influences their biological roles and is able to lower cytotoxicity.[82] The stabilizers on the NP surface are usually small molecules present in very small amounts making the identification and quantification very challenging.[83]

NMR spectroscopy for surface characterization is often limited by the low solubility of the stabilizers that difficult the small molecules to tumble rapidly to provide a sharp signal.[84-85] Conjugating long and flexible linkers to the NPs increases the solubility which provides better NMR spectra.[83] Therefore, NMR is a suitable technique to monitor reactions and product formation but has limitations for structure elucidation of NP stabilizers.[86]

Fourier transform infrared (FTIR) spectroscopy has been widely used to identify functional groups present on the surface of NPs. This technique permits to identify specific functional groups, such as esters, carbamates, amides or azides.[83]

X-ray photoelectron spectroscopy (XPS) is a surface spectroscopic technique that gives information about the elemental composition, empirical formula, chemical and electronic state of the elements existing within the surface of a material.[83] The samples are irradiated with an X-ray beam allowing for the escape of surface electrons with a certain kinetic energy. This kinetic energy can be related to the binding energy of the emitted electrons that depends on the element, the orbital and chemical environment of the atom from which the electron is ejected.[87]

### 1.1.2.3. Nanoparticle activity assessment in cells

To assess the biological behavior of NPs in cells, confocal laser scanning microscopy (CLSM) and fluorescence-activated cell sorting (FACS) are powerful tools when the NPs are tagged with a fluorescent marker.[73]

FACS allows for rapid analysis of multiple characteristics of cells, such as cellular size and internal complexity, as well as uptake studies of fluorescent tagged biomolecules or

nanoparticles.[88] The cells are individually scanned by a laser and the scattered light at different angles gives information about the cellular physical properties, whereas the emitted light is used to identify fluorescent labelled antibodies and NPs.[88] Quantitative information is obtained by the determination of the cell population (that permits to distinguish between alive and dead cells) and the amount of fluorescent labelled NPs or drug internalized by the cells.[73]

CLSM is used for imaging of fluorescent tagged biological systems. In combination with FACS, confocal microscopy is able to pinpoint the location of the tagged nanomaterial within the cells, by using fluorescent tagged antibodies that stain the different organelles. With co-localization calculations, the quantification of internalized NPs is possible.

## 1.2. Multivalency

Multivalency involves multiple simultaneous binding between two units, such as a ligand and a receptor, and plays a key role in biological processes to establish strong or reversible chemical interactions.[89] These additive interactions take place between cells or other organisms, such as viruses and bacteria and are important in biomedicine.[90]

Carbohydrates, together with nucleic acids and proteins, are the most abundant class of biopolymers and are mainly used for energy production and as structural materials. Glycans are found on the surface of living cells forming a thick layer called glycocalyx (Figure 1.8), and are involved in important biological processes such as cell-cell interactions, and they regulate important biological functions such as inflammation, cell growth, differentiation and adhesion.[91] The structural complexity of the glycocalyx makes glycobiology highly challenging.[92]

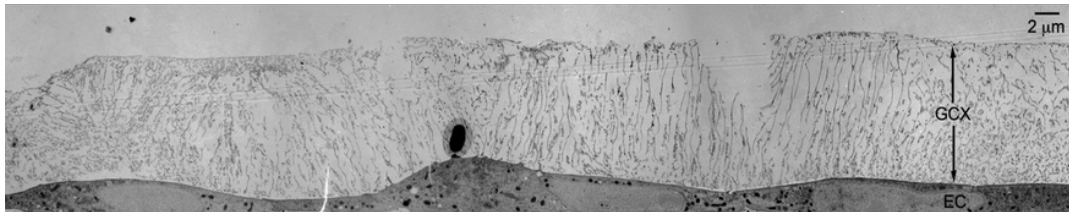


**Figure 1.8.** Transmission electron micrographs of the glycocalyx (GCX) on cultured bovine aortic endothelial cells (EC). Scale bar = 2 µm. Adapted from Ebong *et al.*[93] Copyright (2011), with permission from Wolters Kluwer Health.

Carbohydrates can form hydrogen bonds with other carbohydrates (carbohydrate-carbohydrate interactions, CCIs) or with proteins (carbohydrate-protein interactions, CPIs).[91] These interactions are typically very weak (in the mM range), but multivalency compensates the low affinity of one binding event. Systems that display multiple identical carbohydrates exhibit generally stronger binding affinities than the sum of each single contribution.[94]

There are different possibilities to construct multivalent networks, such as chelating, statistical multivalency, adhesion or sub-site binding (Figure 1.9).[95] The binding affinity of CPIs is known to depend on size, spatial assembly and valency.[94]

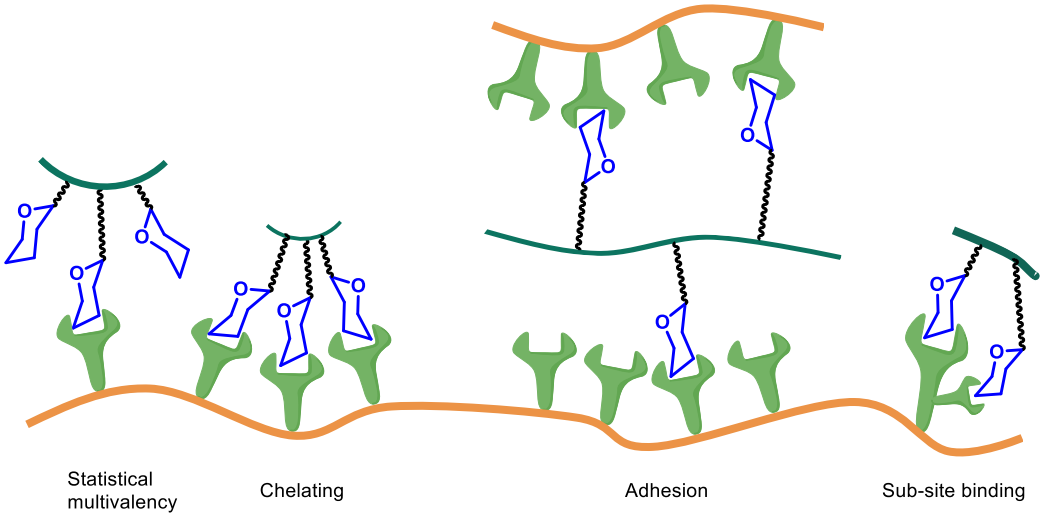


**Figure 1.9.** Different possibilities of multivalent binding modes between carbohydrates and carbohydrate receptors.

## 1.2.1. Multivalent carbohydrate based nanomaterials

This section has been modified in part from the following article:

Carbohydrates in supramolecular chemistry. M. Delbianco, P. Bharate, S. Varela-Aramburu, P. H. Seeberger, *Chem. Rev.* 2016, 116, 1693–1752.[22] doi:10.1021/acs.chemrev.5b00516. Copyright 2016 American Chemical Society

In order to mimic the biological processes that occur in nature, synthetic chemists have tried to construct multivalent carbohydrate based scaffolds.[96-97] Multivalency has been exploited for the design of high affinity ligands that can be used as drugs and probes.

Intense efforts have been devoted to better understand this phenomenon as a first step toward predicting the optimal density of ligand display.[98]

The scaffold at the center of the glycoconjugate serves to classify the systems. Organic macrocycles,[96, 99-100] dendrimers,[101] nanoparticles,[102] and polymeric backbones[103] are used to delineate the classes of carbohydrate-based supramolecular assemblies (Figure 1.10). Carbohydrates are used as building blocks for the synthesis and stabilization of supramolecular systems based on multiple weak interactions.

Many supramolecular systems based on nanomaterials have been described.[22] Glyconanomaterials are a suitable platform to detect lectins or study CCIs and CPIs, and are usually applied as biosensors and as biomedical nanocarriers.

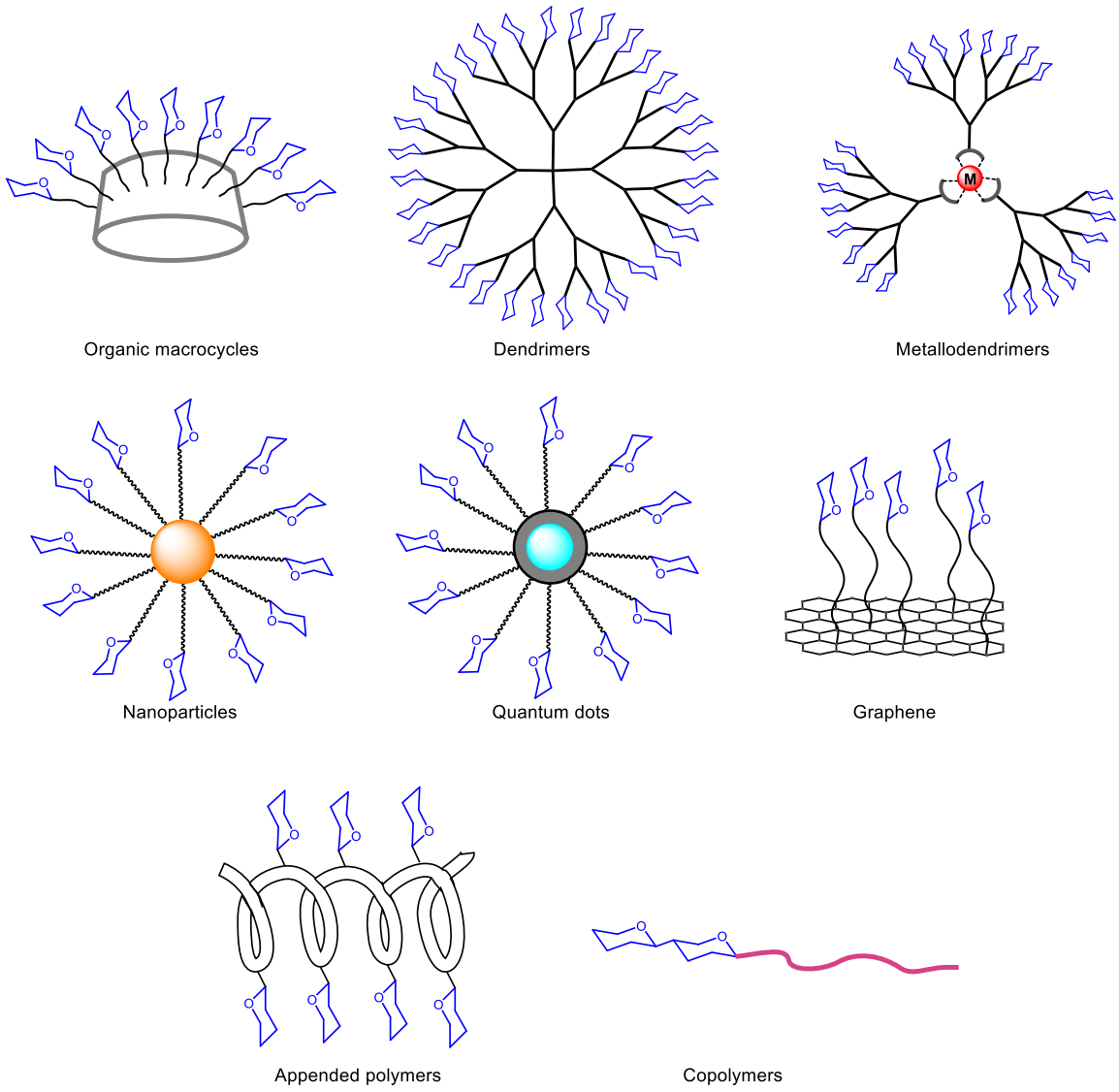


**Figure 1.10.** Overview of different glycosylated scaffolds used for supramolecular assemblies. Adapted from Delbianco *et al.*[22]

# 1.3. Nanomedicine

The use of NPs for biomedical applications such as imaging and therapy of diseases has increased in the past decade.[104] Scientists have tried to develop multimodal NPs that are able to simultaneously accomplish multiple tasks such as imaging and drug delivery, or even perform complex functions that require more than one functional unit (Figure 1.11). The perfect control of all the important parameters such as surface chemistry, cargo, size, shape and matrix is still very challenging.[105] Nevertheless, the need of personalized disease treatments is pushing the field of nanomedicine forward, with the development of

theranostic NPs that can perform diagnosis, imaging, targeted delivery and controlled drug release.[104]

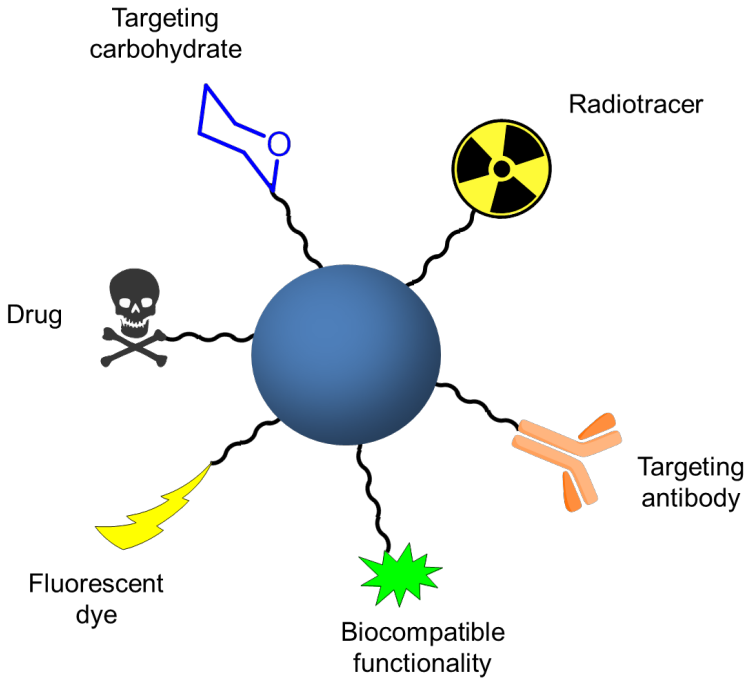


**Figure 1.11.** Example of an engineered nanoparticle for multimodal drug delivery.

It is known that NPs without targeting moieties accumulate in tumors more than in normal tissues due to the enhanced permeability and retention (EPR) effect of the tumor vasculature. NP accumulation in tumors can be explained by the permeability of tumor blood vessels together with the ineffective drainage of the lymphatic system.[106] Therefore, the use of NPs conjugated with cellular targeting carbohydrates increases the chemotherapeutic effect for different types of cancers.[107]

## 1.3.1. Imaging

Fluorescence techniques have been widely used for imaging to identify and track molecular recognition events. The most common fluorescent dyes are organic dyes, comprising a wide range of structures with different functionalities, solubility and spectral properties.[108] The main limitation of organic dyes is photobleaching (decrease in fluorescence intensity).[109] This can be prevent encapsulating the organic dyes to protect them from environmental oxygen that affects the photostability.[110] Silica NPs are very often used for imaging since the synthesis and chemical functionalization is simple and well-stablished.

Similar to organic dyes, quantum dots exhibit tunable optical properties for imaging applications. The high toxicity of quantum dots is their disadvantage.[108]

Magnetic resonance imaging (MRI) is an imaging technique that requires the use of a contrast agent such as magnetic nanoparticles and allows for the visualization of the internal structure of living organisms. MRI has been used for both *in vitro* and *in vivo* imaging and is a safer technique than X-ray computed tomography (CT) and positron emission tomography (PET).[108] PET is a nuclear medicine technique that provides 3D images by detecting positron-emitting radionuclides.

The use of glycosylated NPs in imaging studies gives a better understanding of the role of carbohydrates in nature through CCIs and CPIs. Using different nanomaterials, the interaction between mannose functionalized fluorescent NPs and the lectin FimH that is present on the pili of *E. coli* was elucidated.[111-112] Other studies give an insight of the interactions with more complex carbohydrates, such as between the cancer-associated glycosphingolipids sialosyllactosylceramide (GM3) present on melanoma cells and gangliotriaosylceramide (Gg3), present on lymphoma cells, that play an important role during the adhesion of melanoma cells to the endothelium in tumor metastasis.[55] Sialyl Lewis$^X$ functionalized NPs also served to image the endothelial inflammation during stroke as they interact with selectin proteins.[113]

## 1.3.2. Drug delivery

NPs have been widely used in drug delivery applications. Their high surface area permits drug loading enhancing the solubility and stability of the drugs. The conjugation of targeting moieties to NPs increases the therapeutic efficiency and lowers side effects. Moreover, the possibility to create multivalent interactions with the cell surface mimics the biological events occurring in nature. Drug conjugated nanoparticles show enhanced pharmacokinetics and tumor tissue accumulation due to the EPR effect.[23]

A perfect nanocarrier should be biocompatible, have high drug loading capacities, have no premature drug release, be able to target the specific cells or tissues and display controlled drug release with an optimal effective local concentration.[114]

Targeted drug delivery allows for drug accumulation at a specific place independently of the drug administration method and route.[115] Effective *in vivo* targeted drug delivery needs drug loading efficiency into the nanocarrier, but also an optimum blood half-life to ensure that the nanocarrier reaches the targeted place, and drug release within a timeframe where the drug is effective.[116] Targeted drug delivery can be only achieved when there is overexpression of a specific marker on the targeted cell surface.[116]

Carbohydrates can be used as targeting moieties that direct the drug loaded NPs to the place where they will carry out the therapeutic effect. Some cells overexpress lectins or carbohydrates that specifically interact with the carbohydrates conjugated to the NPs through CPIs and CCIs, respectively. Mannose receptors are overexpressed in cells of the immune system such as macrophages or dendritic cells.[117] Galactose conjugated NPs can be used to target lectins such as asialoglycoprotein, which is overexpressed in liver cancer cells.[118] Glucose is also known to be a transporter to the brain, and therefore shows potential for brain related diseases.[119-120]

More complex carbohydrates such as Sialyl Lewis$^X$ can be used to target the selectin family that are type I transmembrane glycoproteins containing an extracellular lectin domain.[121] These glycoproteins have a role in the adhesion process between platelets and leukocytes during tissue damage or inflammation.[122]

## 1.4. Aim of this thesis

The objective of this dissertation is to contribute to the field of nanoparticle based imaging and drug delivery technologies for the treatment of different diseases. To achieve this goal, nanoparticle based carriers were designed and developed. The second step was the biological evaluation of the nanocarriers *in vitro* and *in vivo*, with a special focus on the imaging and drug delivery study of the targeted diseases. The protozoan parasites *Plasmodium falciparum* and *Toxoplasma gondii* were chosen in order to explore the use of nanotechnology for theranostics of these protozoan parasites. To further contribute to the improvement of cancer chemotherapy, tumor cells were targeted for both imaging and controlled drug delivery.

The synthesis of ultrasmall gold nanoparticles using a thio-glycoside was explored to obtain biocompatible nanocarriers (Chapter 2). These ultrasmall nanoparticles show high potential in multimodal drug delivery due to the high surface area that can be exploited for multiple conjugations. Due to the presence of high cysteine domains on the surface of apicomplexan parasites, the developed nanoparticles can be used to study binding efficiency to these cysteine domains that could be further exploited for imaging and drug delivery applications of malaria and toxoplasmosis (Chapter 3).

Mesoporous silica was used as drug delivery nanocarriers to investigate the synthesis of a different morphology that increases the cellular uptake (Chapter 4). Nanoparticle doping with disulfide moieties can lead to responsive breakable nanocarriers for controlled drug delivery with a special interest in cancer treatment.

Finally, different glycosylated nanomaterials were synthesized to explore the biological activity of multivalent glycosylated scaffolds (Chapter 5). A better insight in brain targeting can be obtained that could be further utilized for imaging and drug delivery of brain related diseases. Also, more information about carbohydrate-protein interactions between microalgae and cyanobacteria can be acquired.

# 2. Synthesis and characterization of glycosylated gold nanoclusters for biomedical applications

This chapter has been modified in part from the following article:

Straightforward and robust synthesis of monodisperse surface-functionalized gold nanoclusters. S. Varela-Aramburu, R. Wirth, C.-H. Lai, G. Orts-Gil, P. H. Seeberger, *Beilstein J. Nanotechnol.* 2016, 7, 1278–1283.[36] doi:10.3762/bjnano.7.118

## 2.1. Introduction

Nanoparticles, materials which range from 1 to 100 nm, are ideal tools to study biological processes.[2,72] Many different materials have been used to create nanoparticles as discussed in Chapter 1.[21,123-125] In particular, gold nanoparticles (AuNPs) are an attractive platform due to their biocompatibility, low toxicity, low immunogenicity,[126] inherent optoelectronic properties,[20] and high contrast in transmission electron microscopy (TEM). AuNPs are relatively easy to synthesize, functionalize and have tunable optical properties.[8, 19, 21, 127-128] Therefore, gold nanoparticles functionalized with carbohydrates,[102] proteins,[129] antibodies[130] and DNA,[131] are commonly used as multivalent materials for biological studies. Some applications include the use of AuNPs *in vivo* when tagged with radiotracers,[130,132] for targeted delivery[133] and, upon functionalization with carboxylic acids, to inhibit β-amyloid fibril growth during Alzheimer's disease.[134]

Several methods to synthesize gold nanoparticles have been reported. The most common method for producing spherical AuNPs is the reduction of chloroauric acid ($HAuCl_4$) with sodium citrate under refluxing conditions.[135] The appearance of a deep red color is indicative

of the formation of AuNPs. The size of the AuNPs is tunable from 10 to 100 nm by changing the concentration ratio of $HAuCl_4$ to sodium citrate.

Brust *et al*. described the synthesis of AuNPs based on a biphasic reaction using tetraoctylammonium bromide as a phase-transfer reagent that transports the gold ions from water to toluene.[136-137] The gold ions are then reduced by $NaBH_4$ in the presence of dodecanethiol. The group of Penadés improved this method by adding a thiol-terminated glycoconjugate to an aqueous solution of gold ions.[138] Under these conditions, the reduction is performed in a single phase following the addition of $NaBH_4$.

Another promising method to synthesize AuNPs under reflux using 1-thioglucose as reducing and stabilizing agent,[139] but the resulting 30 nm gold nanoparticles are too unstable to be used as biosensors.[140]

Gold nanoclusters (NCs) are ultrasmall nanoparticles ranging between 1-3 nm. Their high surface area makes NCs ideal substrates for drug delivery applications.[141] Several synthetic methods have been reported in the last 15 years focused on the synthesis of stable and monodisperse NCs. Nevertheless, most of these syntheses are tedious, time consuming and sensitive to reaction conditions such as temperature or even stirring speed.[142-144]

The use of tetrakis(hydroxymethyl)phosphonium chloride (THPC) to reduce $HAuCl_4$ under basic conditions[145] or the use of $NaBH_4$ in combination with cetyltrimethylammonium bromide (CTAB) as stabilizing agent are commonly used conditions for the preparation of NCs.[146]

In an effort to create monodisperse, stable and surface-functionalized gold nanoclusters, 1-thioglucose was explored as a reducing and stabilizing agent. A novel one-pot method to prepare gold nanoclusters using 1-thioglucose at room temperature was developed. This simple and robust method produces stable, and monodisperse nanoclusters. Oxidation of the carbohydrate results in NCs with carboxylic acid on the surface as determined by X-ray photoelectron spectroscopy (XPS). Surface functionalization of NCs can be achieved through coupling to the carboxylic acids or addition of thiols. The resulting NCs are taken up by cells and are less cytotoxic than NCs prepared by other methods.

NCs were further functionalized with a chelator containing a radiotracer for *in vivo* biodistribution studies in mice using positron electron tomography (PET). Results showed the great potential of this new material for biomedical applications as the NCs accumulated in almost all the organs analyzed and were excreted after 24 h.

# 2.2. Results

## 2.2.1. Synthesis of glucose-based gold nanoclusters

The addition at room temperature of 1-thioglucose as reducing agent to gold salts resulted in the formation of monodisperse gold NCs (Figure 2.1 a). Following this interesting observation, the influence of $Au^{3+}$ to 1-thioglucose ratio on the yield and quality of the glucose-stabilized gold nanoclusters (**Glc-NCs**) was investigated (Table 2.1). Stable nanoclusters were synthesized when the ratio of gold to thioglucose was close to 1:1 (0.9:1 – 1:1.4) (Figure 2.1 b). The nanoclusters aggregated within 5 h at very high gold ion to 1-thioglucose ratios (1:0.5). At higher gold ion concentrations NCs were not fully coated with stabilizer and therefore more likely to collapse due to less steric hindrance. On the contrary, at high thioglucose concentrations NCs formation was not observed.

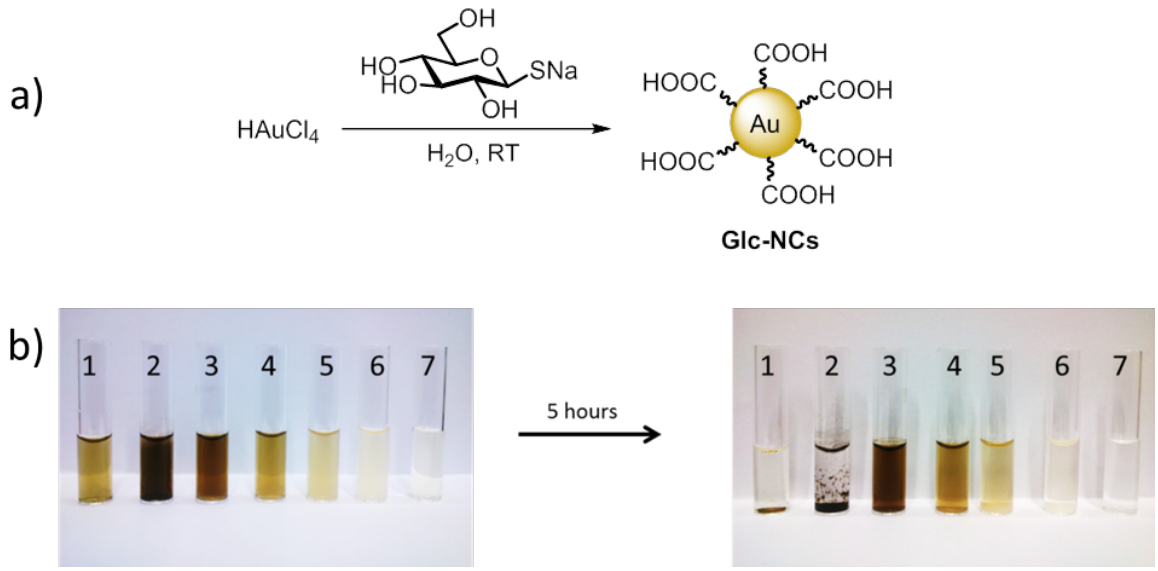


**Figure 2.1**. a) Synthetic scheme of glucose-based gold nanoclusters (**Glc-NCs**); b) **Glc-NCs** using the reaction conditions shown in Table 2.1, freshly synthesized and after 5 h. Numbers correspond to the entries in Table 2.1.

**Table 2.1**. Synthesis optimization of **Glc-NCs**.

| | Ratio Au:1-thioglucose | Observations |
|---|---|---|
| **1** | 1:0.2 | Light brown (unstable) |
| **2** | 1:0.5 | Dark-brown (unstable) |
| **3** | 1:0.9 | Brown (stable) |
| **4** | 1:1.4 | Brown (stable) |
| **5** | 1:1.9 | Light brown (stable) |
| **6** | 1:2.4 | White precipitate |
| **7** | 1:2.8 | No reaction |

The morphology and size of the **Glc-NCs** were analyzed by high resolution TEM bright field imaging. The **Glc-NCs** have a monodisperse spherical shape with an average size of 2.02 ± 0.18 nm, as determined by counting 110 nanoclusters (Figure 2.2). The size of the **Glc-NCs** was corroborated by hydrodynamic diameter measurements with dynamic light scattering (DLS) in aqueous solution (Figure 2.1 c).

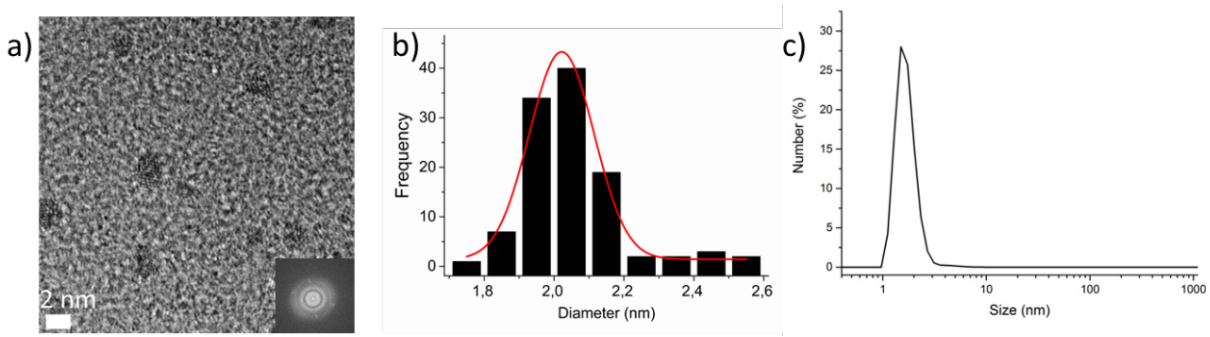


**Figure 2.2**. a) High resolution TEM bright-field image of **Glc-NCs** shows monodisperse nanoclusters, scale bar = 2 nm; b) Size distribution of **Glc-NCs** gives 2.02 ± 0.18 nm in diameter, counting 110 nanoclusters; c) Dynamic light scattering measurement of hydrodynamic diameter of **Glc-NCs** in MilliQ water.

UV measurement of gold nanoparticles allows for the determination of particle size and/or shape.[20, 147] As expected from gold nanoparticles smaller than 5 nm, no plasmon band was observed. The one-pot **Glc-NC** synthesis was temperature independent from 0-90 °C, as proved by the spectroscopic features of the different products (Figure 2.3). The only difference in the use of different temperatures during the synthesis was that at lower temperatures the nanocluster yield was slightly lower, as seen by the lower absorbance in

the UV spectra (absorbance 0.9 vs 1.1). In stark contrast to other known literature procedures[142-144] this procedure is not strongly dependent on the reaction conditions offering a new simple and robust strategy for the production of gold nanoclusters.

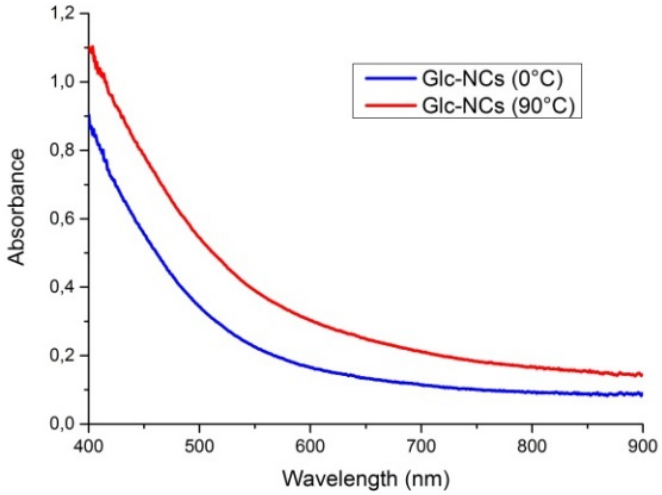


**Figure 2.3.** Ultraviolet spectra of **Glc-NCs** when synthesized at 0 °C and 90 °C. The absence of plasmon resonance in both spectra is indicative of similar shape and morphology.

**Glc-NCs** were more stable than cetyltrimethylammonium bromide (**CTAB-NCs**) and tetrakis(hydroxymethyl)phosphonium chloride stabilized nanoclusters (**THPC-NCs**) as determined by UV absorbance measurements (Figure 2.4). **Glc-NCs** were stable and showed the same absorbance profile after three days of dialysis (Figure 2.4 c), whereas a plasmon band (indication of aggregation) was appearing for **CTAB-NCs** and **THPC-NCs** over a period of time (Figure 2.4 a, b). **THPC-NCs** did not show a plasmon resonance right after the synthesis, since the particle size was below 5 nm as shown by TEM, but after three days of dialysis the appearance of a band at 520 nm revealed nanoparticle aggregation (Figure 2.4 b). **CTAB-NCs** showed a plasmon band directly after synthesis, which is explained by the larger size and polydispersity of these nanoparticles, as shown by TEM imaging (Figure 2.4 c). This plasmon band shifted to longer wavelengths after three days, suggesting an increasing rate of aggregation. Moreover, TEM imaging of freshly synthesized **Glc-NCs** showed monodisperse nanoclusters, which was not the case when the nanoclusters were synthesized by the two other methods. The lack of stability of **THPC-NCs** and **CTAB-NCs** could be due to the surface chemistry of the NCs as the stabilizers are physically adsorbed and could be de-adsorbed by dialysis over time.

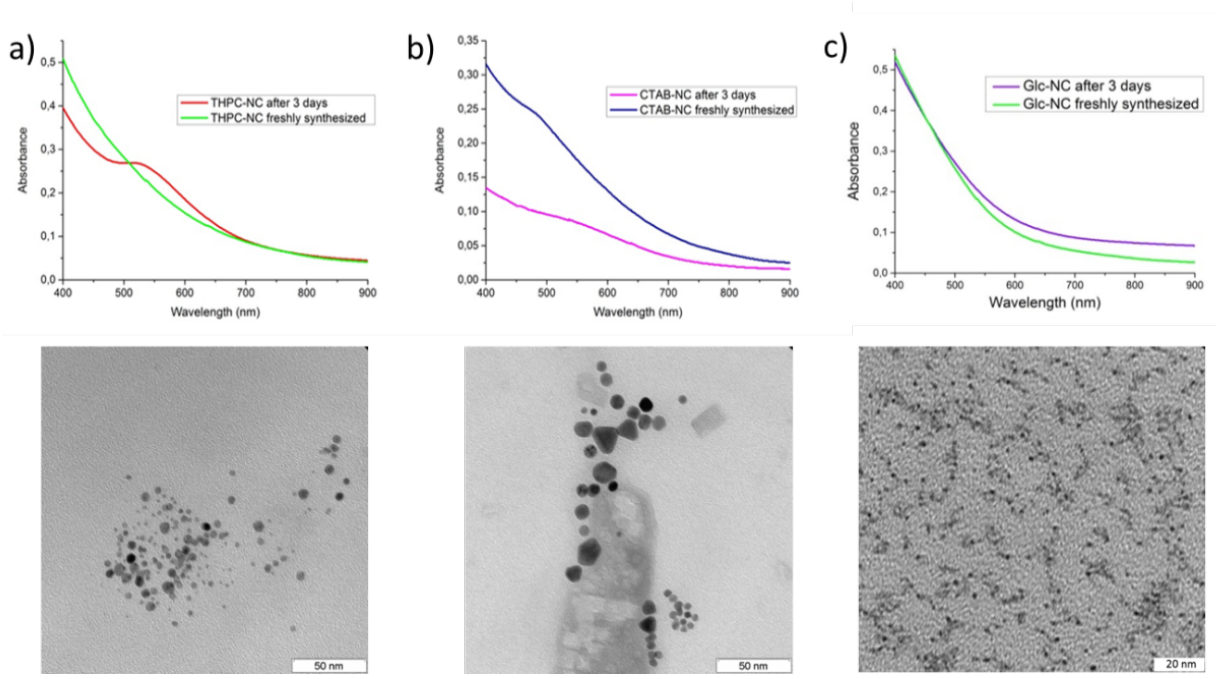


**Figure 2.4**. Ultraviolet spectra comparison of a) **THPC-NCs**, b) **CTAB-NCs**, and c) **Glc-NCs** freshly synthesized and after 3 days. TEM images of freshly synthesized NCs.

The higher stability after dialysis could be explained if we consider that in **Glc-NCs** there is a strong binding between the thiol of the stabilizer and the gold surface, whereas in both **CTAB-NCs** and **THPC-NCs** the stabilizers are only adsorbed to the surface. Zeta (ζ) potential of the nanoclusters over dialysis time was measured to obtain the difference in surface potential between the dispersion medium and the stationary layer of fluid attached to the dispersed nanoclusters. The surface charge did not change upon dialysis for any sample as it stayed positive for **CTAB-NCs** and negative for both **THPC-NCs** and **Glc-NCs**. It can be concluded that the surface chemistry of the nanoclusters does not change and the stabilizers remain attached (Figure 2.5).

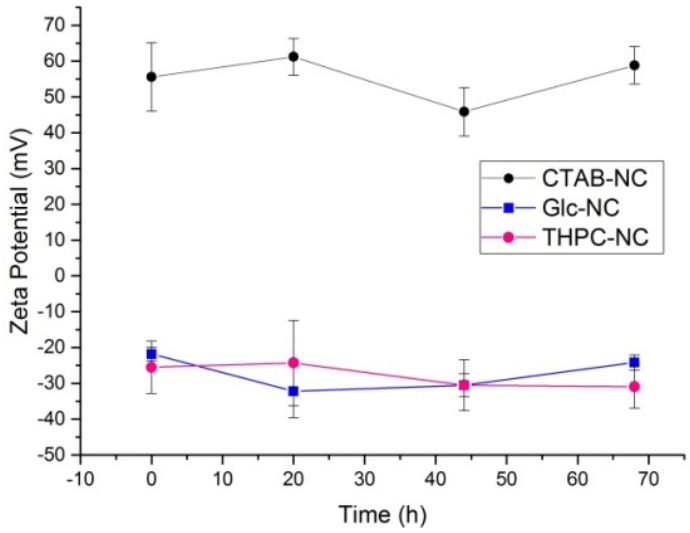


**Figure 2.5.** ζ potential measurement of **Glc-NCs**, **THPC-NCs** and **CTAB-NCs** upon time of dialysis against MilliQ water.

To better understand the structure of the stabilizing agent in **Glc-NCs**, X-ray photoelectron spectroscopy (XPS) (Figure 2.6) was used. XPS allows for the surface chemical characterization of a material as it measures the elemental composition, empirical formula, chemical state as well as the electronic state of the elements located within 1-10 nm of the material. A typical XPS spectrum shows the binding energy that is calculated from the kinetic energy of the emitted electrons, that depends on the element, on the orbital from which the electron was extracted and the chemical environment of the atom.

By analysing the XPS spectra, the gold core of the nanoclusters was confirmed by the Au4f scan (Figure 2.6 b) with a typical binding energy $Au4f_{7/2}$ band at 83.52 eV (

Table 2.2). Moreover, S2p scan (Figure 2.6 e and

Table 2.2) confirmed that the stabilizers were attached through an Au-S bond, as the binding energy $S2p_{3/2}$ of thiol bound to gold gave a signal at 162.5 eV (Table 2.3). The O1s scan (Figure 2.6 c and

Table 2.2) showed C-O (531.5 eV) and carbonyl (533 eV) binding energy bands on the nanocluster surface, as described in Table 2.3.

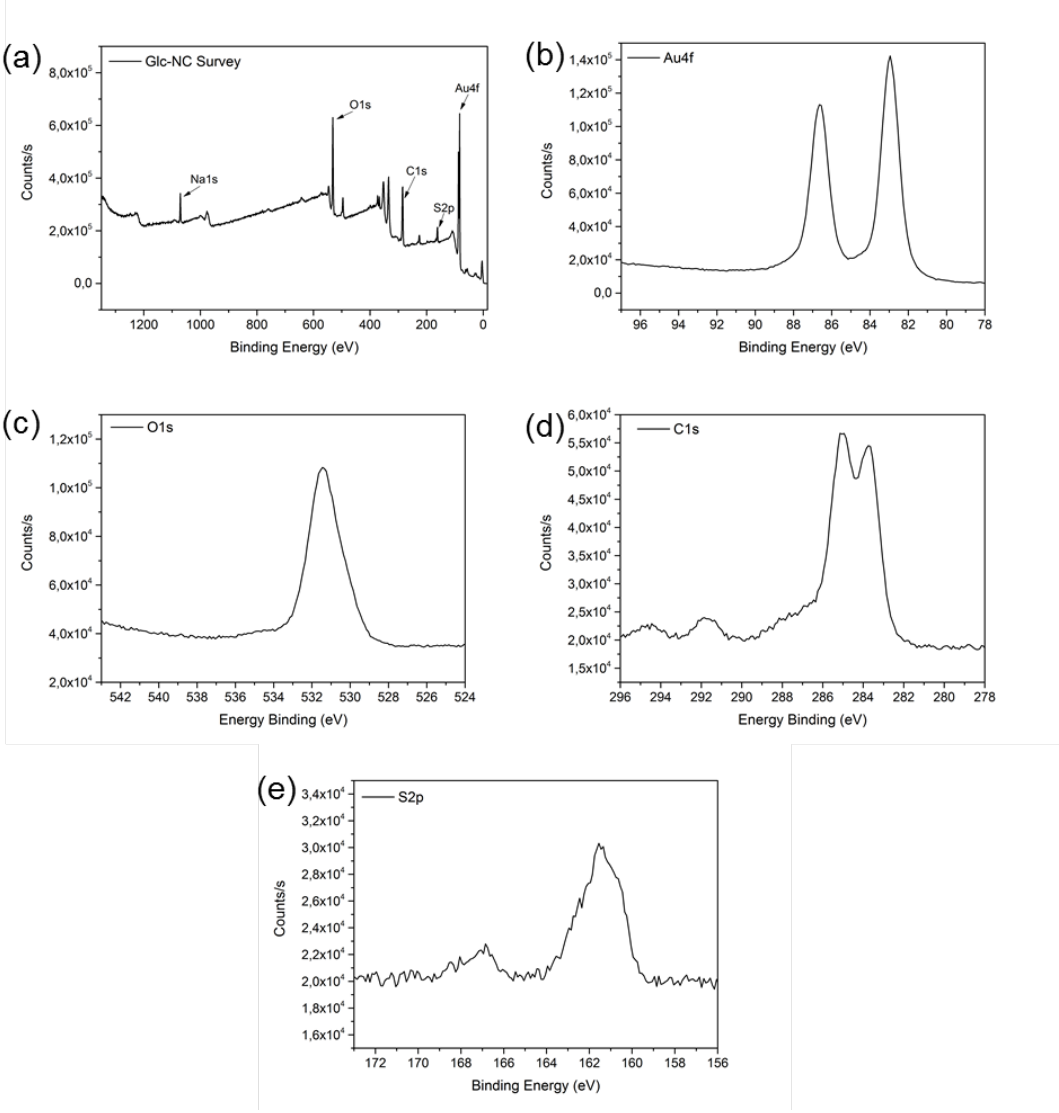


**Figure 2.6**. X-ray photoelectron spectroscopy data of **Glc-NCs**. a) Survey scan of **Glc-NCs**. b) Au4f, c) O1s, d) C1s, e) S2p, elemental scans of **Glc-NCs**.

**Table 2.2.** X-ray photoelectron spectroscopy data of **Glc-NCs** analysis from Figure 2.6.

| Element | Peak BE | FWHM eV | Area (P) counts/s.eV |
|---|---|---|---|
| **C1s** | 284.8 | 3.29 | 802670.4 |
| **O1s** | 531.59 | 3.02 | 1131512 |
| **S2p** | 161.78 | 1.78 | 161929.7 |
| **Au4f** | 83.52 | 2.82 | 2395402 |

The carbonyl signal is likely indicative of the oxidation of carbohydrate hydroxyls as 1-thio-glucose precursor contains no carbonyl group. C1s scan confirms the previous observation by showing a possible carboxylic acid present in the stabilizing agent due to the presence of an O-C=O binding energy band at 288.5 eV (Table 2.3).

**Table 2.3**. X-ray photoelectron spectroscopy analysis of **Glc-NCs** by chemical state.

| **Chemical state** | **Peak BE** | **Chemical state** | **Peak BE** | **Chemical state** | **Peak BE** |
|---|---|---|---|---|---|
| **C-C** | 284.8 | **C-O** | 531.5 | **Au-S** | 162.5 |
| **C-O-C** | 286 | **C=O** | 533 | | |
| **O-C=O** | 288.5 | | | | |

The IR showed the presence of some typical carboxylic acid bands such as the broad O-H stretching band at 3265 nm as well as a C=O stretching band at 1623 nm (Figure 2.7). This observation supports the hypothesis that the stabilizer contains a carboxylic acid due to the oxidation of the glucose in presence of the chloroauric acid.

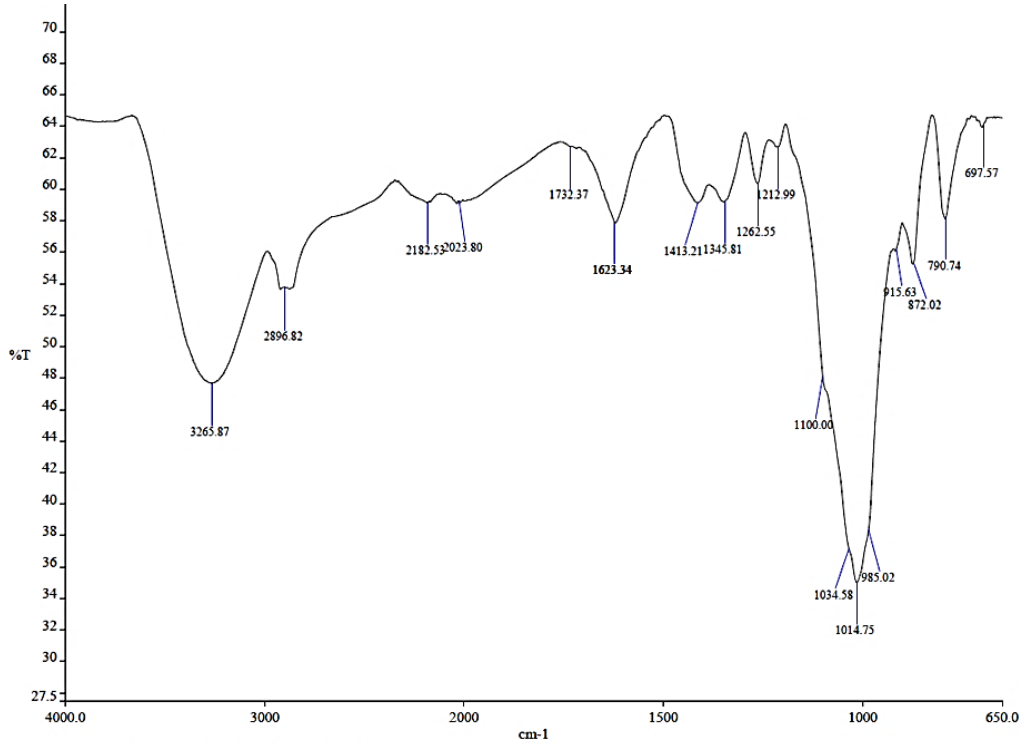


**Figure 2.7.** Infrared spectrum of **Glc-NCs**.

## 2.2.2. Surface modification strategies

In this section, surface functionalization of the synthesized gold nanoclusters is described. Two different methods were used to modify the nanocluster surface: through a coupling reaction to the carboxylic acids of the stabilizers and *via* a further thiol substitution to the gold core. The two possible functionalization pathways open up opportunities to biofunctionalize **Glc-NCs** for many applications.

### 2.2.2.1. Coupling reaction

To confirm the XPS and IR analyses, a coupling reaction with trifluoroethanol was performed since the formation fluorine functionalized **Glc-NCs** (**F@Glc-NCs**) can be monitored by $^{19}$F-NMR. Different reaction conditions were tested to obtain the desired stable product (Table 2.4). A large excess of different coupling reagents was used to ensure that all the carboxylic acids present on the nanoclusters reacted. The treatment of the nanoclusters with most coupling reagents resulted in severe aggregation. Activation with both 1-ethyl-3-(3-dimethylaminopropyl)carbodiimide (EDC) and *N*-hydroxysulfosuccinimide (sulfo-NHS) yielded stable nanoclusters. The water solubility of the modified carboxylate decreases upon *N*-hydroxysuccinimide (NHS) whereas it increases with sulfo-NHS due to the charged sulfonate groups. Phosphate-buffered saline (PBS) at pH 7.2-7.5 was chosen as reaction medium (Scheme 2.1). The reaction gave stable nanoclusters upon treatment with both five and 20 equivalents of the coupling reagent, therefore, 20 equivalents were chosen for the synthesis to ensure complete conversion.

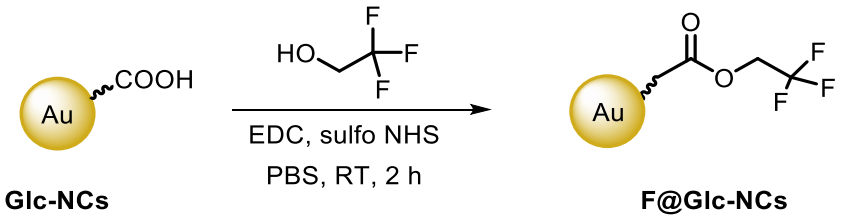


**Glc-NCs** **F@Glc-NCs**

**Scheme 2.1**. Functionalization of **Glc-NCs** by coupling trifluoroethanol to NC-surface carboxylic acid to yield **F@Glc-NCs**.

**Table 2.4.** Reaction conditions for the synthesis of **F@Glc-NCs**.

| Entry | Coupling reagents (eq) | Trifluoroethanol (eq) | Solvents | Observations |
|---|---|---|---|---|
| **1** | EDC + NHS (200 eq) | 200 | Water:DMF (1:1) | Aggregated |
| **2** | EDC + NHS (50 eq) | 50 | Water:DMF (1:1) | Aggregated |
| **3** | EDC + NHS (5 eq) | 200 | Water:DMF (1:1) | Aggregated |
| **4** | EDC + NHS (5 eq) | 200 | Water | Aggregated |
| **5** | DIC + NHS (5 eq) | 200 | Water | Aggregated |
| **6** | EDC + Sulfo NHS (5 eq) | 200 | PBS (75 mM) | Not aggregated |
| **7** | EDC + Sulfo NHS (20 eq) | 200 | PBS (75 mM) | Not aggregated |

After 30 min, $^{19}$F-NMR showed the appearance of the product peak along with the starting material (Figure 2.8 a). After dialysis for two days against milliQ water, only the product peak remained confirming the formation of the fluorinated product **F@Glc-NCs** (Figure 2.8 b).

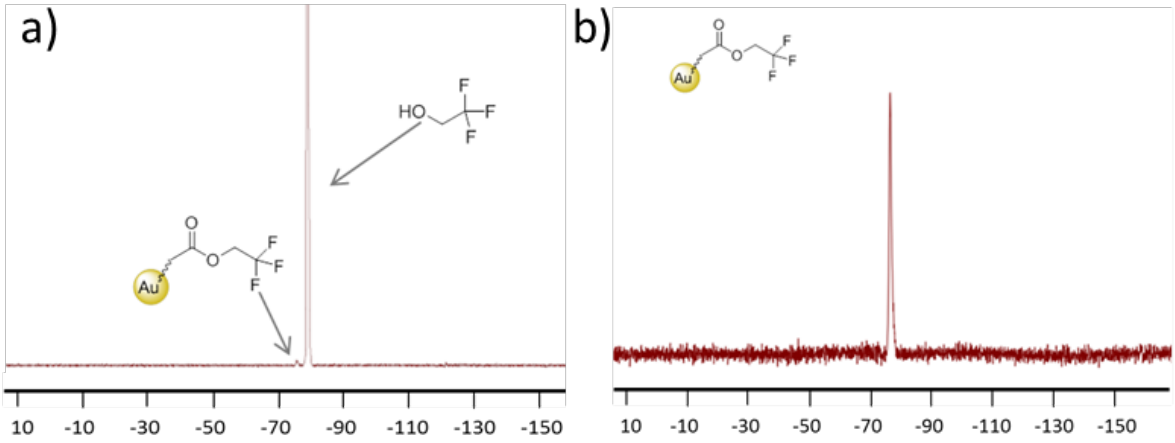


**Figure 2.8.** a) $^{19}$F-NMR (400 MHz, $H_2O$) spectrum after 5 min reaction showing one peak of the starting material and a small peak of **F@Glc-NCs**; b) $^{19}$F-NMR of **F@Glc-NCs** after dialysis showing one product peak.

To calculate the number of active sites per nanocluster, an internal standard (IS) was used. Purified **F@Glc-NCs** were mixed with 2.7 µmol CsF as an internal standard in an NMR tube and $^{19}$F-NMR was measured (Figure 2.9). By integrating the peaks of the sample and the internal standard, it was possible to obtain the concentration of fluorine in **F@Glc-NCs**. The integration IS:-$CF_3$ was 1.0:0.13.

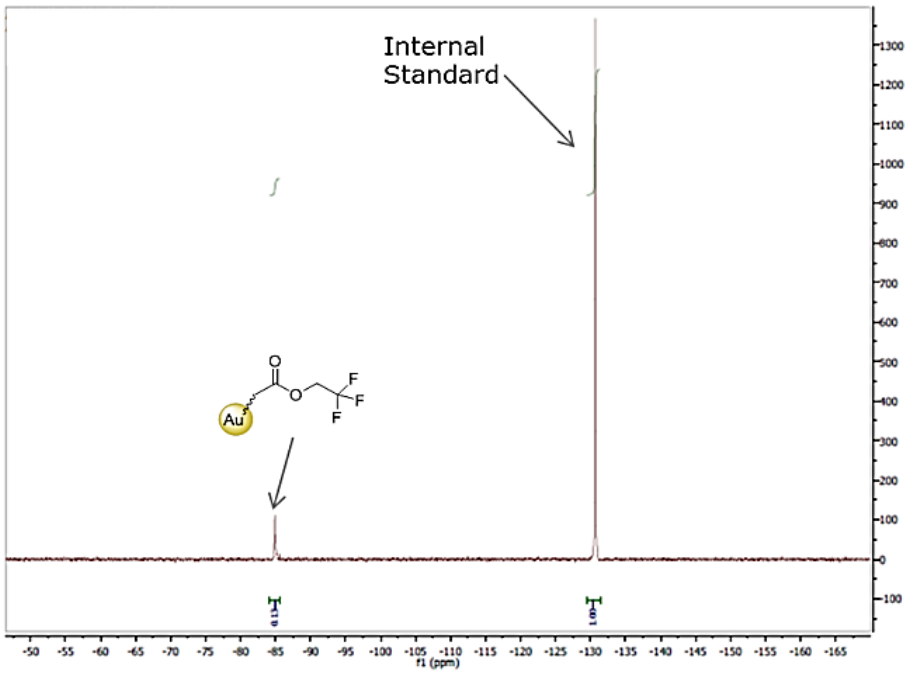


**Figure 2.9.** $^{19}$F-NMR (400 MHz, $H_2O$) of **F@Glc-NCs** with internal standard (CsF). The integration IS:-$CF_3$ was 1.00:0.13.

The gold concentration in the sample (832 nmol) was determined by Inductively Coupled Plasma Atomic Emission Spectrometer (ICP-AES). Considering the concentration of gold and -$CF_3$ in the sample, the number of gold atoms and -$CF_3$ stabilizers in the NMR sample were calculated.

To calculate the amount of -$CF_3$ per nanocluster, the number of gold atoms in one nanocluster needs to be estimated. Therefore, the nanocluster was considered as a sphere with diameter 2 nm and density ρ = 19.3 g/cm$^3$, using equation (1).

$$m = \frac{4}{3}\pi r^3 \rho \qquad (1)$$

From equation (1), the nanocluster mass obtained was $4.55 \cdot 10^{-20}$ g which resulted in 139 atoms per nanocluster, giving 20 -$CF_3$/Nanocluster.

Thus, it can be concluded that **Glc-NCs** can be functionalized *via* coupling to the carboxylic acid groups present on the surface and that there were 20 functionalities attached after completed conversion.

### 2.2.2.2. Thiol conjugation

To further exploit the surface functionalization of **Glc-NCs** *via* a direct thiol linkage to the gold core, a pentylthiol mannoside was synthesized (Scheme 2.2). Peracetylated mannose **1** was coupled with 5-chloropentanol in the presence of stoichiometric $BF_3.OEt_2$.The chloride was then converted to the acetylated thiol derivative **2** in the presence of KSAc.[148] Hydrolysis of the acetyl groups in basic conditions yielded the desired compound **3**.[149]

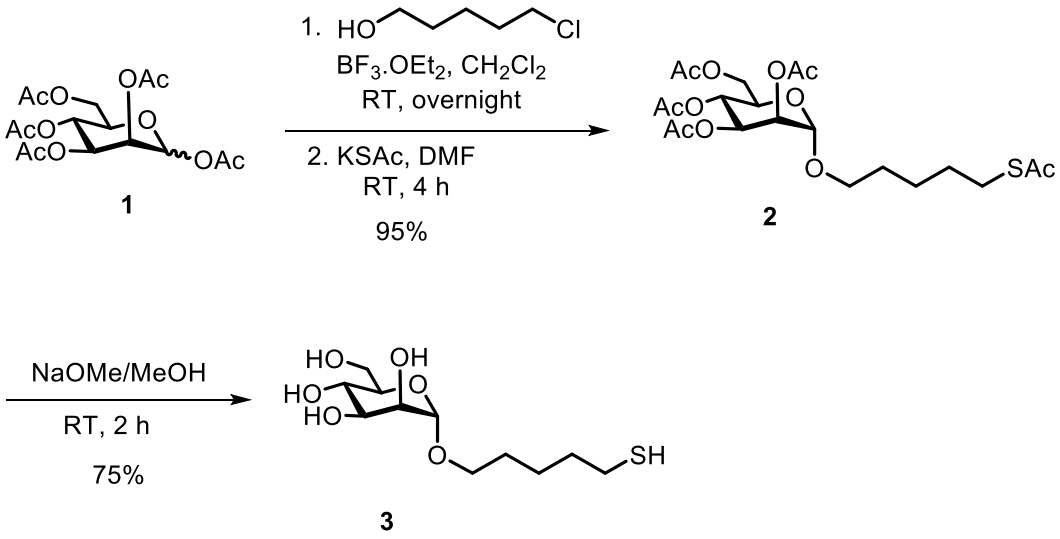


**Scheme 2.2.** Synthesis of pentylthiol mannoside **3**.

Pentylthiol mannoside **3** was incubated with **Glc-NCs** overnight at room temperature to yield **Man@Glc-NCs** (Scheme 2.3).

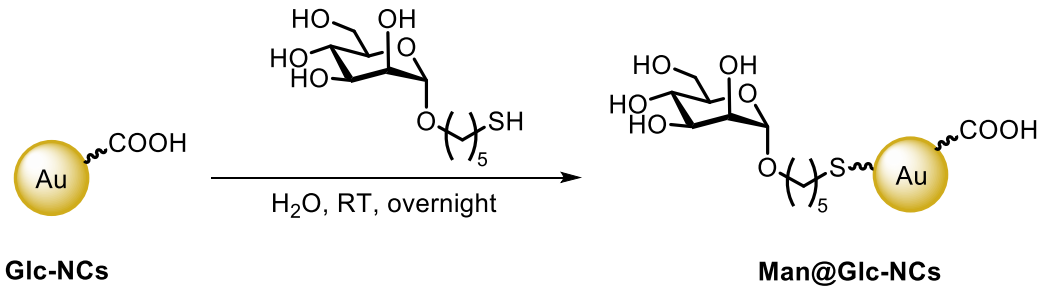


**Scheme 2.3. Glc-NCs** functionalization *via* thio-substitution of pentylthiol mannoside on the gold surface giving **Man@Glc-NCs**.

After purification by dialysis, the IR spectrum revealed two new peaks corresponding to the stretch of the C-H bonds of the linker at 2955 and 2855 nm (Figure 2.10).

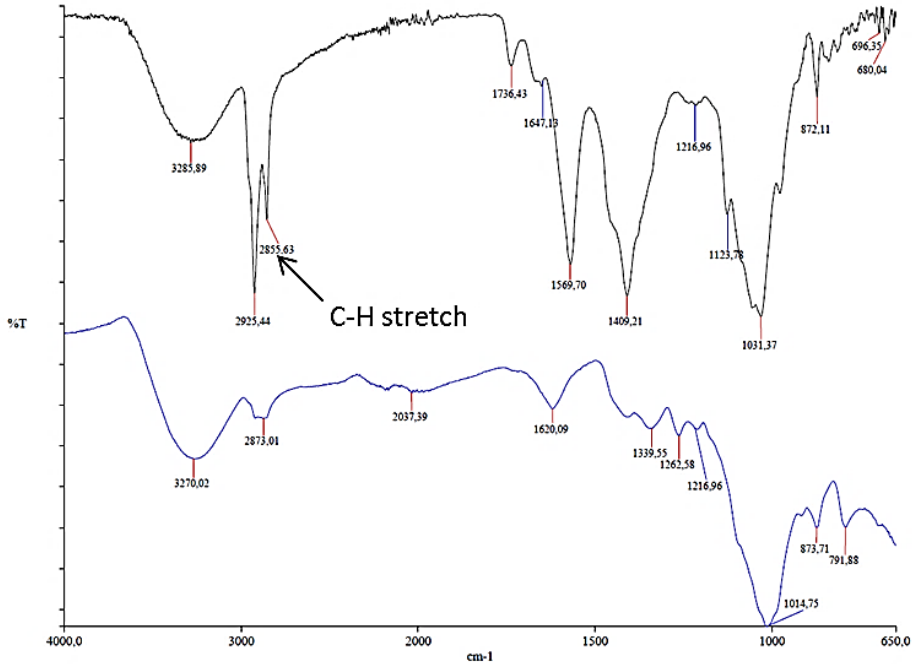


**Figure 2.10.** Infrared spectrum of **Glc-NCs** (below in blue) and **Man@Glc-NCs** (above in black). The **Man@Glc-NCs** shows peaks of the C-H stretch from the linker.

**Man@Glc-NCs** had the same monodisperse size and shape as non-functionalized **Glc-NCs**, as observed by TEM. The nanocluster size of 2.061 ± 0.003 nm was averaged on 129 counted nanoclusters (Figure 2.11).

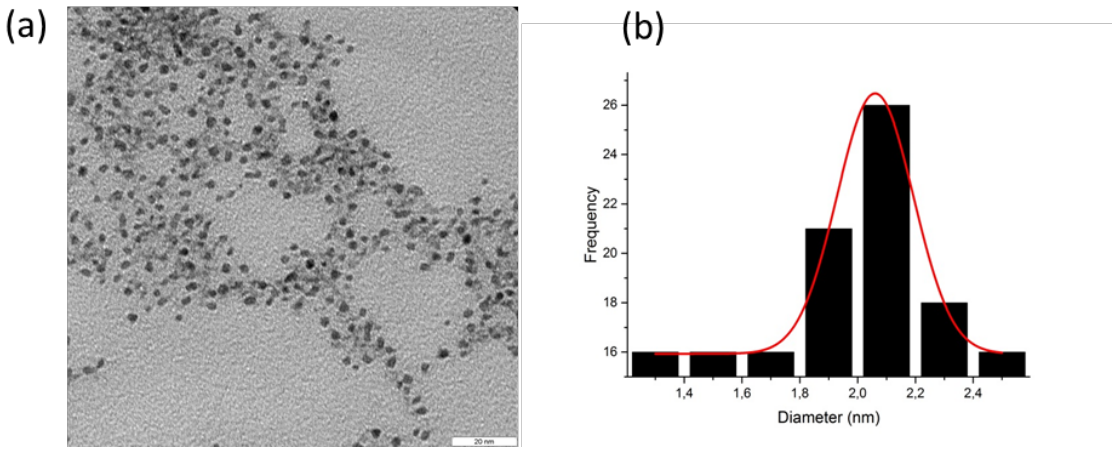


**Figure 2.11.** a) TEM image and b) size distribution of **Man@Glc-NC** considering 129 nanoclusters. The size of **Man@Glc-NCs** was 2.061 ± 0.003 nm. Scale bar = 20 nm.

Surface functionalization of mannose terminated linker on **Glc-NCs** (**Man@Glc-NCs**) was confirmed by performing an agglutination assay with mannose-binding lectin Concanavalin A (ConA). Only mannose functionalized nanoclusters were found to bind ConA, and aggregation was observed by the naked eye. Unfunctionalized **Glc-NCs** failed to aggregate since the oxidized thio-glucose was not recognized by ConA lectin (Figure 2.12).

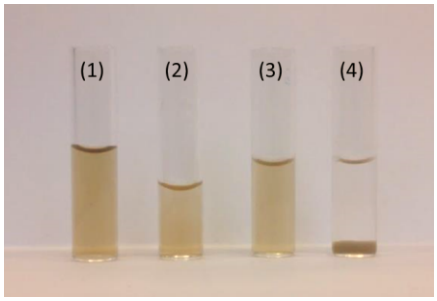


**Figure 2.12.** Vials containing (1) **Glc-NCs** (2) **Man@Glc-NC** (3) **Glc-NCs** + ConA (4) **Man@Glc-NCs** + ConA. Aggregation is only observed upon addition of ConA lectin to the sample containing mannose functionalized gold nanoclusters (4).

## 2.2.3. Cytotoxicity and cellular uptake

The cytotoxicity of the nanocluster was assessed by incubating the nanoclusters for one day with the mouse cell line L929 as proof-of-concept study. Cell viability was measured using the MTS [3-(4,5-dimethylthiazol-2-yl)-5-(3-carboxymethoxyphenyl)-2-(4-sulfophenyl)-2H-tetrazolium inner salt] assay.[150] The cytotoxicity of **Glc-NCs**, **CTAB-NCs** and **THPC-NCs** was compared showing that **CTAB-NCs** were toxic even at low concentrations (25 – 0.2 $\mu$M), whereas both **THPC-NCs** and **Glc-NCs** did not show any toxicity even at the high concentration (500 $\mu$M) (Figure 2.13).

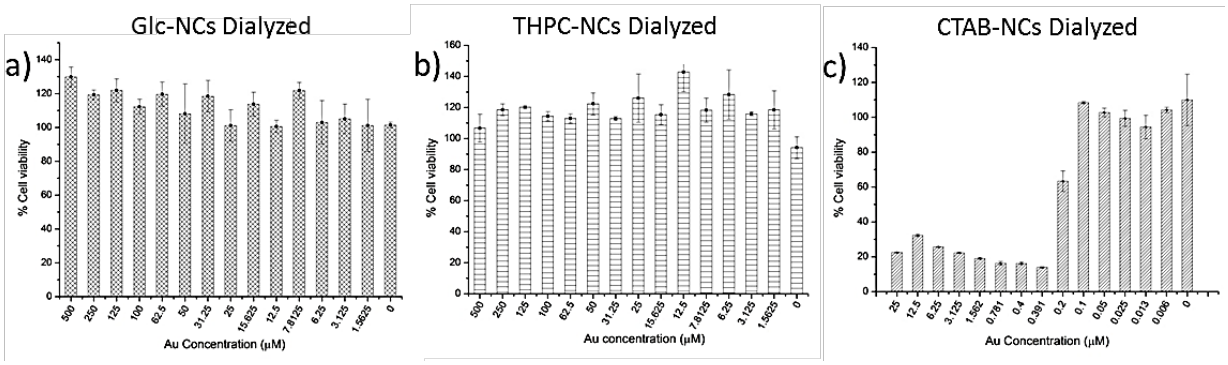

**Figure 2.13.** Cellular cytotoxicity assay of a) **Glc-NCs**, b) **THPC-NCs** and c) **CTAB-NCs** after incubation for one day with L929 cell line.

To test whether the free stabilizers were affecting the cytotoxicity, both **Glc-NCs** and **THPC-NCs** were incubated with the cells after synthesis without dialysis purification. **Glc-NCs** did not show cytotoxicity at any concentration (Figure 2.14 a), whereas **THPC-NCs** were toxic at 100 $\mu$M resulting in a 60% drop in cell viability (Figure 2.14 b). Thus, **Glc-NCs** are suitable for biological experiments even without purification.

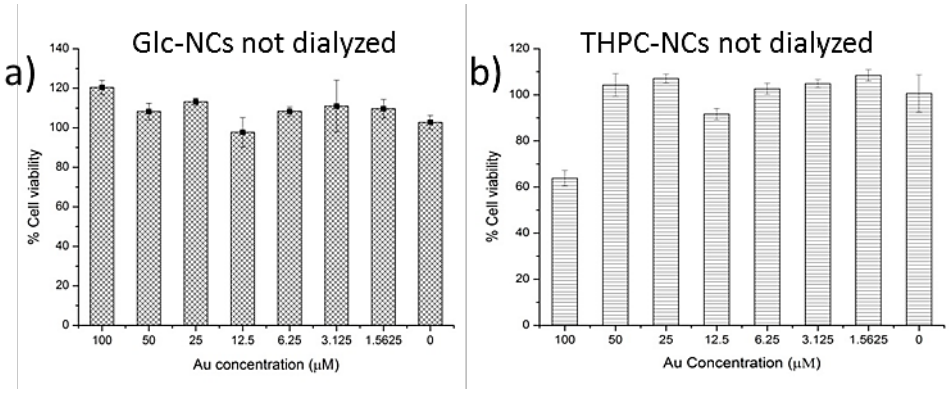


**Figure 2.14.** Cellular viability of a) **Glc-NCs** and b) **THPC-NCs** without purification after incubation of the nanoclusters for one day with L929 cell line. **THPC-NCs** without dialysis showed toxicity at 100 µM.

To further explore the potential of **Glc-NCs** as nanocarriers, cellular uptake of the nanoclusters was studied by incubating 12.5 and 25 $\mu$M **Glc-NCs** with the same cell line. After 24 h, the cells were washed with PBS buffer and then treated with aqua regia to transform the gold nuclei into gold ions. ICP-AES confirmed that the **Glc-NCs** were cell permeable and $10^8$-$10^9$ gold atoms per cell were detected (Figure 2.15). These results confirm the great potential of **Glc-NCs** for cellular delivery applications.

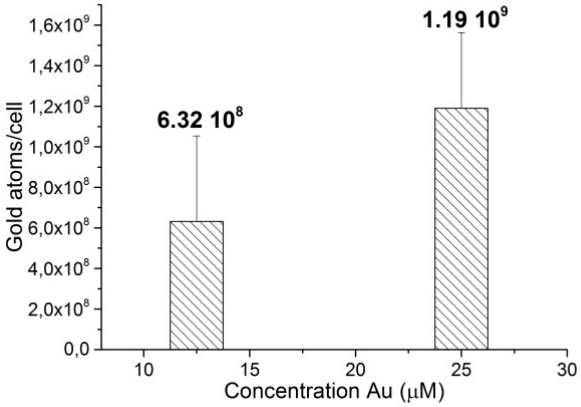

**Figure 2.15.** Cellular uptake of **Glc-NCs** when incubated with L929 cells for one day. An uptake of $10^8$-$10^9$ gold atoms per cell was measured with ICP-AES.

A straightforward, robust and efficient one-pot method to prepare glucose-stabilized gold nanoclusters was developed. The resulting 2 nm nanoclusters are monodisperse and more stable than gold nanoclusters synthesized by other methods. Functionalization of the **Glc-NCs** was achieved either *via* coupling to the carboxylic acid of the stabilizing agent or substitution with a thio-functionalized molecule. The **Glc-NCs** are non-toxic, and taken up by L929 cells. New opportunities for drug delivery applications will be described in Chapter 3.

## 2.2.4. *In vivo* biodistribution using positron electron tomography (PET)

Positron-emission tomography (PET) is a nuclear medicine imaging technique that monitors metabolic processes in the body. This technique is able to detect pairs of gamma rays that are emitted by a radiotracer, which is introduced into the body on a biologically active molecule.

To better understand the metabolic fate of **Glc-NCs**, radiolabeling was chosen as it allows for sensitive, reliable *ex* and *in vivo* imaging with high temporal resolution. Copper-64 has favorable decay characteristics ($t_{1/2}$ = 12.7 h, $\beta^+$ = 19%; $\beta$ = 40%; electron capture 40%) and has received significant attention in the PET field thanks to the well-established coordination chemistry of copper that allows for its complexation with a wide variety of chelators. These chelators can also be easily linked to biomolecules such as antibodies, proteins, peptides etc.[151] The nanoclusters were functionalized with 2-*S*-(4-aminobenzyl)-1,4,7-triazacyclononane-1,4,7-triacetic acid (p-$NH_2$-Bn-NOTA) as ligand for $^{64}$Cu(II) because of the presence of carboxylic groups that would not change the negative surface charge of the pristine nanoclusters.

### 2.2.4.1. Synthesis of NOTA functionalized gold nanoclusters

**Glc-NCs** were firstly functionalized with p-$NH_2$-Bn-NOTA to obtain **NOTA@Glc-NCs** as shown in Scheme 2.4. During this synthesis, several problems arose while trying to obtain stable NOTA functionalized nanoclusters. When the nanoclusters were

functionalized with a high concentration of p-$NH_2$-Bn-NOTA, the nanoclusters aggregated. Hence, it is important to estimate the number of nanoclusters in the reaction solution (using UV or ICP-AES) in order to add the same amount of chelator ligands. This problem was solved by performing the conjugation reaction under sonication at 0 °C. Completion of the reaction was observed in 2 h using EDC and sulfoNHS as coupling reagents in the presence of PBS buffer. Dialysis against MilliQ water for two days was carried out to purify the nanoclusters for further characterization.

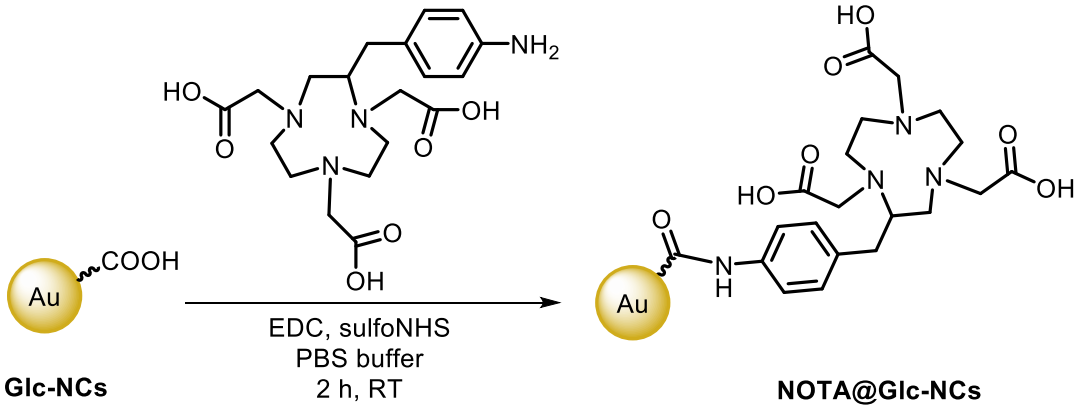


**Scheme 2.4.** Conjugation of p-NH2-Bn-NOTA chelator to **Glc-NCs** to yield **NOTA@Glc-NCs**.

The **NOTA@Glc-NCs** were characterized with IR by comparing the non-functionalized nanoclusters with the functionalized ones (Figure 2.16). The functionalized nanoclusters showed additional peaks from the chelator ligand such as C-H stretching (2919 $cm^{-1}$), C=O (1730 $cm^{-1}$) and C-O (1260 $cm^{-1}$) from carboxylic acids present on the chelator, and C=O (1654 $cm^{-1}$) from the amide bond formed during the reaction, which confirms the successful functionalization of the nanoclusters.

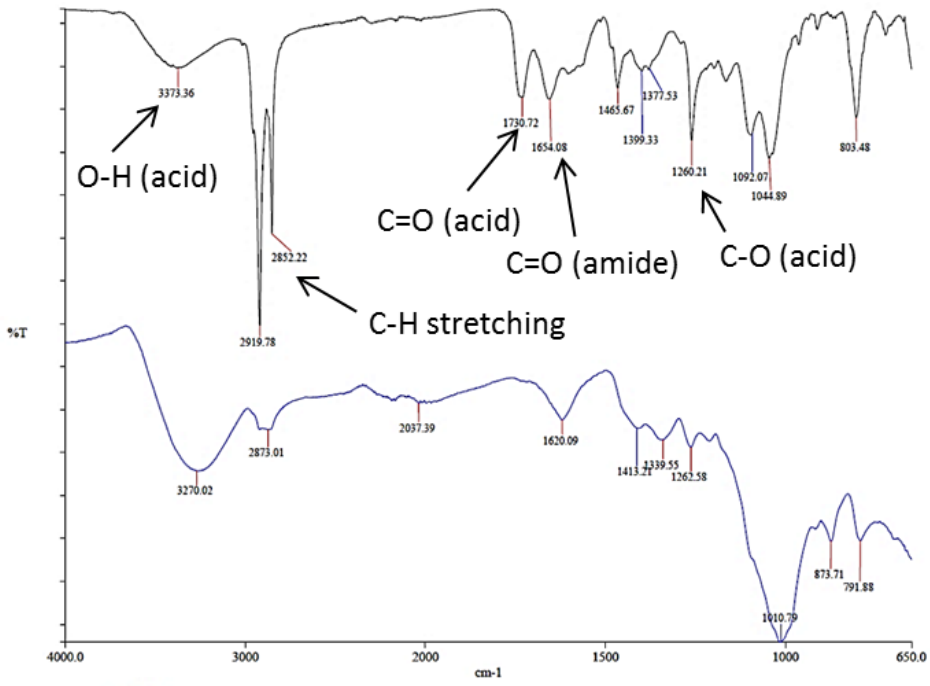


**Figure 2.16.** IR spectra of pristine **Glc-NCs** (blue) and **NOTA@Glc-NCs** (black)

TEM imaging of the purified **NOTA@Glc-NCs** showed the same size and morphology when compared to the pristine **Glc-NCs** (Figure 2.17).

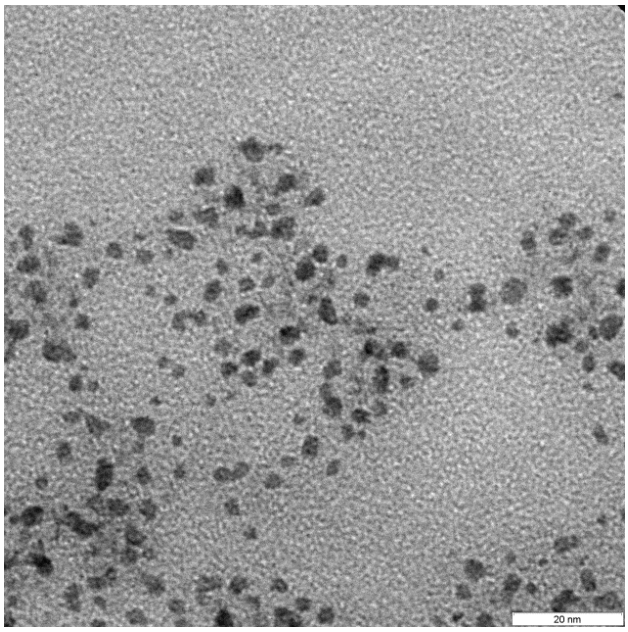


**Figure 2.17.** TEM image of purified **NOTA@Glc-NCs**. Scale bar = 20 nm.

The samples were sent to the group of Dr. Holger Stephan at the Institute of Radiopharmaceutical Cancer Research, Helmholtz-Zentrum Dresden - Rossendorf

(HZDR) for biodistribution studies in a mouse model. **NOTA@Glc-NCs** underwent radiolabeling and accumulated in all the organs except for the brain. After 24 h, the nanoclusters were excreted in high amount, showing the high potential of this material for biomedical applications.

### 2.2.4.2. $^{64}$Cu(II)-labeling and in vitro stability[a]

The **NOTA@Glc-NCs** were labelled with $^{64}$Cu(II) to yield **$^{64}$Cu(II)-NOTA@Glc-NCs** (Figure 2.18) by adding 20 nmol gold nanocluster sample to 50 MBq of Cu[$^{64}$Cu]$Cl_2$ in 2-[*N*-morpholino]-ethansulfonic acid (MES) buffer (pH 5.0) at 37 °C for 3 h. Subsequently, 8-10 fold excess of EDTA was added to remove the unbound copper. Radio thin layer chromatography (radio TLC) chromatogram showed the successful radiolabelling of **NOTA@Glc-NCs** (Figure 2.19 a).

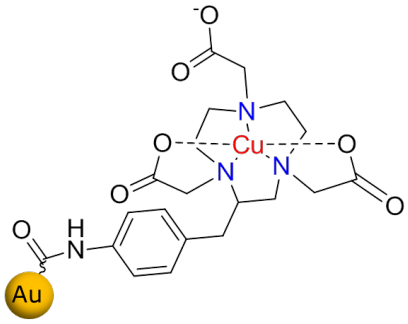


**Figure 2.18.** Structure of **$^{64}$Cu(II)-NOTA@Glc-NCs**.

The **$^{64}$Cu(II)-NOTA@Glc-NCs** were then purified using PD 10 size exclusion column by collecting 200 µL aliquots. Radio TLC chromatogram using instant thin layer chromatography with salicylic acid in citrate buffer at pH 5.0, showed that **$^{64}$Cu(II)-NOTA@Glc-NCs** was further separated from unbound copper that formed a complex with citrate. The radiolabelling yield (RCY) of **$^{64}$Cu(II)-NOTA@Glc-NCs** was 46%.

[a] Radiolabelling was carried out by Dr. Kritee Pant (Institute of Radiopharmaceutical Cancer Research, Helmholtz-Zentrum Dresden - Rossendorf (HZDR)).

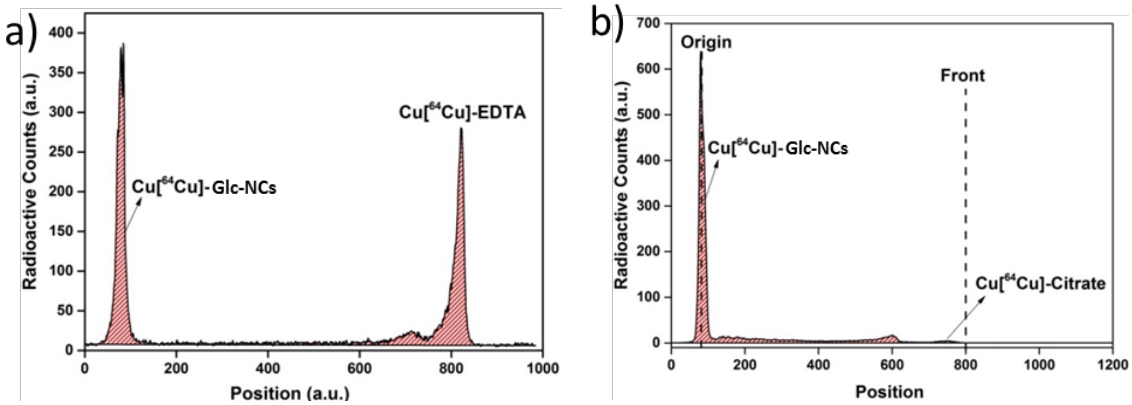


**Figure 2.19.** Radio TLC chromatograms of a) **$^{64}$Cu(II)-NOTA@Glc-NCs** after the reaction was completed and EDTA was added to capture unbound copper, and b) **$^{64}$Cu(II)-NOTA@Glc-NCs** after column purification using instant thin layer chromatography with salicylic acid in citrate buffer.

The stability of the copper complex on **$^{64}$Cu(II)-NOTA@Glc-NCs** was assessed in serum in order to determine whether the radiotracer was released in biological medium over time. The **$^{64}$Cu(II)-NOTA@Glc-NCs** were purified using a PD 10 column and subsequently incubated with 1 mL of serum. Aliquots (150 µL) were taken at different time points and centrifuged using 10 kDa filters in order to calculate the bound/unbound copper on the sample. The complex was stable for the first 4 h and released only around 10% of copper after 24 h of incubation in serum (Figure 2.20). These results proved the stability of the copper complex on **$^{64}$Cu(II)-NOTA@Glc-NCs** and allowed for the injection of the material in mice for *in vivo* experiments.

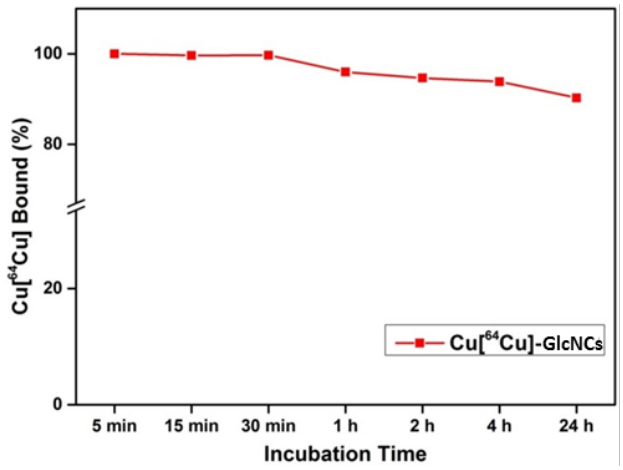


**Figure 2.20.** Analysis of copper release on **$^{64}$Cu(II)-NOTA@Glc-NCs** at different time points when incubated in serum. The low release of the radiotracer allows for the use in mouse experiments.

Radiometric titration was performed in order to obtain the concentration of copper in **$^{64}$Cu(II)-NOTA@Glc-NCs**. An increasing amount of copper was added to 2 nmol of **NOTA@Glc-NCs** based on gold concentration. An excess of EDTA was added to remove the unspecific bound copper. The percentage of bound copper in **$^{64}$Cu(II)-NOTA@Glc-NCs** was calculated as nmoles of copper added, giving 0.24 nmol of bound $^{64}$Cu per nmol of gold (Figure 2.21).

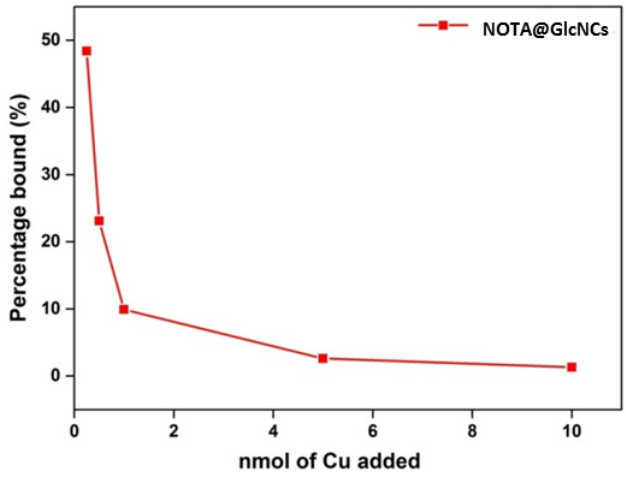


**Figure 2.21.** Radiometric titration to calculate the bound copper in **$^{64}$Cu(II)-NOTA@Glc-NCs**. Results showed 0.24 nmol of bound $^{64}$Cu per nmol of gold in **$^{64}$Cu(II)-NOTA@Glc-NCs**.

### 2.2.4.3. Biodistribution studies[b]

The fully characterized **$^{64}$Cu(II)-NOTA@Glc-NCs** were used for biodistribution studies in healthy Wistar rats. For the first experiment, the radiolabeling of **NOTA@Glc-NCs** was performed 3 h prior to injection in rats. To **$^{64}$Cu(II)-NOTA@Glc-NCs,** 1:5 mol excess of EDTA was added to remove the unspecifically bound copper and PD 10 size exclusion column was used to purify the sample. The **$^{64}$Cu(II)-NOTA@Glc-NCs** were then injected in healthy Wistar mice and biodistribution studies were performed in triplicates after 5 min, 1 h and 24 h of injection. Even five minutes after injection, **$^{64}$Cu(II)-NOTA@Glc-NCs** were accumulated in many organs probably due to the optimum blood half-life (Figure 2.22). The high accumulation of **$^{64}$Cu(II)-NOTA@Glc-NCs** in the kidneys can be

[b] Biodistribution studies were carried out by the group of Dr. Holger Stephan group (Institute of Radiopharmaceutical Cancer Research, Helmholtz-Zentrum Dresden - Rossendorf (HZDR)).

explained with the excretion of around 7% of the injected dose (ID) through the urine after 5 min, which is typical for ultrasmall nanomaterials (Figure 2.23).

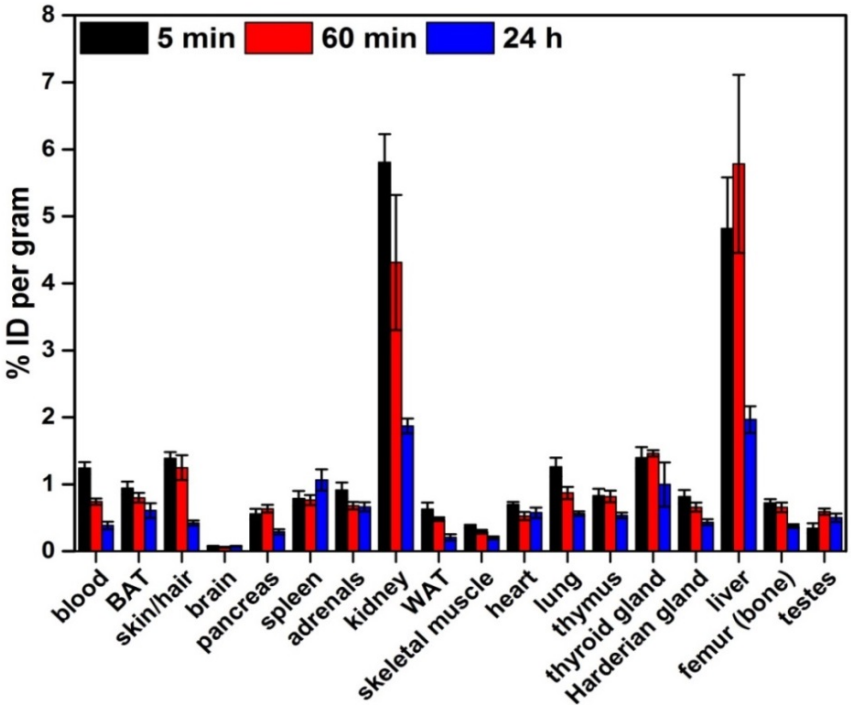


**Figure 2.22.** Whole-body biodistribution of **$^{64}$Cu(II)-NOTA@Glc-NCs** in healthy Wistar rats after 5 min, 60 min and 24 h of injection. Radiolabelling was performed 3 h prior to injection. Data are represented as a percentage of injected dose per gram.

Sixty minutes after injection, the biodistribution of **$^{64}$Cu(II)-NOTA@Glc-NCs** is similar to that five minutes after injection. The accumulation in the bone can be explained by affinity of **$^{64}$Cu(II)-NOTA@Glc-NCs** to hydroxyapatite or even to macrophages. A significant reticuloendothelial system (RES) uptake was observed, which can be explained with the high anionic charge of **$^{64}$Cu(II)-NOTA@Glc-NCs** that may increase uptake.[152] Overall, it was noticed that the accumulation in brain was negligible, since crossing the blood brain barrier is a very complex process and would probably require further surface bioconjugation.

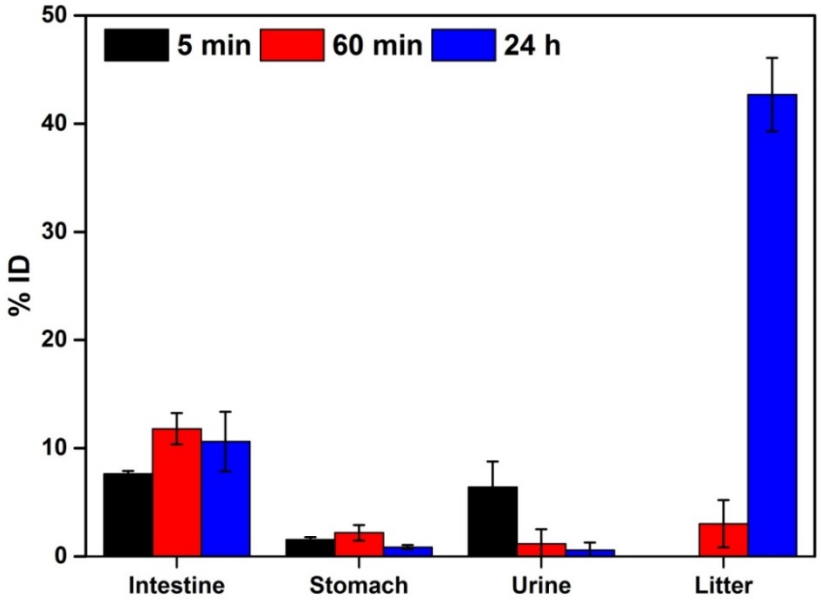


**Figure 2.23.** Elimination of **$^{64}$Cu(II)-NOTA@Glc-NCs** through the intestine (hepatobiliary) and urine (renal) after 5 min, 60 min and 24 h of injection. Radiolabelling was performed 3 h prior to injection. Data are represented as a percentage of injected dose per gram.

It is important to notice that 1 h after injection, the **$^{64}$Cu(II)-NOTA@Glc-NCs** were accumulated in high amount in the liver. Nevertheless, 24 h after injection, the accumulation of **$^{64}$Cu(II)-NOTA@Glc-NCs** in the different organs was overall decreased (Figure 2.22), and almost 50% was excreted *via* hepatobiliary pathway in the feces (Figure 2.23). **Glc-NCs** can be used for biomedical applications, for their accumulation capacity in many organs of the body (except for the brain) and for the ability to be cleared mostly from the body 24 h after injection.

A second experiment was carried out by radiolabeling **NOTA@Glc-NCs** 24 h prior to injection. The results (Figure 2.24) did not coincide with the previous ones (Figure 2.22). Stirring for 24 h at room temperature after radiolabeling caused aggregation that was visually detected by the presence of black. The high accumulation of **$^{64}$Cu(II)-NOTA@Glc-NCs** in lungs as well as in spleen and the low accumulation in all the other organs also can be explained by the particle aggregation (Figure 2.24).[153]

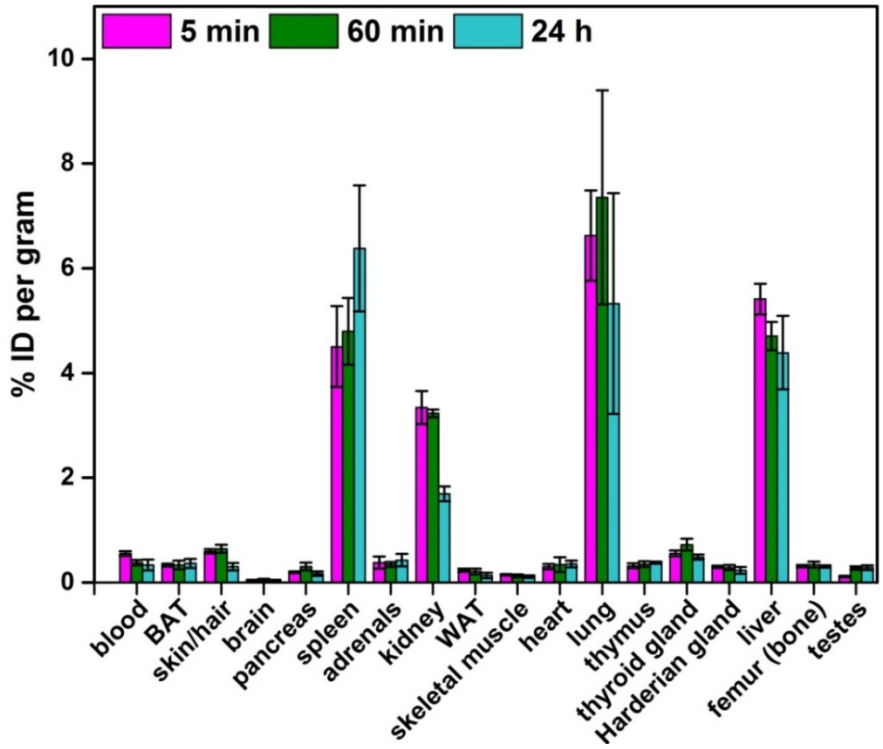


**Figure 2.24.** Biodistribution of **$^{64}$Cu(II)-NOTA@Glc-NCs** in healthy Wistar rats after 5 min, 60 min and 24 h of injection. Radiolabelling was performed 24 h prior to injection with no further purification. Data are represented as a percentage of injected dose per gram.

Moreover, **$^{64}$Cu(II)-NOTA@Glc-NCs** were excreted in a much lower amount compared to the previous experiment. This can be clearly seen by the litter measurement after 24 h, that is much lower (around 9%) compared to the previous experiment (around 50%). In this second experiments the **$^{64}$Cu(II)-NOTA@Glc-NCs** were not cleared from the body as in the previous assay due to the presence of aggregates in certain organs that could not be excreted. To improve this, stability studies will be carried out in order to obtain a sample that could be stored after radiolabelling.

Nevertheless, the first experiment showed that **$^{64}$Cu(II)-NOTA@Glc-NCs** has high potential to be applied in biomedical applications. As the nanoclusters are able to accumulate in many organs, the introduction of a targeting agent would direct the sample to a specific organ. Moreover, upon conjugation with a drug, the nanoclusters could be used for targeted delivery and thereby reduce side effects because of less administration and body clearance after targeted delivery.

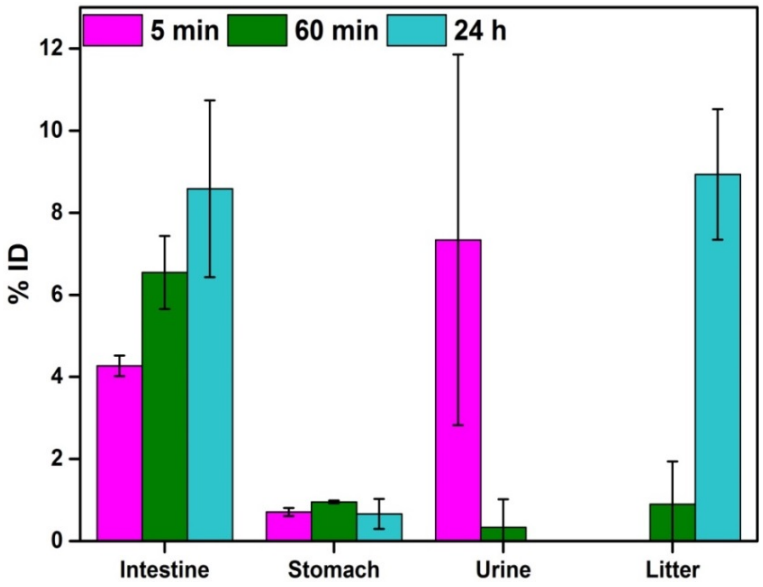


**Figure 2.25.** Elimination of $^{64}$Cu(II)-NOTA@Glc-NCs through the intestine (hepatobiliary) and urine (renal) after 5 min, 60 min and 24 h of injection. Radiolabelling was performed 24 h prior to injection with no further purification. Data are represented as a percentage of injected dose per gram.

# 2.3. Conclusion and outlook

In this chapter, a straightforward, robust and efficient one-pot method was developed to prepare glucose-stabilized gold nanoclusters. The resulting 2 nm nanoclusters do not possess a plasmon resonance, are monodisperse and more stable than gold nanoclusters synthesized by other methods (THPC and CTAB methods). Surface characterization analyses showed the presence of a carboxylic acid in the stabilizing agents due to the oxidation of thioglucose precursor. This carboxylic acid can be exploited for **Glc-NCs** functionalization *via* coupling with alcohols or amines. Further thiol conjugation on the gold core was achieved by the addition of a thiol functionalized carbohydrate. The pristine **Glc-NCs** showed no cytotoxicity and were able to penetrate L929 cells. *In vivo* studies in mice were performed in order to evaluate the bioaccumulation of **Glc-NCs** in different organs. For this purpose, **Glc-NCs** were radiolabeled with copper prior to injection. Results showed that radiolabeled **Glc-NCs** were able to reach and accumulate in all the organs except for the brain, and were also excreted after 24 h (almost 50% through the litter). **Glc-NCs** hold great potential as nanocarriers that can be functionalized using different strategies and the carrier is neither biologically active nor cytotoxic.

A targeting moiety can be used to functionalize **Glc-NCs** together with a drug in order to create a bimodal system. In this way, the side effects of the drug will be reduced as fewer administrations are required. Since the **Glc-NCs** are excreted out of the body in a relatively short time, the plasma half-life could be increased by using different strategies such as changing the surface charge of the nanoparticles.[154]

# 2.4. Experimental section

## 2.4.1. General methods

All **reagents** were commercially purchased and used without further purification. Anhydrous solvents were obtained from a Dry Solvent System (jcmeyer-solvent system). Air sensitive reactions were carried out using oven-dried glassware and under an atmosphere of argon or nitrogen.

Thin-layer **chromatography** (TLC) was carried out on ALUGRAM® Xtra SIL plates pre-coated with silica gel of 0.20 mm thickness (Macherey-Nagel). TLC spots were visualized either under UV irradiation (254/366 nm) or by dipping the TLC in sugar stain (0.1% (v/v) 3-methoxyphenol, 2.5% (v/v) sulfuric acid in EtOH). Flash column chromatography was carried out using silica (Sigma Aldrich Silica Gel 60, 230 – 400 mesh).

**Lyophilized** water containing samples were performed using an Alpha 2-4 LD Lyophilizer (Christ, Osterode am Harz, Germany).

**$^{1}$H, $^{13}$C and $^{19}$F** and two dimensional **NMR** data were obtained on Bruker ECX 400 MHz, Varian 400 MHz, Varian 600 MHz, and Bruker AVANCE III 700 MHz NMR spectrometers.

**FTIR** spectra were recorded on a Spectrum 100 FT-IR spectrometer (Perkin Elmer). The samples were spotted as a solid on the detector before measurements.

**UV/Vis** spectra were recorded on an UVmini-1240 UV/Vis spectrophotometer (Shimazu).

**Mass spectra** were obtained using an electrospray ionization (ESI) interface on an Agilent LC/MSD TOF system.

**Transmission electron microscopy** (TEM) measurements were performed on a Zeiss EM 912 Omega. The samples were prepared by immersion of grids into a small volume of the sample and subsequent solvent evaporation in a dust protected atmosphere.

**High resolution TEM** imaging was performed using a Tecnai F20 X-Twin transmission electron microscope at GFZ Potsdam. The TEM is equipped with a field emission gun as electron emitter. TEM bright-field images were acquired as energy filtered images using a Gatan imaging filter GIF. A 20 eV window was applied to the zero-loss peak. Data were evaluated with the Gatan Digital Micrograph software package.

**Dynamic light scattering (**DLS) measurements were carried out at a scattering angle of 173° with a Malvern Zeta Nanosizer working at 4-mW He–Ne laser (633 nm). The **Glc-NCs** were measured in MilliQ water.

**ζ potential** was measured using a Malvern Zetasizer instrument in order to obtain the electrophoretic mobility of nanoparticles at different times of dialysis against MilliQ water. The Helmholtz-Smoluchowski equation was used to correlate the measured electrophoretic mobilities to the zeta potentials. Three replicates of each sample were measured six times at 25 °C in MilliQ water.

**X-ray Photoelectron Spectroscopy** (XPS) measurements were carried out with a Thermo Scientific K-Alpha X-ray Photoelectron Spectrometer. A monochromatic AlKα radiation (hν = 1486.6 eV) was used. A 200 eV analyzer pass energy and a 1 eV energy step size were used in survey scan measurements. Element scans were performed with a 50 eV analyzer pass energy and a 0.1 eV energy step size. All the obtained binding energies were referenced to carbon 1s peak at 284.8 eV. The samples were prepared on gold thin film substrates.

**Inductively Coupled Plasma Atomic Emission Spectrometry** (ICP-AES) for silicon concentration determination was performed on an Optima 8000; Perkin Elmer¸ Massachusetts; USA. Samples (1 mL) were diluted to a total volume of 10 mL using aqueous aqua regia. An external calibration series from 0.1 mg/L to 5 mg/L was prepared using Au standard solution. The average of 3 measurements was obtained and the initial dilution was back-calculated.

## 2.4.2. Synthetic chemistry methods

### 2.4.2.1. Nanoparticle synthesis

**Glucose-based gold nanoclusters (Glc-NCs)**

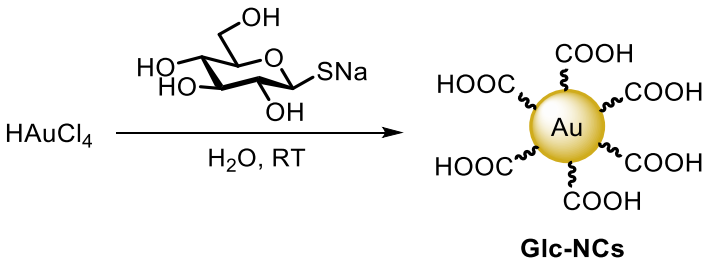


1-thio-*β*-D-glucose sodium salt in MilliQ water (80.0 µL, 41.2 mM) was added to $HAuCl_4$ (1.0 mL, 2.9 mM) at room temperature. In a few seconds a change in color from yellow to brownish was observed indicating the formation of the gold nanoclusters. The solution was dialyzed in two cycles of 1.5 L of MilliQ water or filter centrifuged using Amicon Ultra 15 mL tubes (3000*g*, 30 min, three times).

**THPC-based gold nanoclusters (THPC-NCs)**

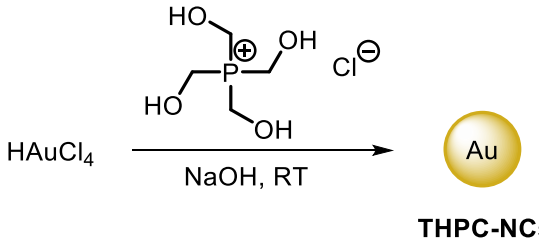


As described previously,[145] a solution of NaOH (1.5 mL, 0.2 M) was added to 45.5 mL of ultrapure water and stirred with the reducing agent tetrakis(hydroxymethyl)phosphonium chloride (THPC, 1 mL of a solution of 0.3 mL of 80% aqueous solution diluted to 25 mL with ultrapure water). The mixture was stirred for 5 min before the addition of $HAuCl_4$ (2 mL, 25 mM). The solution turned to a brown-orange color. The nanoclusters were further purified by two cycles of dialysis against 1.5 L of MilliQ water.

**CTAB-based gold nanoclusters (CTAB-NCs)**

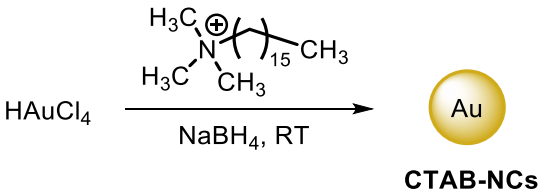


As described previously,[146] 10 mL of a solution of gold nanoclusters, $HAuCl_4$ (250 nM) was mixed with cetyltrimethylammonium bromide (CTAB, 75 mM) and afterwards reduced by $NaBH_4$ (600 nM). The reaction mixture was stirred for 5 min allowing the escape of the gas formed during the reaction. The nanoclusters were purified by two cycles of dialysis against 1.5 L of MilliQ water.

**Trifluoroethanol functionalized nanoclusters (F@Glc-NCs)**

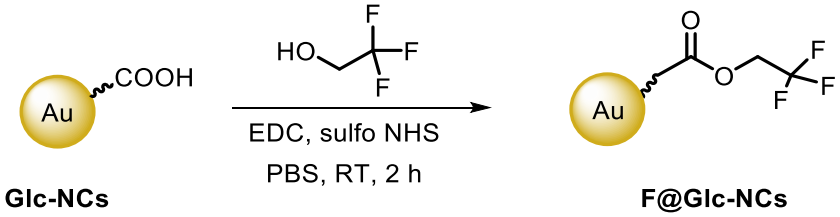


A solution of **Glc-NCs** (1.0 mL, 0.4 µmol) was mixed with 1 mL of PBS. The resulting solution was diluted with MilliQ water to 10 mL and then 1-ethyl-3-(3-dimethylaminopropyl)carbodiimide (EDC, 1.4 mg, 7.2 µmol) and *N*-hydroxysulfosuccinimide (sulfo-NHS, 1.6 mg, 7.2 µmol) were added under stirring. The reaction was allowed to stir for 5 min after which 2,2,2-trifluoroethanol (5.15 µl, 0.07 mmol) was added and let react under stirring for 2 h. The **F@Glc-NCs** were purified twice against 1.5 L MilliQ water.

Concentration of both gold and -$CF_3$ in the NMR tube.

| **NMR Tube** | **Gold** | **-$CF_3$** |
|---|---|---|
| **Concentration** | 832 nmol | 117 nmol |
| **Number of atoms/molecules** | $5 \cdot 10^{17}$ atoms | $7 \cdot 10^{16}$ molecules |

**Mannose functionalized nanoclusters (Man@Glc-NCs)**

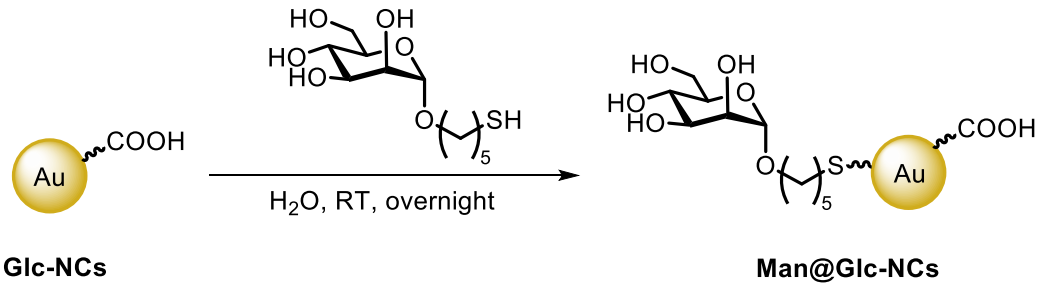


To a solution of **Glc-NCs** (1.0 mL, 2.6 mM), the synthesized thio-linked mannose in MilliQ water (2.5 mg, 8.7 µmol) was added and the reaction was allowed to stir overnight at room temperature. The **Man@Glc-NCs** were dialyzed twice against 1.5 L of MilliQ water.

**2-S-(4-Aminobenzyl)-1,4,7-triazacyclononane-1,4,7-triacetic acid (NOTA) functionalized nanoclusters (NOTA@Glc-NCs)**

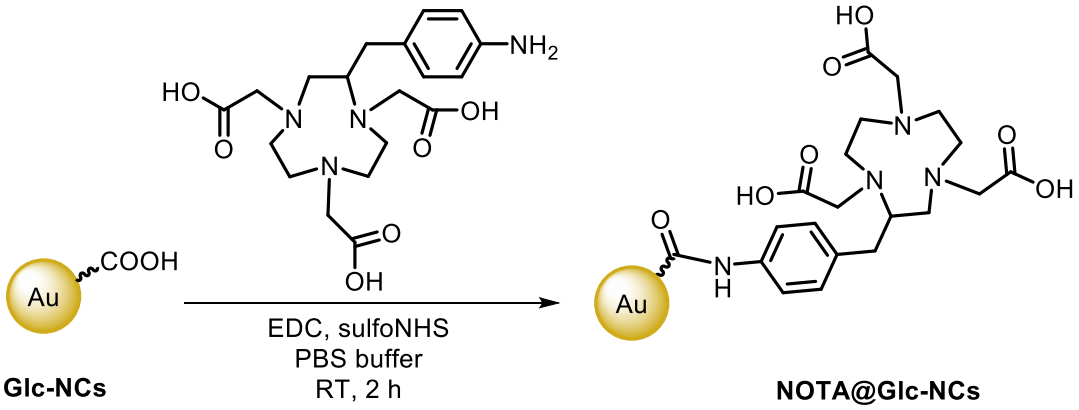


A solution of **Glc-NCs** (1.00 mL, 0.65 µmol Au, 1.26 $10^{15}$ nanoclusters) was diluted with 5 mL MilliQ water and 100 µL PBS. To this solution, EDC (2.50 mg, 0.01 mmol) and sulfo-NHS (2.80 mg, 0.01 mmol) were added dropwise and the reaction was allowed to stir for 5 min under sonication in an ice bath. Subsequently, an aqueous solution of 2-*S*-(4-aminobenzyl)-1,4,7-triazacyclononane-1,4,7-triacetic acid (NOTA) (75.0 µL, 0.4 mmol) was added and allowed to react for 2 h under cold sonication bath. The **NOTA@Glc-NCs** were purified three times against 1.5 L MilliQ water.

**Radiolabeling strategy ($^{64}$Cu(II)-NOTA@Glc-NCs)**

To a solution of **NOTA@Glc-NCs** (20 nmol Au) Cu[$^{64}$Cu]$Cl_2$ (50 MBq) in 2-[N-morpholino]-ethansulfonic acid (MES) buffer (pH 5.0) was added at 37 °C for 3 h. Subsequently, 8-10 fold of EDTA was added.

The **$^{64}$Cu(II)-NOTA@Glc-NCs** were then purified using PD 10 size exclusion column by collecting 200 µL aliquots. The purified **$^{64}$Cu(II)-NOTA@Glc-NCs** were obtained at 3-4 mL which was detected by radio thin layer chromatography. The RCY of **$^{64}$Cu(II)-NOTA@Glc-NCs** was 46%.

## 2.4.2.2. Carbohydrate synthesis

**(2R,3R,4S,5S,6S)-2-(acetoxymethyl)-6-((5-(acetylthio)pentyl)oxy)tetrahydro-2H-pyran-3,4,5-triyl triacetate (2)**

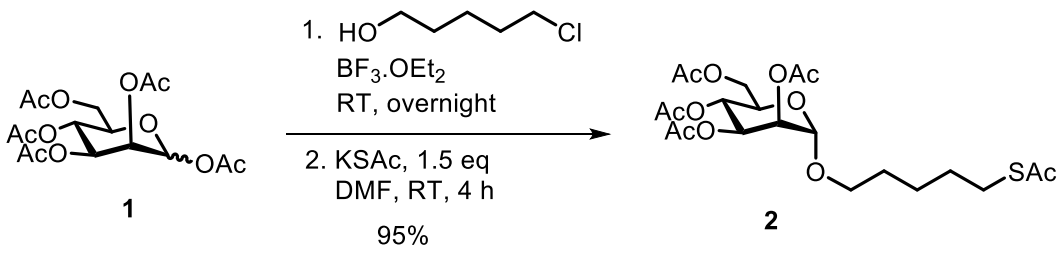


Compound **1** (4.3 g, 11.1 mmol) was dissolved in anhydrous $CH_2Cl_2$ and 5-chloropentan-1-ol (1.5 mL, 13.3 mmol) was added and the reaction stirred for 1 h. The mixture was cooled to 0 °C, $BF_3.OEt_2$ (6.4 mL, 51.2 mmol) was slowly added drop wise and the mixture continuously stirred for additional 12 h at room temperature under Argon atmosphere. The crude mixture was diluted with $CH_2Cl_2$ and water and the phases were separated. The organic layer was washed three times with saturated aqueous $NaHCO_3$ and brine. The organic layers were combined, dried over sodium sulfate, filtered and concentrated in vacuum. The crude compound was taken to the next step without further purification.

The crude compound (0.1 g, 0.2 mmol) was dissolved in anhydrous DMF and stirred with KSAc (0.5 g, 4.4 mmol) overnight at room temperature. The reaction mixture was extracted with EtOAc and concentrated in vacuum to obtain compound **2**. The crude compound was purified using flash column chromatography (EtOAc/Hex 1:4) to obtain the desired compound (0.1 g, 95% yield over two steps).

$^1$H NMR (400 MHz, $CDCl_3$) δ 5.32 (dd, 1H, H-3), 5.27 (d, 1H, H-4), 5.21 (dd, J = 3.3, 1.7 Hz, 1H, H-2), 4.78 (d, J = 1.4 Hz, 1H, H-1), 4.30 – 4.23 (m, 1H, H-6), 4.11 – 4.05 (m, 1H, H-6), 3.98 – 3.92 (m, 1H, H-5), 3.70 – 3.62 (m, 1H, $CH_2$-7), 3.46 – 3.39 (m, 1H, $CH_2$-7), 2.86 (t, J = 7.3 Hz, 2H, $CH_2$-11), 2.31 (s, 3H, $CH_3$-SAc), 2.14 (s, 3H, $CH_3$), 2.09 (s, 3H, $CH_3$), 2.03 (s, 3H, $CH_3$), 1.98 (s, 3H, $CH_3$), 1.63 – 1.54 (m, 4H $CH_2$-8,10), 1.46 – 1.37 (m, 2H, $CH_2$-9), NMR data were in good agreement with those previously reported.[148] LC MS calculated for $[M+K]^+$ 531.2 $C_{21}H_{21}O_{11}S$, found 531.2.

**(2R,3S,4S,5S,6S)-2-(Hydroxymethyl)-6-((5-mercaptopentyl)oxy)tetrahydro-2H-pyran-3,4,5-triol (3)**

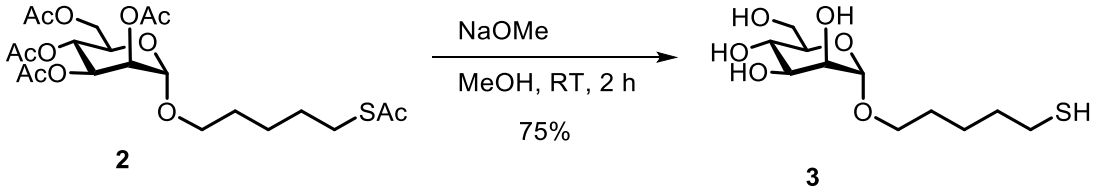


Compound **2** (50 mg, 0.1 mmol) was dissolved in 1 mL of MeOH, then sodium methoxide (5.5 mg, 0.1 mmol) was added and stirred for 2 h at room temperature. The reaction mixture was neutralized with amberlite-IR120 (H+) resin, filtered and concentrated in vacuum to obtain compound **3** (21.5 mg, 75% yield).

$^1$H NMR (400 MHz, $CD_3OD$) δ 4.71 (s, 1H), 3.80 (d, J = 9.8 Hz, 1H), 3.76 (s, 1H), 3.72 (d, J = 9.5 Hz, 1H), 3.70 – 3.66 (m, 1H), 3.65 (d, J = 3.5 Hz, 1H), 3.57 (t, J = 9.4 Hz, 1H), 3.51 (d, J = 8.2 Hz, 1H), 3.44 – 3.37 (m, 1H), 3.33 (s, 2H), 2.68 (t, J = 7.1 Hz, 1H), 2.49 (t, J = 7.1 Hz, 2H), 2.13 (s, 1H), 1.70 (s, 1H), 1.66 – 1.53 (m, 4H), 1.48 (d, J = 7.7 Hz, 2H). NMR data were in good agreement with those previously reported.[149] LC MS calculated for $[M+Na]^+$ 305.1 $C_{11}H_{22}O_6S$, found 305.4

## 2.4.3. Biology methods

### Cell culture

The mouse cell line L929 of adipose cells was cultured in 10 $cm^2$ dishes with RPMI 1640 + 2 mM L-glutamine + 10% fetal bovine serum (FBS) + 0.26 μM cisplatin. The cells were incubated at 37 °C in an ambient air/5% $CO_2$ atmosphere and sub-confluent cultures (70-80%) were split using DPBS + 0.05% EDTA.

**MTS Assay**

For the cell viability assessment, the cells were seeded at 13,000 cells/well in 96-well plates and allowed to settle overnight. Then, the cells were incubated with **Glc-NCs** at 500, 100, 50, 25, 12.5, 6.250, 3.125, 1.563, 0.781, 0.391 and 0 mM from a concentrated stock solution of each of the **Glc-NCs** samples which was prepared in water and successively diluted in RPMI mixture cell media. For the controls, the same amount of water was added to the most concentrated samples and similarly diluted with the cell medium in order to see the effect of water on the viability of the cells.

After 24 h, the CellTiter 96 $A_{Queous}$ One Solution Cell Proliferation Assay was used. For this assay, 20 µL of MTS [3-(4,5-dimethylthiazol-2-yl)-5-(3-carboxymethoxyphenyl)-2-(4-sulfophenyl)-2*H*-tetrazolium inner salt] were directly added to the culture wells and incubated for 1-4 h. The absorbance was then measured at 490 nm using a 96-well plate reader. Untreated cells were assayed as a control reference.

**ICP-AES**

For gold uptake measurements, L929 cells were seeded in 10 $cm^2$ plates. When cells reached confluence in the dish, the cell number was counted (approximately $9 \times 10^7$ cells per plate) and the **Glc-NCs** were added (gold concentrations: 12.5 µM, 25 µM). After 1 h treatment with **Glc-NCs**, the medium was removed and the cells were washed with DPBS + 0.05% EDTA to collect cell residues. The cell residues were further digested with 300 µL of $HNO_3$:HCl (3:1) and decomposed for 48 h at room temperature. Subsequently, 700 µL of MilliQ water was added to each tube. Gold concentrations were determined by Inductively Coupled Plasma Atomic Emission Spectrometer (ICP–AES).

# 3. Targeting protozoan parasites using gold nanoclusters

## 3.1. Introduction

Malaria is a mosquito-borne disease caused by a protozoan parasite that belongs to the *Plasmodium* species. There are five *Plasmodium* species that can infect humans, but *Plasmodium falciparum* (*P. falciparum*) is the most severe one. According to the World Health Organization (WHO), in 2015, 212 millions of malaria infected cases were reported worldwide, causing 429,000 deaths.[155] The typical malaria symptoms are fever, headache and vomit, causing in severe cases seizures, yellow skin, coma or even death.

The *Plasmodium* species, together with *Toxoplasma gondii* (*T. gondii*), belong to the phylum Aplicomplexa having an apicoplast organelle and an apical complex structure that is important in the invasion process.[156] Both *Plasmodium* and *Toxoplasma* species have a complex life cycle that involves different hosts. The life cycle of *Plasmodium* starts with the human host receiving *Plasmodium* sporozoites after the bite of an infected female *Anopheles* mosquito (Figure 3.1). These sporozoites are transmitted to the bloodstream and migrate to the liver within a few minutes where they undergo asexual maturation into liver merozoites during an asymptomatic period of six to 16 days. After this liver stage, the merozoites are released into the bloodstream and invade red blood cells (RBCs) starting the blood life cycle, where the malaria symptoms arise. This invasion of RBCs occurs mainly through an asexual erytrocytic cycle, but some of the merozoites undergo a sexual blood cycle (gametocytogenesis) and develop into male and female gametocytes. These gametocytes are then taken up by an *Anopheles* mosquito during a blood meal into the gut and develop into macrogametes (female) and microgametes (male). These gametes undergo fertilization resulting in a zygote formation that develops into an ookinete that migrates through the gut wall forming a polyploid oocyst. After maturation, this oocyst releases new

sporozoites that migrate to the salivary gland of the mosquito and are further transmitted to another human host through a mosquito bite, starting the cycle again.

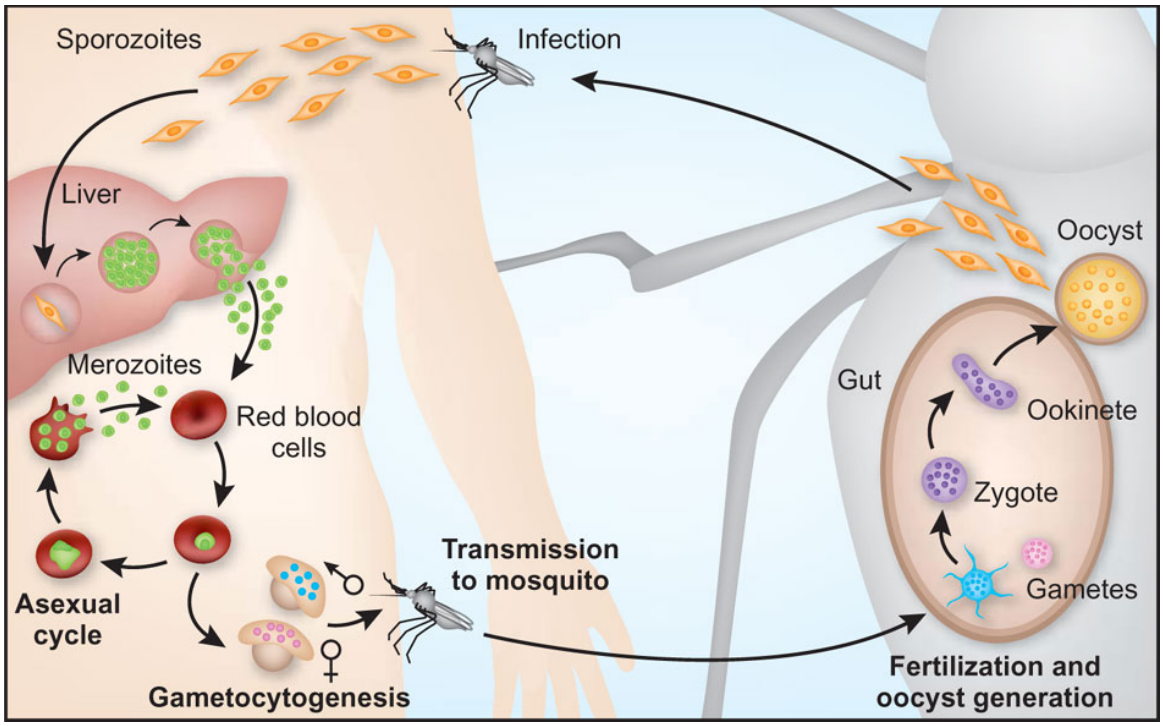


**Figure 3.1.** Life cycle of *Plasmodium* species. *Plasmodium* sporozoites are transmitted by a female *Anopheles* mosquito to the human host. These sporozoites migrate into the liver and develop into merozoites that are released to the bloodstream. Merozoites invade RBCs mainly through asexual reproduction releasing more merozoites, but also producing gametocytes that are taken up again by another *Anopheles* mosquito inside of which the life cycle is completed. Reprinted from Pasvol *et al.*[157] Copyright (2016), with permission from Springer Nature.

The malaria symptoms appear during the blood life cycle of *P. falciparum*. This erythrocytic cycle starts when the merozoites are released from the liver into the bloodstream. The merozoites invade RBCs and undergo different stages as they start to reproduce asexually (Figure 3.2). The earliest stage inside the RBCs is called ring stage as the parasite adopts a ring shape. These rings further develop into early and late stage trophozoites that are visible under the optical light microscope due to an increase in size as well as by the beginning of polyploidy. Finally, the last polyploid stage of the blood life cycle is the schizont stage that, after 48 h of invasion, is capable to burst the RBC and release 16 to 32 merozoites, capable to invade other RBCs.[158] The whole process of merozoites release, and further recognition, attachment and invading RBCs occurs very rapidly (less than a minute).[156]

During the blood life cycle, some of the parasites undergo gametocytogenesis, where they develop into gametocytes. This process increases under certain conditions such as high host parasitemia (quantitative content of parasites in the blood), or even drug treatment, as it creates an environmental stressor.[159-160] In *P. falciparum*, the gametocytogenesis usually occurs within ten to twelve days and is divided into five stages (stages I to V). Gametocytes stage I are very similar to asexual trophozoites, but in stage II, the gametocytes start to elongate forming a D-shaped parasite (Figure 3.2). In stage III the gametocytes get longer reaching, in stage IV, a very elongated banana-like shape. Finally, in stage V of gametocytogenesis, both male and female gametocytes can be distinguished as the female gametocytes are more curved than the male ones.[159]

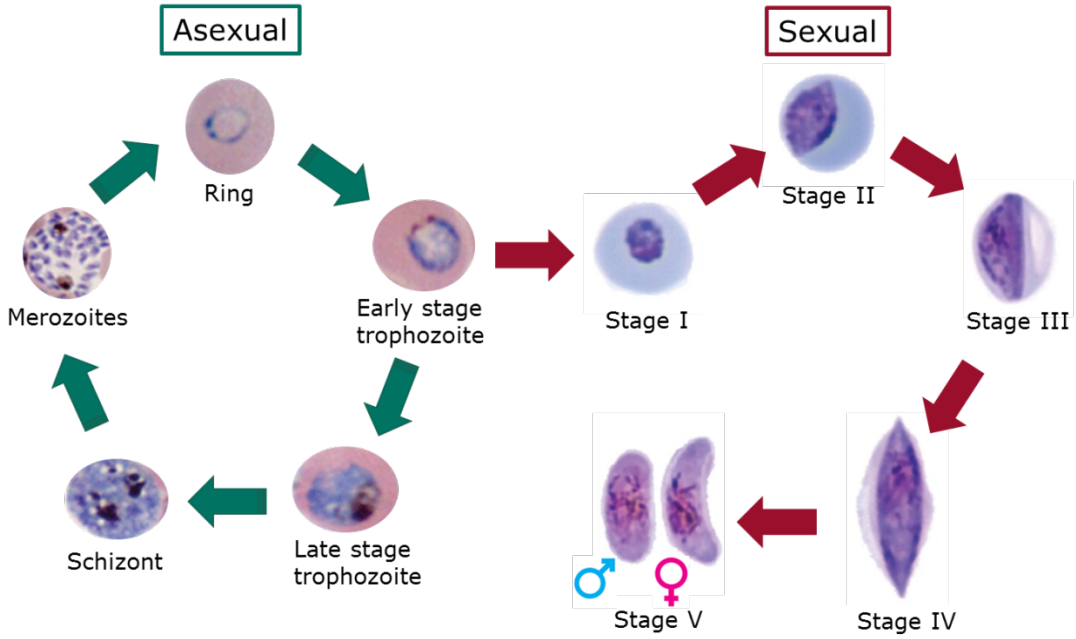


**Figure 3.2.** Blood cycle of *Plasmodium falciparum*. The asexual cycle starts with RBCs invasion of merozoites and development of the parasites into different stages: rings, trophozoites, schizonts and finally merozoites that are released to the bloodstream to invade more RBCs. Some parasites undergo gametocytogenesis as they commit sexual development. The parasites undergoing different stages (I, II, III and IV) until they finally develop into stage V as male and female gametocytes. These gametocytes are further taken up by an *Anopheles* mosquito and are responsible for the transmission of the disease.

Several methods to prevent and treat malaria exist, but are of limited efficacy. Prevention methods of malaria comprise the use of insecticide treated nets, indoor residual spraying or even larva source management in order to eliminate malaria vectors. Nevertheless, the increasing resistance to insecticides requires the need of alternative methods to control malaria vectors.[161] Regarding malaria treatments, the most effective medication is the

artemisinin-based combinational therapy (ACT) that uses the drug artemisinin together with other anti-malaria drugs. Artemisinin is extracted from sweet wormwood (*Artemisia annua*) that is cultivated in many countries of Asia and Africa. Nevertheless, the cultivation and production costs of artemisinin are relatively high, demanding the need of alternatives, such as chemical synthesis.[162] Recently, a semi-synthetic approach was developed to produce artemisinin using a continuous-flow system.[163] The starting material, artemisinic acid can be extracted from the same plant in higher yields allowing for a cost-effective large scale production. However, due to the low number of existing alternatives, the demand of novel efficient anti-malaria drugs is still high. Furthermore, the side effects of artemisinin (nausea, vomiting and dizziness) and other anti-malaria drugs, together with rising drug resistance due to high administrations suggest the need of other therapeutic strategies, such as targeted drug delivery.

For targeted therapies, it is important to understand the surface biochemistry of the parasites during the blood cycle. It is known that the surface of merozoites is coated with glycosylphosphatidylinositol (GPI)-anchored proteins that are likely to play an important role during erythrocyte invasion.[164] Many of these GPI-anchored surface proteins contain cysteine-rich domains, such as the reticulocyte binding homolog 5 (PfRh5), or the cysteine-rich protective antigen (CyRPA).[165-166] These cysteine-rich domains are known to also be expressed on the surface of other stages of *P. falciparum* such as schizonts, gametocytes and sporozoites.[164, 167-168] Similarly, the asexual *T. gondii* stage tachyzoite has also surface proteins containing cysteine-rich domains, such as the surface antigen (SAG) related sequence (SRS) superfamily.[156] Therefore, the design of a scaffold able to target cysteine could potentially give information regarding the proteins on each stage of *P. falciparum* and *T. gondii*. Moreover, the use of multivalent scaffolds such as nanoparticles, allows for the design of a multimodal system that can carry one or more biologically active functional groups.

Thiols have been widely used to functionalize gold nanoparticles as the resulting bond is strong and useful for many applications such as sensing and drug delivery.[169] In particular, cysteine has been used to functionalize gold nanoparticles.[170-173] Nevertheless, there is no report about the use of gold nanoparticles to target cysteine moieties expressed on biological systems.

In this chapter, glucose-synthesized gold nanoclusters (**Glc-NCs**, Chapter 2) were used for targeting studies using *Plasmodium falciparum* and *Toxoplasma gondii*. For this purpose, **Glc-NCs** were used without further functionalization and conjugated with a dye to have a better insight into the binding efficiencies to the different stages of the protozoan parasites. **Glc-NCs** were further functionalized with pyrimethamine, a drug used to treat both malaria and toxoplasmosis, to further determine the effectiveness of this system as a nanocarrier.[174-175]

# 3.2. Results

## 3.2.1. Targeting *Plasmodium falciparum*

As described in Chapter 2, **Glc-NCs** showed high potential for biomedical applications. To assess the suitability of **Glc-NCs** to target *Plasmodium falciparum* different biological experiments were carried out using *in vitro P. falciparum* cultures.

Mature stages in the erythrocytic cycle of *P. falciparum* contain cysteine-rich domains on the parasite surface. As cysteine is widely used to functionalize gold nanoparticles (AuNPs), to get a first insight into the possibility of using gold nanomaterials for targeting cysteine-rich domains, extracellular schizonts were treated with 2 nm **Glc-NCs**[c] and citrate stabilized AuNPs (**Cit-AuNPs**) of 20 nm (Figure 3.3). **Cit-AuNPs** were synthesized using the previously reported Turkevich method.[135]

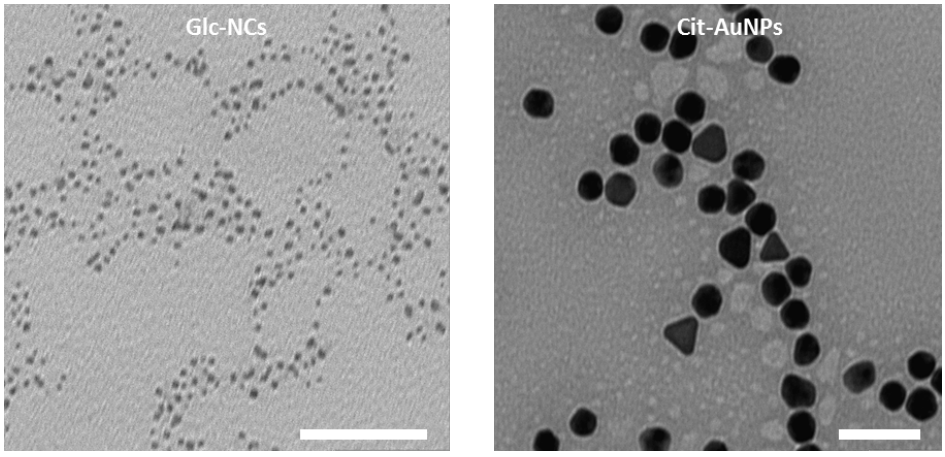


[c] Synthesis of **Glc-NCs** was performed as described in Chapter 2.

**Figure 3.3.** Transmission electron microscopy images of **Glc-NCs** (left) and **Cit-AuNPs** (right). Scale bar = 50 nm.

Inductively Coupled Plasma Atomic Emission Spectrometry (ICP-AES) was used to detect the concentration of gold bound to the parasites. Schizonts were isolated from RBCs by incubating a culture with high parasitemia at schizont stage with saponin to lyse RBCs. Three different concentrations of **Glc-NCs** and **Cit-AuNPs** in PBS (5, 20 and 50 μM, based on atomic gold) were incubated with the isolated parasites for 15 min at room temperature. After incubation, the parasites were washed three times with PBS to remove unbound nanoparticles and incubated for 24 h with aqua regia, to oxidize Au(0) to Au(III) that was detected by ICP-AES. The binding efficiency of **Glc-NCs** was significantly higher at the three concentrations compared to the binding of **Cit-AuNPs** (Figure 3.4). This proves that gold nanoparticles adhere to mature parasites, possibly *via* cysteine-rich domains. Moreover, the higher binding of **Glc-NCs** compared to **Cit-AuNPs** can be explained due to size, as the smaller the nanoparticles, the higher the surface area. This provides a higher surface contact with the parasites allowing for more **Glc-NCs** to bind, which results in a higher binding efficiency. This result shows the high potential of using gold as targeting nanovector of *P. falciparum*, especially in the ultrasmall range, as the high surface to volume ratio also affords more surface area for bioconjugations.

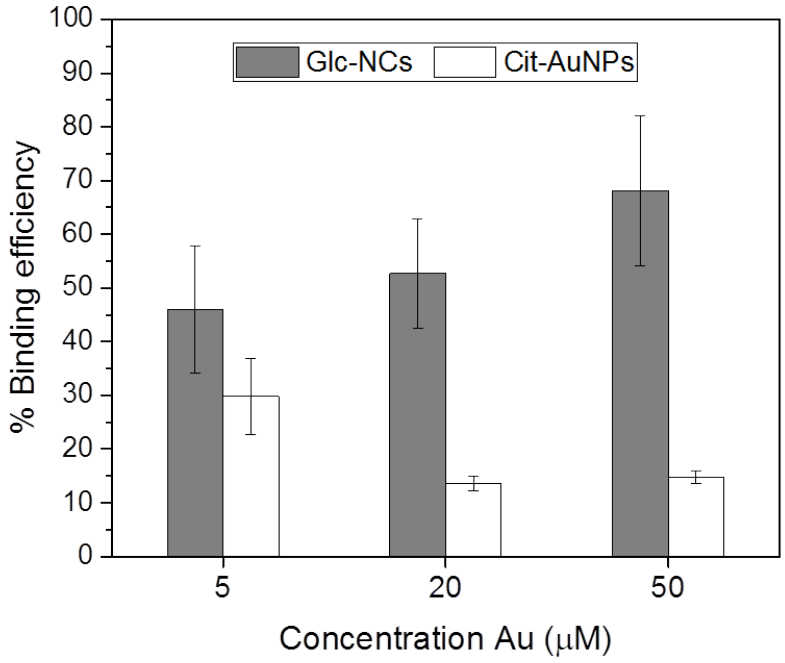


**Figure 3.4.** Binding efficiency of **Glc-NCs** (2 nm) and **Cit-AuNPs** (20 nm) in three different concentrations based on atomic gold (5, 20 and 50 μM) to extracellular schizonts.

The high binding efficiency of **Glc-NCs** to isolated mature parasites can be exploited to target parasites present inside RBCs. **Glc-NCs** are not cytotoxic in mouse fibroblast cells and biodistribute well *in vivo* (Chapter 2). Nevertheless, **Glc-NCs** should show as well minimum hemolytic effect for further *in vitro* experiments. For this purpose, a hemolysis assay was performed using different concentrations of **Glc-NCs** (ranging from 2.5 nM to 50 μM, based on atomic gold) with human RBCs invaded by parasites at different stages (i.e. rings, trophozoites and schizonts), as well as healthy RBCs were taken as control.

The three different blood stages of *P. falciparum* were isolating by performing either sorbitol synchronization to isolate ring stages or percoll synchronization or using magnetic columns to isolate schizont stages. Sorbitol synchronization takes advantage of the osmotic fragility of malaria-infected RBCs and is able to selectively lyse erythrocytes containing mature parasites.[176] Schizont stages can be magnetically separated because during the blood life cycle, the parasites degrade the hemoglobin of the RBCs as a main source of amino acids which results in an accumulation of haem in the cells.[177] This free haem is metabolized and converted into malaria pigment haemozoin, which forms paramagnetic iron crystals that are accumulated in the vacuole of mature parasites. Since the haem moiety in the hemoglobin is diamagnetic, the iRBCs containing only mature parasites can be separated using magnetic-activated cell sorting (MACS) and LD columns.

To understand whether the parasitemia affects the hemolysis of RBCs incubated with **Glc-NCs**, the experiment was performed using 1% and 10% parasitemia of highly synchronized cultures. For this experiment, infected and healthy RBCs were incubated with **Glc-NC**s at different concentrations for 15 min. Subsequently, the samples were centrifuged and the supernatant was separated and measured at 540 nm to obtain the amount of lysed RBCs. Hemolysis was calculated by considering 100% of lysis RBCs treated with saponin, and 0% of lysis RBCs incubated with PBS. **Glc-NCs** did not produce significant hemolysis, as the hemolysis was always below 1% (Figure 3.5), and are therefore suitable for further *in vitro* experiments.

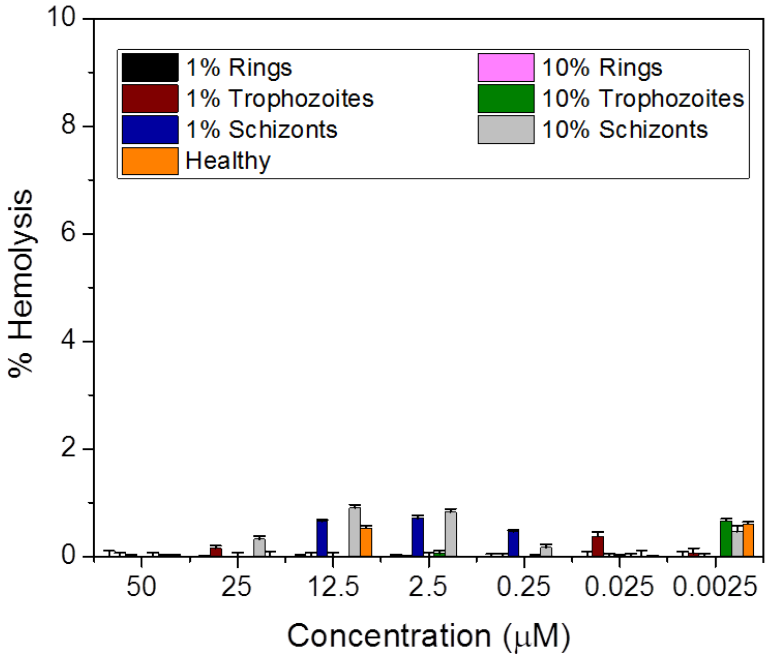


**Figure 3.5.** Hemolysis assay performed by incubating different concentrations of **Glc-NCs** (2.5 nM – 50 μM) with 1% and 10% parasitemia of highly synchronized cultures (rings, trophozoites and schizonts) and healthy RBCs.

To further assess the binding capabilities to different *P. falciparum* blood stages, **Glc-NCs** were conjugated with a fluorescent dye containing a free primary amine (ATTO647N) to yield **ATTO@Glc-NCs** (Scheme 3.1).[d]

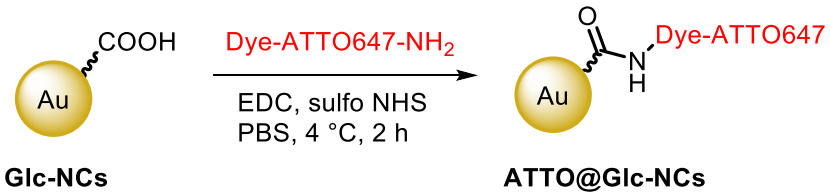


**Scheme 3.1.** Conjugation of the fluorescent dye ATTO647N to **Glc-NCs** to yield **ATTO@Glc-NCs**.

After dialysis purification for 2 days, transmission electron microscopy (TEM) of **ATTO@Glc-NCs** showed same particle size and shape as naked **Glc-NCs** (Figure 3.6 c). UV spectra showed an absorbance band at around 640 nm in **ATTO@Glc-NCs**, confirming the presence of the dye on the surface of the nanoclusters (Figure 3.6 a, b).

[d] Optimized conditions used for the coupling reaction are described in Chapter 2.

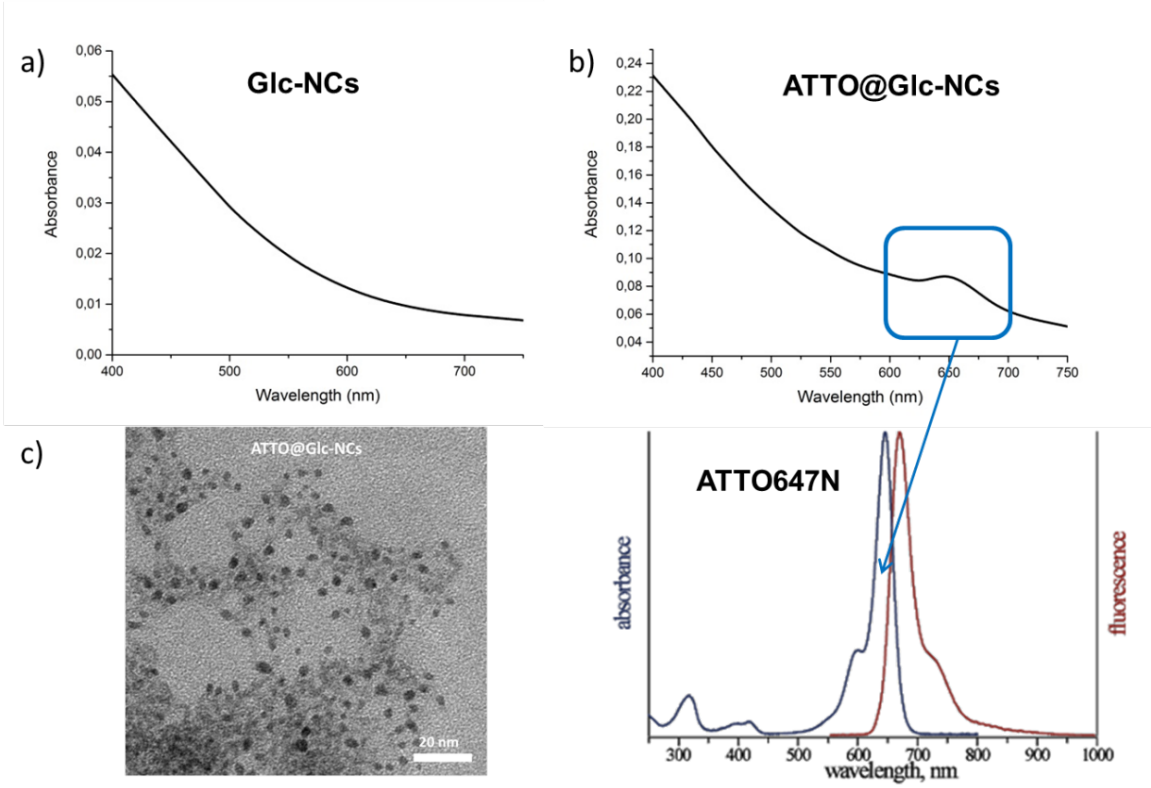


**Figure 3.6.** a) UV spectrum of naked **Glc-NCs**; b) UV spectrum (above) of **ATTO@Glc-NCs** that shows a band at 640 nm that corresponds to the absorption band of ATTO647 dye (below); c) TEM of **ATTO@Glc-NCs**. Scale bar = 20 nm.

To test whether **ATTO@Glc-NCs** were able to specifically bind parasites, nanoclusters (20 µM) were incubated for 15 min with both infected and healthy RBCs. Subsequently, the unbound **ATTO@Glc-NCs** were washed out with PBS buffer and the parasites were stained with the DNA binding dye 4',6-diamidino-2-phenylindole (DAPI, in blue), as RBCs do not contain DNA, unless they are invaded by *P. falciparum* parasites. Confocal laser scanning microscopy (CLSM) showed that **ATTO@Glc-NCs** (in red) were specifically binding *P. falciparum* parasites (in blue) and not RBCs (Figure 3.7). RBCs were identified by the differential interference contrast (DIC) channel.

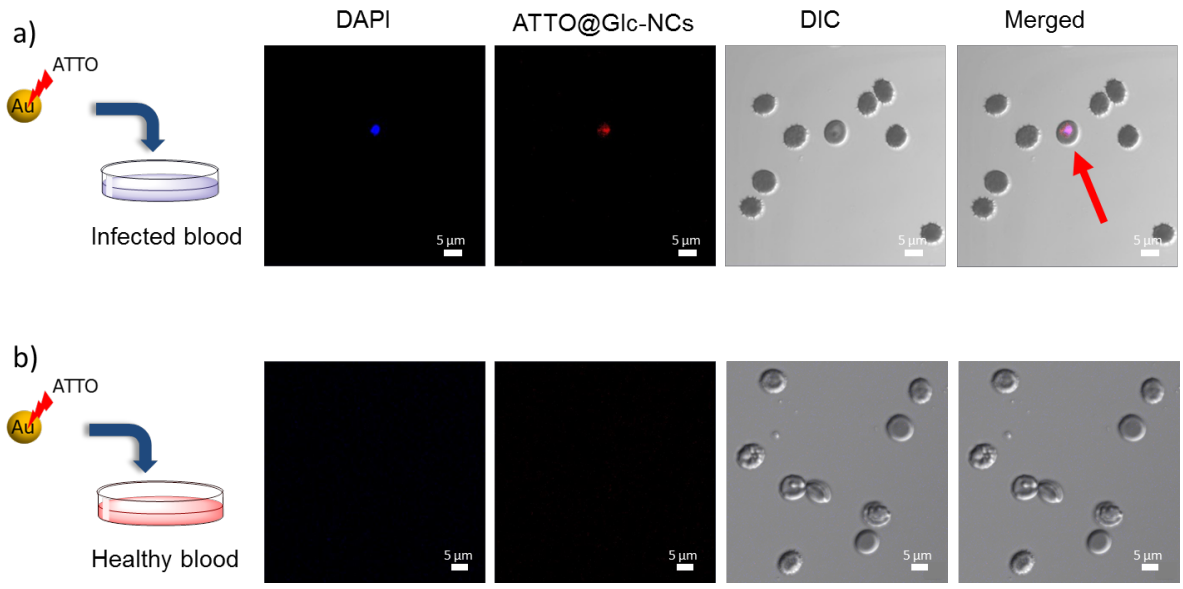


**Figure 3.7.** Confocal laser scanning microscopy of **ATTO@Glc-NCs** (red) at 20 µM incubated with a) *P. falciparum* infected RBCs, and b) healthy RBCs (blue = DAPI). Scale bar = 5 µm.

In order to verify that the nanoclusters are binding due to the gold core and not through the dye, another control experiment was carried out using the corresponding concentration of non-conjugated ATTO647N dye conjugated on **ATTO@Glc-NCs**. Both healthy and infected RBCs were incubated for 15 min with the ATTO647N dye and further washed with PBS buffer to remove unbound material. Parasites were further stained with DAPI and measured with CLSM. Results showed that the free ATTO647N dye (in red) did not bind the parasites or the healthy RBCs (Figure 3.8).

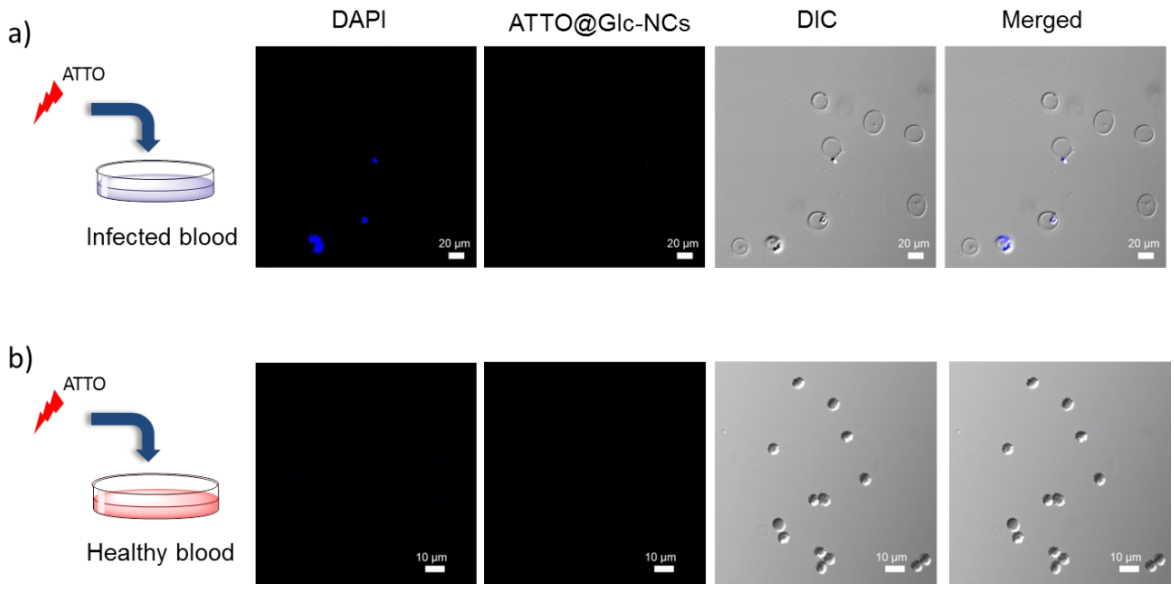


**Figure 3.8.** Confocal laser scanning microscopy of free ATTO647N (red) incubated with a) *P. falciparum* infected RBCs (scale bar = 20 µm), and b) healthy RBCs (blue = DAPI). Scale bar = 10 µm.

To further prove that the binding of **ATTO@Glc-NCs** occurs through the gold core and not due to the dye, the fluorescent dye cyanine 5 (Cy5) containing a free amine was used to tag **Glc-NCs** using the same conditions to yield **Cy5@Glc-NCs** (Scheme 3.2)

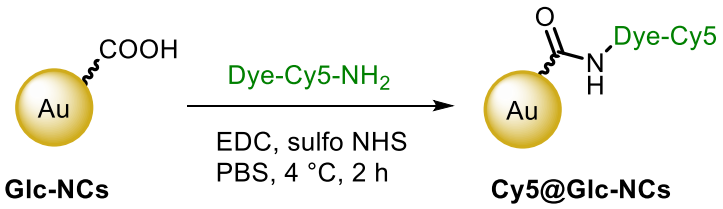


**Scheme 3.2.** Conjugation of the fluorescent dye Cy5 to **Glc-NCs** to yield **Cy5@Glc-NCs**.

After further dialysis purification, transmission electron microscopy (TEM) of **Cy5@Glc-NCs** showed same particle size and shape as naked **Glc-NCs** as well as **ATTO@Glc-NCs** (Figure 3.9 c). UV spectra showed an absorbance band at around 640 nm in **Cy5@Glc-NCs** that confirmed the presence of the dye on the surface of the nanoclusters (Figure 3.9 a, b).

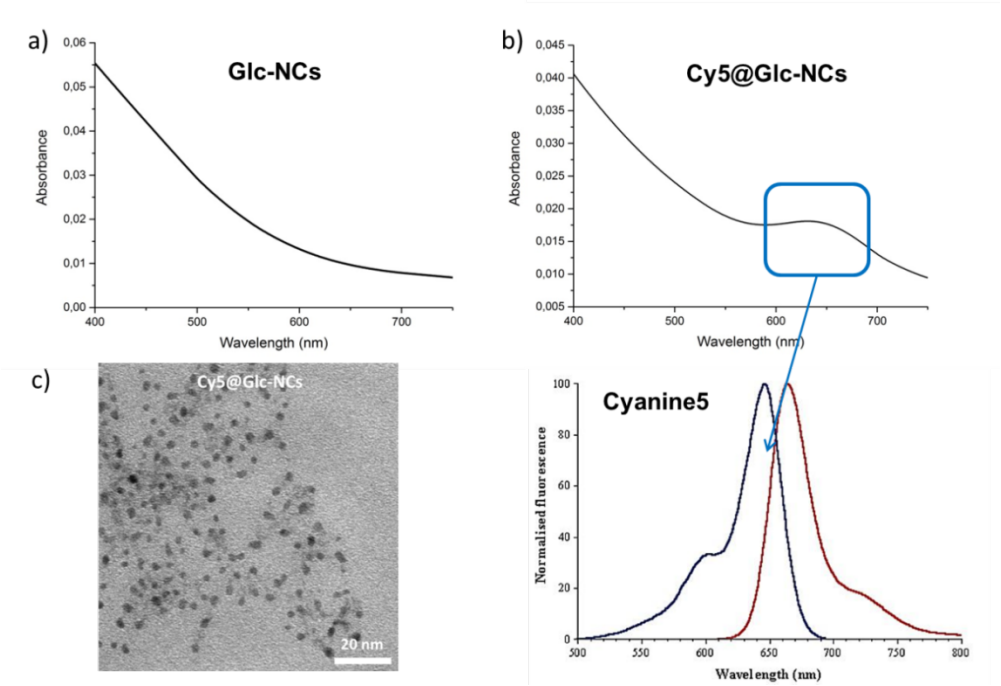


**Figure 3.9.** a) UV spectrum of naked **Glc-NCs**; b) UV spectrum (above) of **Cy5@Glc-NCs** that shows a band at 640 nm that corresponds to the absorption band of Cy5 dye (below); c) TEM of **Cy5@Glc-NCs**. Scale bar = 20 nm.

Similarly as described for **ATTO@Glc-NCs**, to analyze whether **Cy5@Glc-NCs** were able to specifically bind parasites, 20 µM of the tagged nanoclusters were incubated for 15 min with both infected and healthy RBCs. The unbound **Cy5@Glc-NCs** were washed out with PBS buffer and the parasites were stained with DAPI (in blue). CLSM showed specific binding of **Cy5@Glc-NCs** to the parasites and no the RBCs.

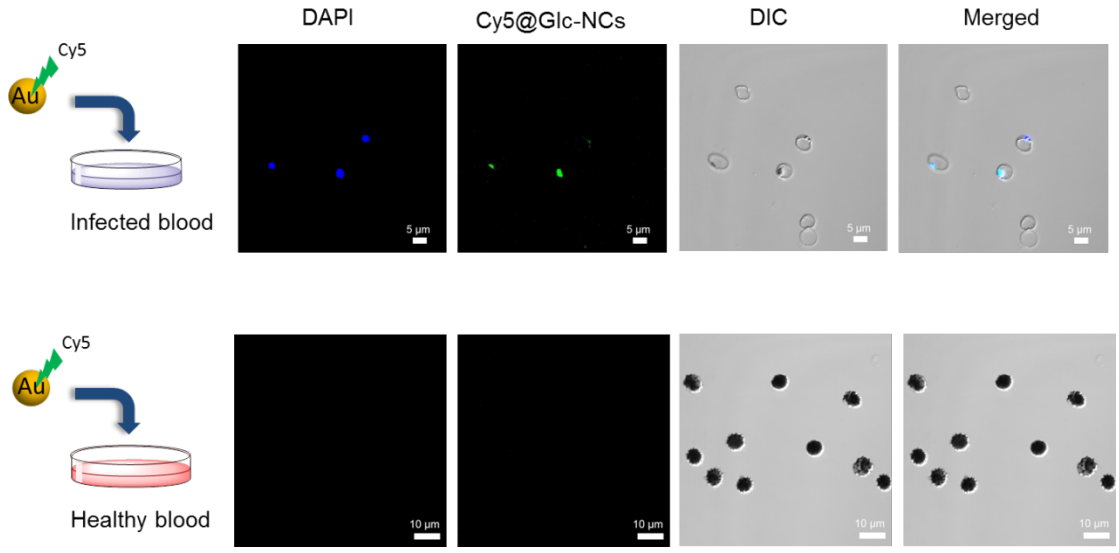


**Figure 3.10.** Confocal laser scanning microscopy of **Cy5@Glc-NCs** (green) at 20 µM incubated with a) *P. falciparum* infected RBCs (scale bar = 5 µm), and b) healthy RBCs (blue = DAPI). Scale bar = 10 µm.

Similarly to the ATTO647N dye experiments, a control experiment was carried out incubating the corresponding concentration of Cy5 dye conjugated to **Cy5@Glc-NCs** using the sample conditions as previously described. CLSM imaging showed that the free Cy5 dye has unspecific affinity to *P. falciparum* parasites as well as some healthy RBCs (Figure 3.11). Therefore, for further experiments, ATTO647N dye was used to tag **Glc-NCs**.

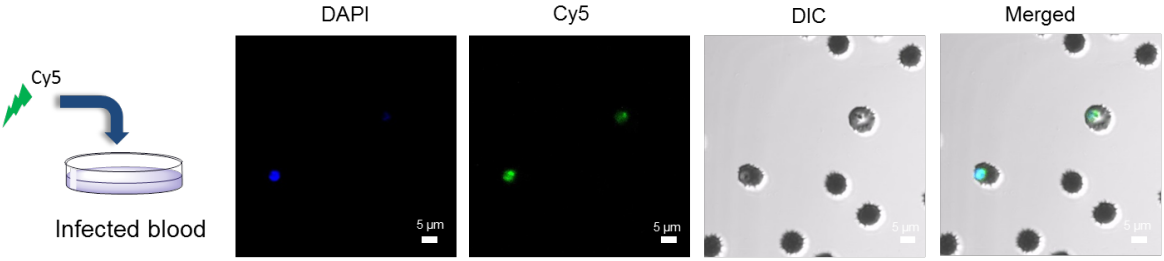


**Figure 3.11.** Confocal laser scanning microscopy of free Cy5 (green) incubated with *P. falciparum* infected RBCs (blue = DAPI). Scale bar = 5 µm.

To analyze the specificity of **Glc-NCs** to target the different blood stages of *P. falciparum*, the infected cultures underwent different types of synchronization cycles to isolate the specific stages. Ring stages were obtained by performing the sorbitol synchronization. Schizonts were isolated by doing either percoll synchronization or magnetic cell separation using columns and a magnetic-activated cell sorting (MACS). Trophozoites (both early and late stages) were imaged 22 to 36 h after performing sorbitol synchronization. Each of the synchronized cultures was incubated with 20 µM **ATTO@Glc-NCs** for 15 min. Healthy cells were also treated as control. After washing with PBS to remove unbound **ATTO@Glc-NCs**, CLSM was used to image the specific binding to all the different asexual blood stages. Results showed that **ATTO@Glc-NCs** were able to specifically bind all the asexual blood stages: rings, early and late trophozoites and schizonts (Figure 3.12). This binding specificity to all the asexual blood stages can be important for drug delivery, as many drugs are stage specific, and cargo delivery will be ensured.

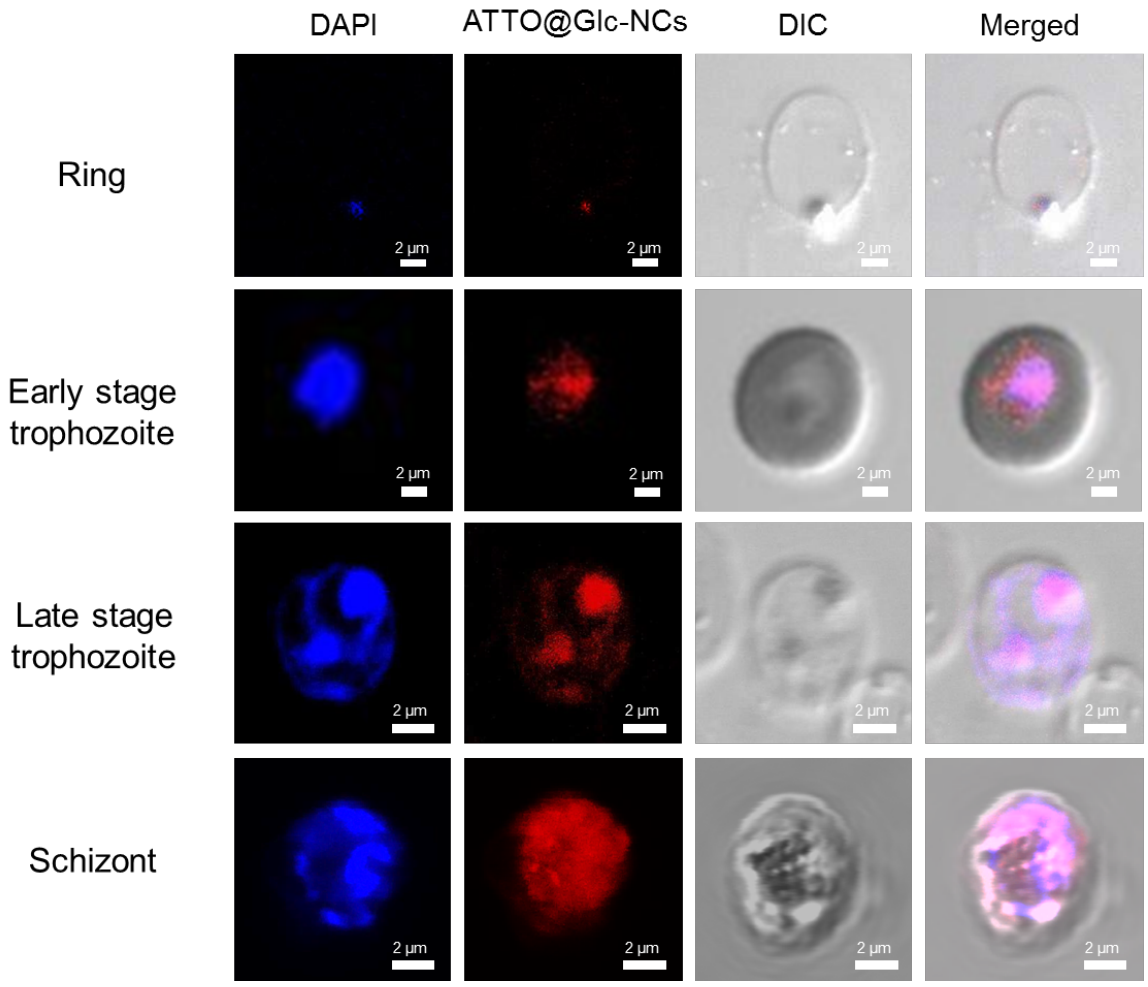


**Figure 3.12.** Confocal laser scanning microscopy of synchronized cultures containing rings, early and late trophozoites, and schizonts incubated with **ATTO@Glc-NCs** (red), show specific binding to each asexual blood stage (blue = DAPI). Scale bar = 2 µm.

Cysteine-rich domains are known to be present on the parasite surface of schizonts.[164] In order to analyze the location of **ATTO@Glc-NCs** on mature parasites, Z-Stack confocal imaging was performed on schizonts incubated with **ATTO@Glc-NCs** using the same conditions as previously described. Results showed that **ATTO@Glc-NCs** are covering the surface of the mature parasites, but are also present inside the parasite, as also DAPI (in blue) was co-localized with the tagged nanoclusters (in red) (Figure 3.13). This proves that **ATTO@Glc-NCs** not only interact with the surface through the cysteine rich domains, but are also able to penetrate the parasite and accumulate inside of it.

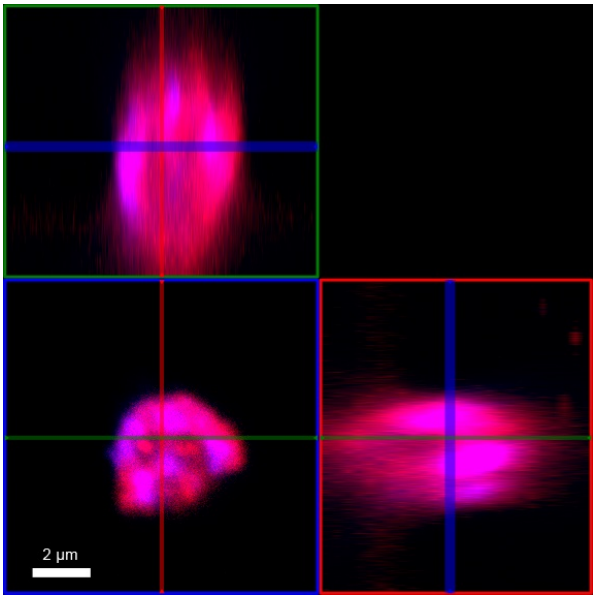


**Figure 3.13.** Z-stack confocal imaging of a schizont incubated with **ATTO@Glc-NCs** (red) (blue = DAPI). Scale bar = 2 µm.

The transmission of the malaria disease occurs through the sexual blood stages. Gametocytogenesis can be also induced in an *in vitro* culture under very specific conditions that involve high levels of parasitemia, low hematocrit to simulate anemia, and the presence of human serum and *N*-acetyl-glucosamine in the parasite culture medium.[178] Isolation of all the different stages of the sexual blood cycle (stages I to V) was achieved either by percoll synchronization or magnetic cell separation using LD columns to separate the late stages from the early ones. **ATTO@Glc-NCs** were once again incubated for 15 min. After washing with PBS, CLSM was used to monitor the binding of **ATTO@Glc-NCs** to the different sexual stages. **ATTO@Glc-NCs** bind all the stages from I to IV and even the isolated male and female gametocytes (stage V), which is essential for delivery of drugs against gametocyte stages that prevents the transmission of the malaria disease through the uptake by the mosquito (Figure 3.14).

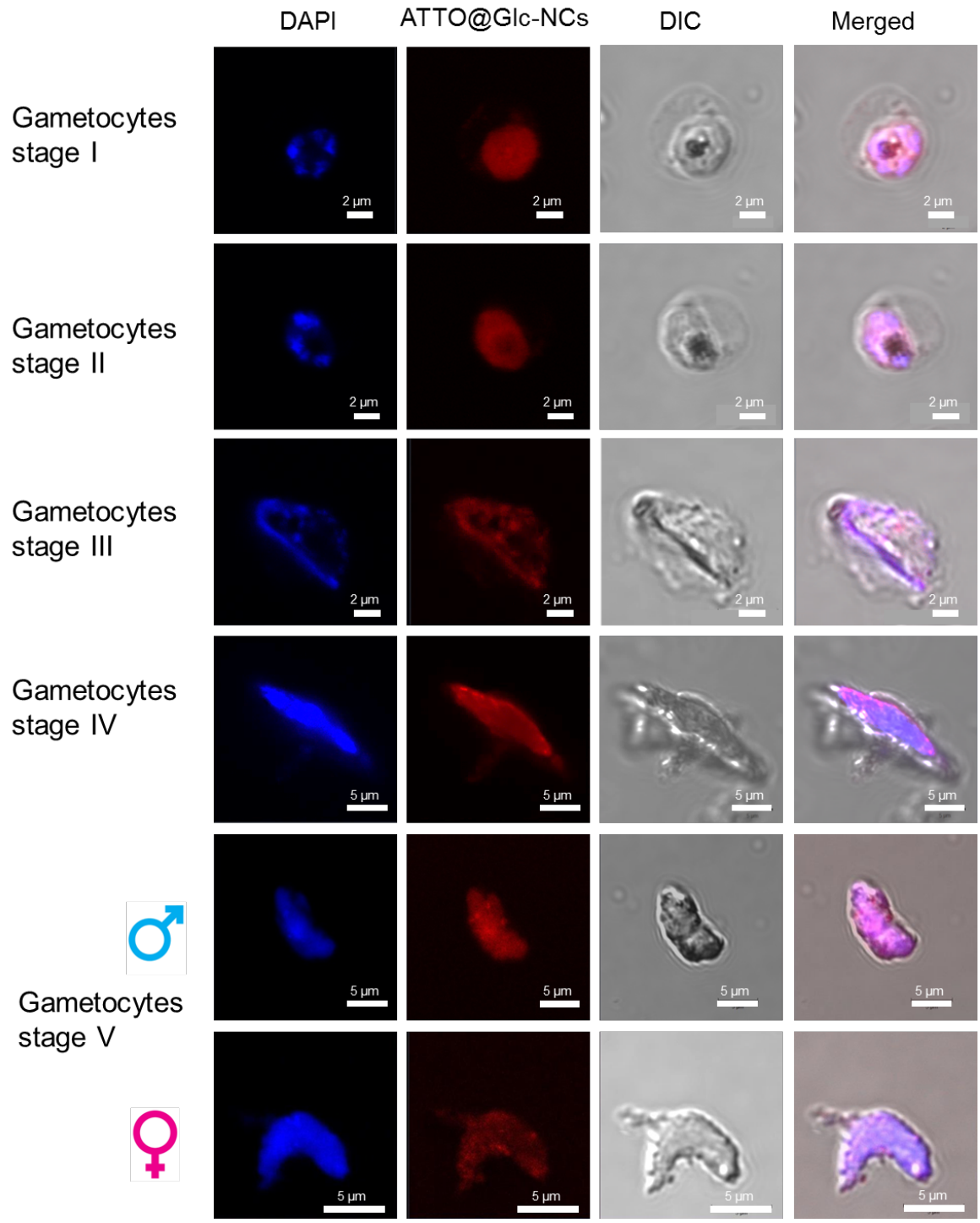


**Figure 3.14.** Confocal laser scanning microscopy of synchronized cultures containing gametocytes stages I, II, III, IV and V incubated with **ATTO@Glc-NCs** (red), show specific binding to each sexual blood stage (blue = DAPI). Scale bar = 2 µm for stages I-III. Scale bar = 5 µm for stages IV and V.

Gametocytes in stage IV were also analyzed by Z-stack imaging in confocal microscopy after incubation with **ATTO@Glc-NCs**. Results show that **ATTO@Glc-NCs** interact with the surface of the parasite, but are also present inside the parasite, as the signal of the

tagged nanoclusters (in red) co-localizes with the signal of the nuclei of the parasites (in blue) (Figure 3.15).

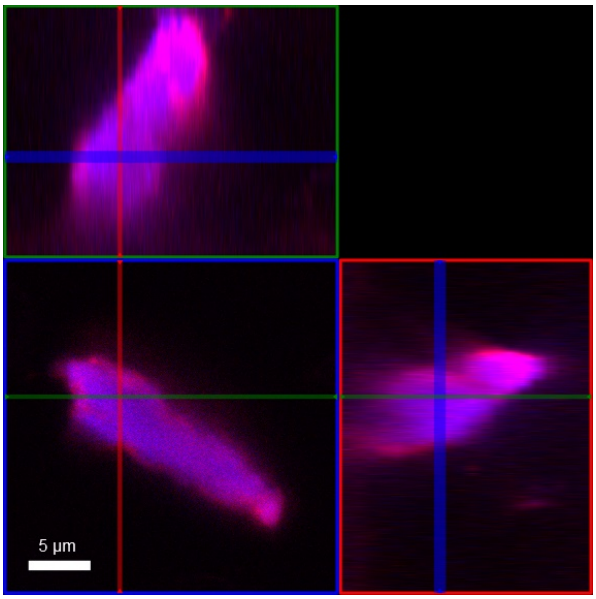


**Figure 3.15.** Z-stack confocal imaging of a gametocyte stage IV incubated with **ATTO@Glc-NCs** (red) (blue = DAPI). Scale bar = 5 µm

The ability of **Glc-NCs** to specifically target all the blood stages of *P. falciparum* opens up opportunities for targeted drug delivery applications. Conjugation of drugs on **Glc-NCs** was done for further delivery studies.

## 3.2.2. Targeting *Toxoplasma gondii*

Similarly to *P. falciparum*, the protozoan parasite *T. gondii* also contain cysteine rich domains on surface proteins.[156] Thus, **ATTO@Glc-NCs** were used to target *T. gondii*.[e]

Extracellular parasites were used to assess the binding of **ATTO@Glc-NCs** with CLSM. For this experiment, the tagged nanoclusters were incubated for 15 min with extracellular *T. gondii* in the tachyzoite stage, and further washed with PBS to remove unbound nanoclusters. CLSM imaging showed that the cysteine rich domains on the parasite surface could probably be targeted by **ATTO@Glc-NCs** (Figure 3.16). The parasites could be identified from the DIC and the DAPI (in blue) channel.

[e] *Toxoplasma gondii* parasites (extracellular and intracellular) were provided by Ms. Laura Radtke, Humboldt University, Department of Biology, Molecular Parasitology.

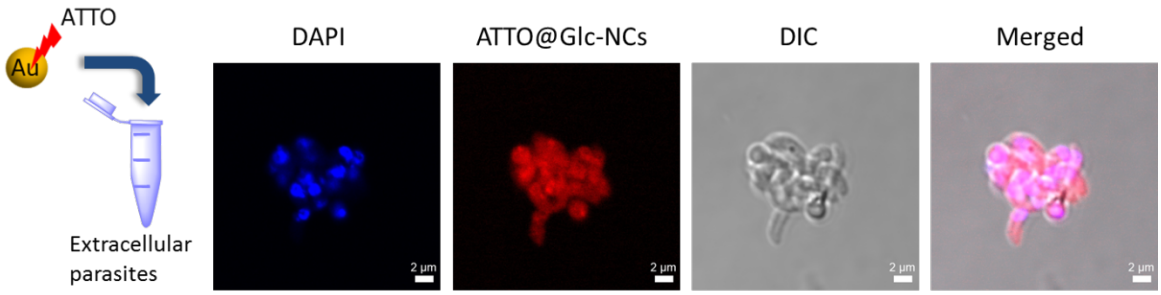


**Figure 3.16.** Confocal laser scanning microscopy of **ATTO@Glc-NCs** (red) incubated with extracellular *T. gondii* (blue = DAPI). Scale bar = 2 µm.

CLSM Z-stack imaging was performed to obtain more information about the location of **ATTO@Glc-NCs** on the parasites. The nanoclusters were found on the surface of the extracellular parasites, but were also located inside, as the nuclei (in blue) co-localized with the signal of the **ATTO@Glc-NCs** (in red) (Figure 3.17).

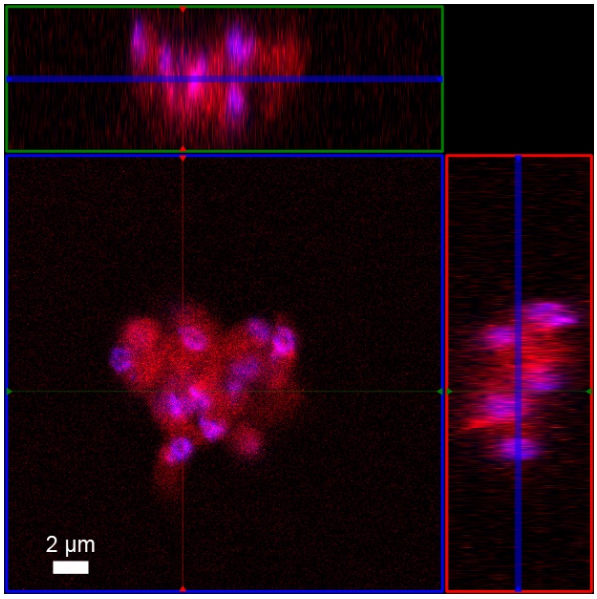


**Figure 3.17.** Z-stack confocal imaging of extracellular *T. gondii* parasites incubated with **ATTO@Glc-NCs** (red) (blue = DAPI). Scale bar = 2 µm.

Human foreskin fibroblast (HFF) cells were infected with *T. gondii* to assess whether **ATTO@Glc-NCs** were able to penetrate the cells and target the parasites. The infected cells were grown in glass slides and the previously described conditions (Section 3.2.1.) were used for the binding assay of **ATTO@Glc-NCs**. DAPI (in blue) was used to stain the nuclei of both host cells and parasites, SAG1 (in green) is a tagged antibody that specifically binds SAG surface proteins, and was used to identify the intracellular parasites. CLSM

analysis was carried out to analyze the binding of the nanoclusters in a much more complex environment. Confocal imaging showed that HFF host cells were infected with cysts containing bradyzoites. These parasites could be directly identified through the SAG1 channel (in green) as well as the DAPI channel (in blue).[f] The nuclei of the host cells were much bigger in size compared to the nuclei of the parasites. Results showed that **ATTO@Glc-NCs** were dispersed within the host cell and were also attached to the bradyzoites (Figure 3.18). The attractiveness of targeting bradyzoites lies in the formation of cysts that accumulate in many organs such as lungs, liver, kidneys and are also able to reach the brain.[179] Interestingly, it is possible to visualize the cyst that contains the bradyzoites, as it is formed by a vacuole, where the **ATTO@Glc-NCs** are not attached to. This means that **ATTO@Glc-NCs** are able to penetrate the vacuole, but do not bind to it. The presence of **ATTO@Glc-NCs** overall within the cells can be explained by the host cellular uptake that retains the nanoclusters for a long time before they are exocytosed.

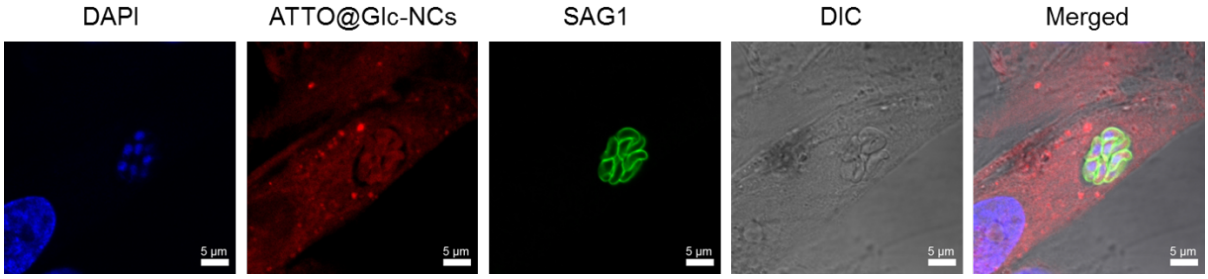


**Figure 3.18.** Confocal laser scanning microscopy of **ATTO@Glc-NCs** (red) incubated with *T. gondii* infected HFF cells (blue = DAPI, green = SAG1). Scale bar = 5 µm.

To gain a better understanding of the exact location of the **ATTO@Glc-NCs** within the infected HFF cells, Z-stack confocal analysis was performed. **ATTO@Glc-NCs** are localized on the surface and inside the bradyzoites, which can be confirmed as the SAG1 antibody stains only the surface of the parasite (Figure 3.19). It is also possible to confirm that the vacuole containing the bradyzoites does not have affinity to **ATTO@Glc-NCs**, as there is a gap line between the bradyzoites and the rest of the cytoplasm.

[f] Microscopy slides preparation was performed by Ms. Laura Radtke, Humboldt University, Department of Biology, Molecular Parasitology.

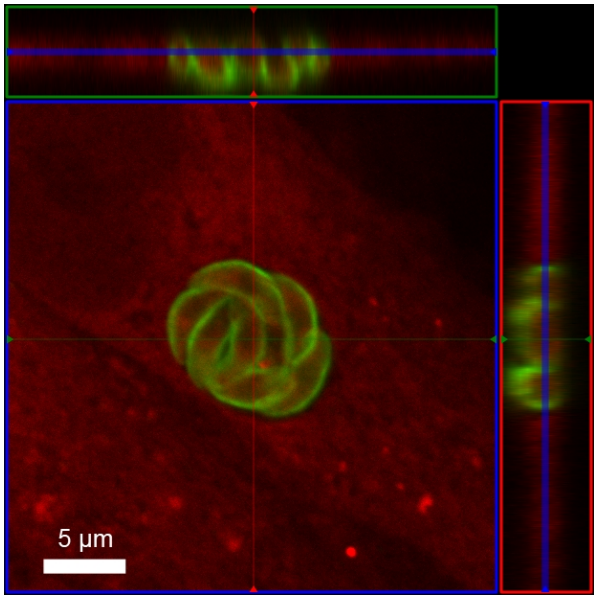


**Figure 3.19.** Z-stack confocal imaging of *T. gondii* infected HFF cells incubated with **ATTO@Glc-NCs )** (red) (green = SAG1). Scale bar = 5 µm.

## 3.2.3. Drug conjugation to Glc-NCs

Pyrimethamine is a drug used to treat both malaria and toxoplasmosis as it is active against both protozoan parasites.[174-175] Conjugation and quantification of pyrimethamine on **Glc-NCs** was carried out for further inhibition studies against *P. falciparum* and *T. gondii*.

Conjugation of pyrimethamine was performed through an amine-carboxylic acid coupling reaction, using the same conditions previously described (Chapter 2). Excess of drug was added to ensure the complete coverage of the nanocluster surface to yield **Pyr@Glc-NCs** (Scheme 3.3).

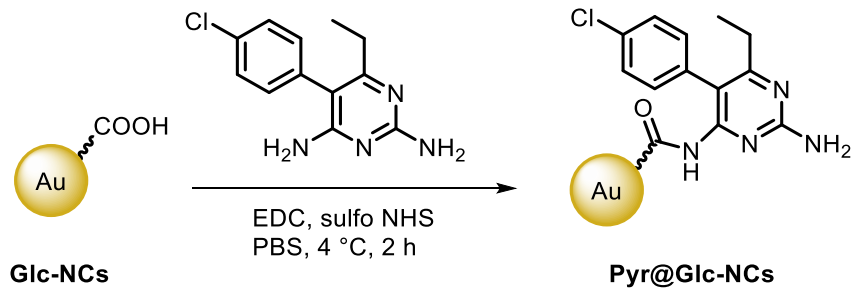


**Scheme 3.3.** Conjugation of the drug pyrimethamine to **Glc-NCs** to yield **Pyr@Glc-NCs**.

After dialysis purification, zeta (ζ) potential showed a decrease in the surface charge from -30 mV to -15 mV, due to drug functionalization through the carboxylic acid stabilizers (Figure 3.1).

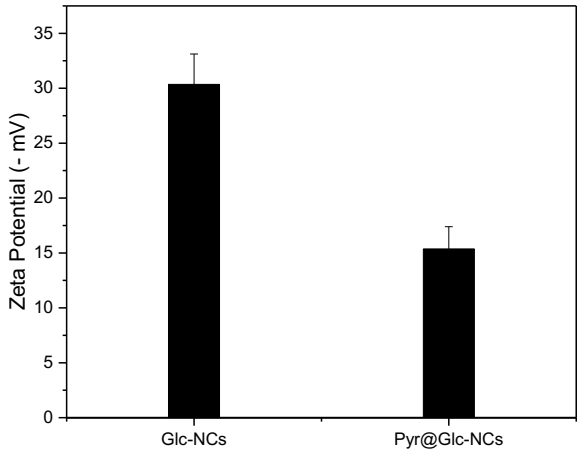


**Figure 3.20.** Zeta potential of **Glc-NCs** and **Pyr@Glc-NCs** show a difference in the surface charge due to drug conjugation.

Drug loading was quantified for further biological experiments. The UV spectrum of free pyrimethamine presented a band with a maximum at 211 nm (Figure 3.21).

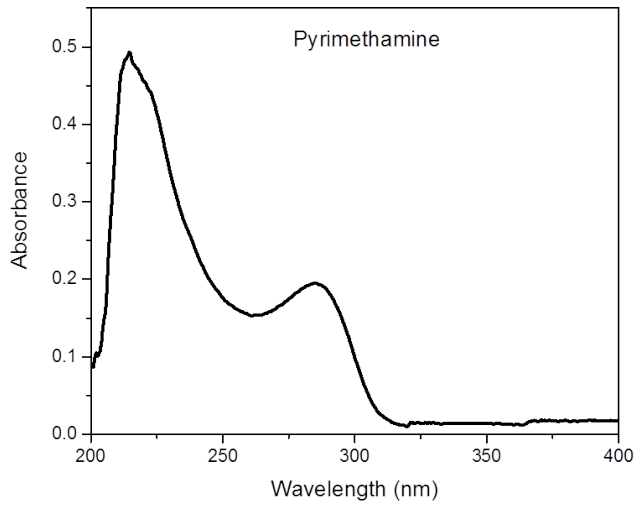


**Figure 3.21.** UV spectrum of free pyrimethamine that presents a maximum band at 211 nm.

A calibration curve was obtained by preparing stock solutions of pyrimethamine in DMSO in the concentration range from 0 to 1.25 μg/mL and measuring UV absorbance at 211 nm. A trendline was fit to the values giving an equation that could be further used to interpolate the concentration of loaded pyrimethamine on **Pyr@Glc-NCs** (Figure 3.22).

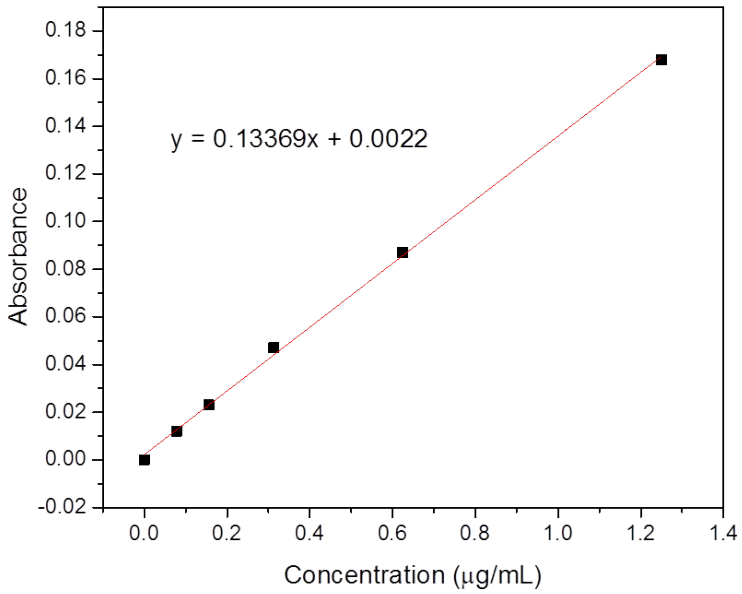


**Figure 3.22.** Calibration curve obtained by measuring the absorbance of free pyrimethamine at different concentrations (0 - 1.25 μg/mL) at 211 nm.

The absorbance value for pyrimethamine loading was calculated by subtracting the total signal of **Pyr@Glc-NCs** from that measured by only the **Glc-NCs**. To this end, the absorbance values of a sample of pristine **Glc-NCs**, prepared at equal concentration, were recorded as the control. The concentration of atomic gold can be quantified at 400 nm.[180] UV spectra showed a difference in the absorbance of the two bands at 211 nm that corresponded to the loading of pyrimethamine (Figure 3.23).

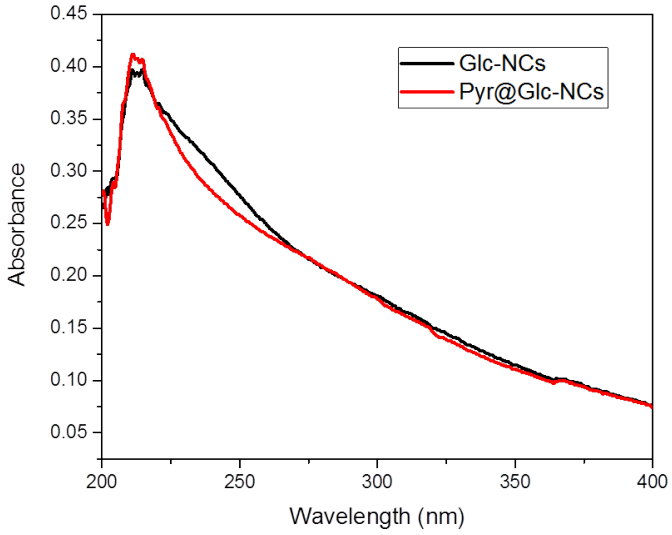


**Figure 3.23**. UV spectra of **Glc-NCs** and **Pyr@Glc-NCs** at same concentration (based on gold). The absorbance difference at 211 nm corresponds to the pyrimethamine loading in **Pyr@Glc-NCs**.

After interpolating in the calibration curve (Figure 3.22), the loading of pyrimethamine on **Pyr@Glc-NCs** was found to be 5 μg of pyrimethamine per μmol of atomic gold.

The drug loaded nanoclusters are currently being assessed *in vitro* with *P. falciparum* cultures, using free pyrimethamine in the same concentration range as control, in order to test whether targeted drug delivery permits the use of less quantities of drug.

# 3.3. Conclusion and Outlook

The protozoan parasites *P. falciparum* and *T. gondii* were targeted by gold nanoparticles through the high cysteine domains contained in the surface proteins of both parasites. The small size of **Glc-NCs** allowed for more accumulation on extracellular *P. falciparum* parasites compared to bigger gold nanoparticles. **Glc-NCs** were further tagged with a fluorescent dye for imaging studies. Confocal microscopy imaging showed that **Glc-NCs** were able to target both asexual and sexual blood stages of *P. falciparum,* but were not accumulating in healthy red blood cells.

**Glc-NCs** were able to bind and penetrate extracellular *T. gondii* parasites as shown by confocal microscopy. **Glc-NCs** were also able to target *T. gondii* inside human foreskin fibroblasts. Nevertheless, accumulation inside the host cells was also observed.

**Glc-NCs** were conjugated to the drug pyrimethamine that is active against *P. falciparum* and *T. gondii*. The pyrimethamine loaded **Glc-NCs** will be further used for inhibition experiments against both parasites both *in vitro* and *in vivo*.

# 3.4. Experimental part

## 3.4.1. General methods

All **reagents** were commercially purchased and used without further purification.

**Transmission electron microscopy** (TEM) measurements were performed on a Zeiss EM 912 Omega. The samples were prepared by immersion of grids into a small volume of the sample and subsequent solvent evaporation in a dust protected atmosphere.

**UV/Vis** spectra were recorded on Shimadzu UV-3600 spectrophotometer double-beam UV–VIS–NIR spectrometer and baseline corrected.

**ζ potential** was measured using a Malvern Zetasizer instrument in order to obtain the electrophoretic mobility of nanoparticles at different times of dialysis against MilliQ water. The Helmholtz-Smoluchowski equation was used to correlate the measured electrophoretic mobilities to the zeta potentials. Three replicates of each sample were measured six times at 25°C in MilliQ water.

**Confocal Microscopy** imaging was performed with a Zeiss LSM 710 confocal microscope system equipped with a 63x magnification, numerical aperture 1.3 of Zeiss LCI Plan-NEOFLUAR water immersion objective lens (Zeiss GmbH, Germany).

**Flow Cytometry** (FACS) analysis was acquired on a FACSCanto II flow cytometer (BD Biosciences, San Jose, CA, USA). Fluorescence of 10,000 living single cells was analyzed after monoparametric acquisition using the FITC Area parameter (excitation with a 488 nm Blue Laser, 585/42 nm emission filter). Data were analyzed with FlowJo analysis software (Tree Star Inc., Ashland, OR).

**Inductively Coupled Plasma Atomic Emission Spectrometry** (ICP-AES) for gold concentration determination was performed on an Optima 8000; Perkin Elmer, Massachusetts; USA. Samples were diluted to a total volume of 5 mL using aqueous aqua regia. An external calibration series from 0.1 mg/L to 5 mg/L was prepared using Au standard solution. The average of 3 measurements was obtained and the initial dilution was back-calculated.

## 3.4.2. Synthetic chemistry methods

### Citrate stabilized AuNPs (Cit-AuNPs)

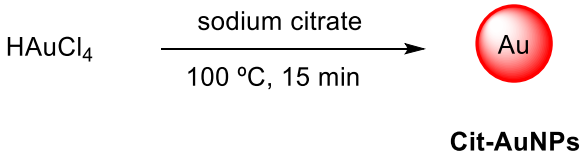


As previously reported,[135] a preheated solution of sodium citrate (10 mL, 1%) in MilliQ water was added to a solution of $HAuCl_4$ (100 mL, 500 µM) in MilliQ water under boiling

conditions (100 ºC). No refluxing was used to prevent the presence of temperature gradients within the liquid. After 15 minutes, the red solution was cooled to room temperature. The resulting **Cit-AuNPs** were dialyzed against 1.5 L MilliQ water three times.

**ATTO tagged Glc-NCs (ATTO@Glc-NCs)**

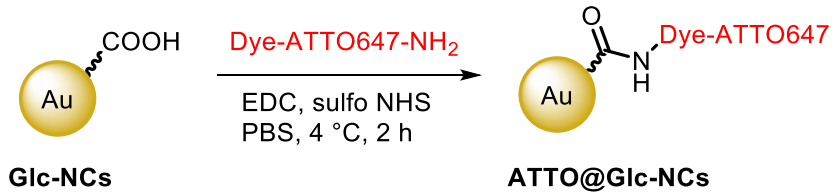


A solution of **Glc-NCs** (5.0 mL, 1.4 µmol Au, 6.11 $10^{15}$ nanoclusters) was diluted with 25 mL MilliQ water and 500 µL PBS. To this solution, 1-ethyl-3-(3-dimethylaminopropyl)carbodiimide (EDC, 6.5 mg, 34 µmol) and *N*-hydroxysulfosuccinimide (sulfo-NHS, 7.4 mg, 34 µmol) were added dropwise and the reaction was allowed to stir for 5 minutes under sonication in an ice bath. Subsequently, an aqueous solution of ATTO 647N dye (8.14 µL, 0.01 µmol) was added and allowed to react for 2 h under cold sonication bath. The resulting **ATTO@Glc-NCs** were dialyzed against 1.5 L MilliQ water three times.

**Cy5 tagged Glc-NCs (Cy5@Glc-NCs)**

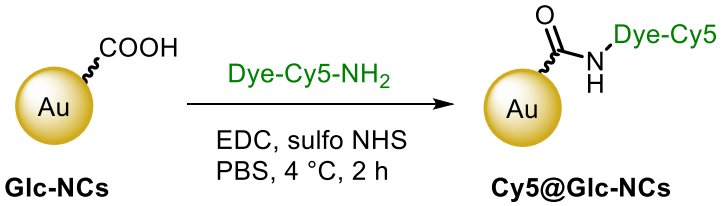


A solution of **Glc-NCs** (5.0 mL, 1.4 µmol Au, 6.11 $10^{15}$ nanoclusters) was diluted with 25 mL MilliQ water and 500 µL PBS. To this solution, EDC (6.5 mg, 34 µmol) and sulfo-NHS (7.4 mg, 34 µmol) were added dropwise and the reaction was allowed to stir for 5 minutes under sonication in an ice bath. Subsequently, an aqueous solution of Cy5-$NH_2$ dye (6.6 µL, 0.01 µmol) was added and allowed to react for 2 h under cold sonication bath. The resulting **Cy5@Glc-NCs** were dialyzed against 1.5 L MilliQ water three times.

**Pyrimethamine functionalized Glc-NCs (Pyr@Glc-NCs)**

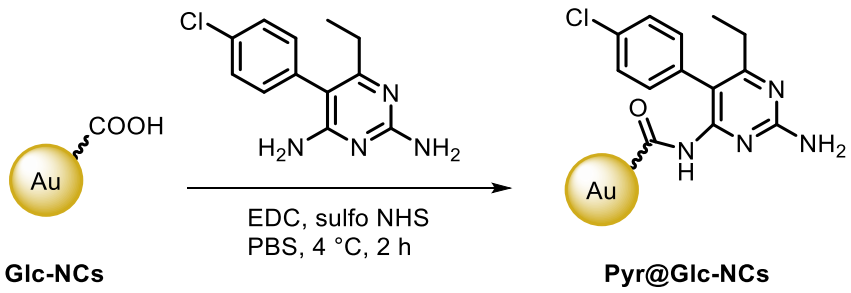


A solution of **Glc-NCs** (5.0 mL, 1.4 µmol Au, 6.11 $10^{15}$ nanoclusters) was diluted with 25 mL MilliQ water and 500 µL PBS. To this solution, EDC (6.5 mg, 34 µmol) and sulfo-NHS (7.4 mg, 34 µmol) were added dropwise and the reaction was allowed to stir for 5 minutes under sonication in an ice bath. Subsequently, a solution of pyrimethamine (0.03 mg, 0.12 µmol) in DMSO was added and allowed to react for 2 h under cold sonication bath. The resulting **Pyr@Glc-NCs** were dialyzed against 1.5 L MilliQ water three times.

## 3.4.3. Biology methods

### 3.4.3.1. *Plasmodium falciparum* asexual culture

The *P. falciparum* erythrocyte stages were cultured as previously reported.[181] The asexual growth medium was composed of RPMI 1640 supplemented with 2 mM L-glutamine, 5 mM HEPES buffer, 28 µg/mL hypoxanthine, 50 µg/mL gentamycin and 0.5% AlbuMAX™ II. Parasites were kept at 1% hematocrit in 150 $cm^2$ cell culture flasks at 37 °C under 5% $CO_2$.

**Thawing of *P. falciparum* glycerol-cryostocks**

Cryostocks of infected red blood cells (iRBCs) containing 3D7 *P. falciparum* strain were stored in 15% (v/v) glycerol and 1.5% (w/v) sorbitol in liquid nitrogen. The cryovial was thawed for 3 min in a 37 °C water bath and transferred into a 50 mL tube under sterile conditions. Subsequently, 0.1 times the volume of preheated thawing solution A (12% (w/v) NaCl) was added to the tube and the mixture was incubated for 5 min at room temperature. Then, 10 times the volume of preheated thawing solution B (1.6% (w/v) NaCl) was added dropwise while swirling the tube. The cell suspension was further centrifuged for 5 min at 300*g* and the pellet was washed once in 10 mL *P. falciparum* growth medium.

The washed cells were added to a 150 $cm^2$ cell culture flask containing 60 mL *P. falciparum* growth medium. Fresh red blood cells (RBC) of blood group O (ABO system) and Rhesus factor positive (Deutsches Rotes Kreuz e.V.) were added to a final hematocrit of 1%. The flask was maintained at 37 °C under 5% $CO_2$.

**Cultivation of *P. falciparum***

Life cycle stages as well as parasitemia were determined on a daily basis by light microscopy. For the microscope slide preparation, 1 mL of resuspended culture was centrifuged for 5 min at 300*g* and the supernatants were removed. The sample was smeared on the glass slides by taking 7.5 µL of the blood pellet. The slides were then allowed to dry and were further fixed with methanol. The parasites were then stained with UN 1230 Giemsa staining solution, diluted to 6% (v/v) with staining buffer (7 mM phosphate, pH 7.1) for visualization under the microscope.

**Sorbitol synchronization of *P. falciparum***

Sorbitol synchronization allows for enrichment of ring staged parasites in culture through lysis of most iRBCs containing mid and late trophozoites as well as schizonts. The parasite cultures were centrifuged for 5 min at 400*g*. The resulting pellet was resuspended in 5 times the pellet volume of sterile and preheated 5% sorbitol solution (in MilliQ water). Afterwards, the cultures were incubated for 10 min at 37°C and shaken every 3 min in vortex mixer. Subsequently, the cultures were washed twice (400*g*, 10 min) with growth medium and transferred into a 150 $cm^2$ cell culture flask containing 60 ml of medium. Fresh RBCs were added to a final hematocrit of 1%.

**Magnetic cell separation for schizont enrichment**

Since the haem moiety in the hemoglobin is diamagnetic, the iRBCs containing only mature parasites can be separated using magnetic-activated cell sorting (MACS) and LD columns. For this purpose, the LD columns were placed on a magnetic column holder and equilibrated using 2 mL of parasite growth medium. The cultures were centrifuged at 300*g* for 5 min to obtain the parasite pellets that were then loaded on the column followed by 4 mL of growth medium. The flow through containing RBCs and ring stage iRBCs was collected and the column containing mature parasites was finally removed from the magnet and eluted with 2 mL of growth medium by applying pressure.

**Saponin isolation of *P. falciparum* schizonts**

Saponin treatment leads to complete lysis of RBC and allows for the isolation of parasites. For this purpose, synchronized schizont stage cultures at very high parasitemia (>50%) were used. The cultures were therefore centrifuged (5 min, 400*g*) and resuspended in saponin solution (1 mL, 0.15%) and further incubated for 10 min in an ice bath, shaking the cultures every 3 min using a vortex mixer. The suspension was then centrifuged for 10 min at 2000*g* keeping the temperature at 4 °C and the supernatant was discarded. The pellets were washed several times with ice cold PBS until the supernatant became clear.

**Percoll synchronization of *P. falciparum***

Percoll synchronization allows for enrichment of mature staged parasites (schizonts) in the culture in a similar way as magnetic cell separation. The parasite cultures were centrifuged for 5 min at 300*g*. A solution of percoll 70% in PBS was pre-warmed and 1 mL of the pellet was gently deposited on top of this solution (using 15 mL falcon tubes). This resulting mixture was subsequently centrifuged at 800*g* for 10 min at 37 °C, putting the acceleration and brake to minimum. The resulting red upper layer is collected as it contains mature parasites and washed extensively with growth medium (300*g*, 5 min). The culture was then transferred into the culture flask or plate by adjusting (when required) the hematocrit to 1%.

### 3.4.3.2. *Plasmodium falciparum* sexual culture

The *P. falciparum* gametocytes stages were obtained by a modification of a previously reported protocol.[178] Parasites were kept at 5% hematocrit in 10-cm Petri dishes at 37 °C under 5% $CO_2$, 5% $O_2$, 90% $N_2$ and 60% humidity.

Different media were used:

The **asexual growth medium** was composed of RPMI 1640 supplemented with 2 mM L-glutamine, 5 mM HEPES buffer, 28 µg/mL hypoxanthine, 50 µg/mL gentamycin and 0.5% AlbuMAX™ II.

The **no-N-acetyl-glucosamine gametocyte medium (NNGM)** was composed of RPMI 1640 supplemented with 1 g of glucose, 28 µg/mL hypoxanthine, 25 mM of HEPES, and 0.5% AlbuMAX™ II. This medium could be stored for no longer than 3 weeks at 4 °C.

The **N-acetyl-glucosamine gametocyte medium (NGM)** was composed of RPMI 1640 supplemented with 1 g of glucose, 28 μg/mL hypoxanthine, 25 mM of HEPES, 5.8 g of *N*-acetyl-glucosamine, 0.5 mL of human serum and 0.5% AlbuMAX™ II. This medium could only be used when freshly prepared.

For the gametocyte induction, a first asexual culturing and synchronization is required in order to initiate a log growth during the first ten days. This asexual culturing is followed by a gametocyte induction by mimicking host anemia through total RBC replacement, as well as by reducing the hematocrit from 5 to 1.25%. A further increase of % parasitemia also produces stressed parasites that induce gametocytogenesis. These parameters can be achieved by using either magnetic separation or percoll synchronization. Once the gametocytes are induced, they can be isolated depending on the early or late stage.

Early staged gametocytes can be isolated by changing the asexual growth medium to NNGM, doing percoll synchronization in NGM instead of asexual growth medium. The gametocytes can then be used for confocal microscopy imaging. Parasites were kept at 5% hematocrit in 10-cm Petri dishes at 37 °C under 5% $CO_2$, 5% $O_2$, 90% $N_2$ and 60% humidity.

Late staged gametocytes can be isolated by changing the medium to NGM and doing percoll synchronization using NGM instead of the asexual growth medium. The gametocytes can then be used for confocal microscopy imaging. Parasites were further kept at 5% hematocrit in 10-cm Petri dishes at 37 °C under 5% $CO_2$, 5% $O_2$, 90% $N_2$ and 60% humidity.

### 3.4.3.3. ICP-AES

Isolated mature parasites (by saponin) were thawed and washed with PBS (3000*g*, 5 min), and 500 μL of PBS was added to resuspend the pellet. Three different concentrations of **Glc-NCs** and **Cit@AuNPs** were used (5, 20, 50 μM). For each experiment, 20 μL of the resuspended parasites were incubated with 1 mL of each gold nanoparticle solution in PBS, for 15 min. The parasites were further washed three times with PBS (3000*g*, 5 min) and the pellet was treated with aqua regia and measured with ICP-AES.

### 3.4.3.4. Flow cytometry

Flow cytometry is a very powerful technique that is able to analyze cells depending on morphology features by means of light scattering as well as give information about binding of fluorescent labelled probes.

**Parasitemia determination**

As RBCs do not contain DNA, the iRBCs can be distinguished by using a DNA staining dye (SYBR™ Green). For this purpose, 500 µL of a resuspended culture (containing 5 µL of RBCs) was centrifuged (300*g*, 5 min) and further washed with PBS. The pellet was then resuspended in 150 µL of PBS. Finally, 1 mL of PBS containing 4% PFA, 1 µL of the resuspended parasites and a solution of SYBR™ Green (dilution 1:10,000) were incubated for 20 min in absence of light. Non infected RBCs were used as control. The measurements were performed using a FITC channel.

**Binding studies with ATTO@Glc-NCs**

The parasitemia of a synchronized culture (rings, trophozoites or schizonts) was determined as previously described to adjust it to 1 and 10% parasitemia by adding fresh RBC. The experiment was performed using both % parasitemia. Then, 500 µL of a resuspended culture (containing 5 µL of RBCs) as well as 5 µL non-infected RBC were centrifuged (300*g*, 5 min) and further washed with PBS. Subsequently, 1 mL of a dilution of **ATTO@Glc-NCs** (20 µM concentration based on Au) in growth medium and PBS was added to each sample. To prepare this solution, 500 µL of **ATTO@Glc-NCs** (40 µM concentration based on Au) was diluted with 500 µL of growth medium and 50 µL of 10x PBS. The diluted **ATTO@Glc-NCs** were incubated with the parasites for 15 min under shaking and in the dark. The parasites were then thoroughly washed 3 times with PBS (300*g*, 5 min) and finally resuspended in 150 µL of PBS. Subsequently, 1 mL of PBS containing 4% PFA, 1 µL of the resuspended parasites and a solution of SYBR™ Green (dilution 1:10,000) were incubated for 20 min in absence of light. Non infected RBCs were used as control. The measurements were performed using a FITC channel to detect parasitemia and APC channel to detect **ATTO@Glc-NCs**. Non infected RBCs (treated and not treated with **ATTO@Glc-NCs**), as well as iRBC not treated with **ATTO@Glc-NCs** were used as control. Experiments were done in triplicates.

### 3.4.3.5. Confocal microscopy

For confocal imaging binding studies of both asexual and sexual cultures, 500 µL of a resuspended culture (containing 5 µL of RBCs) as well as 5 µL non-infected RBC were centrifuged (300*g*, 5 min) and further washed with PBS. Subsequently, 1 mL of a dilution of **ATTO@Glc-NCs** (20 µM concentration based on Au) in growth medium and PBS was added to each sample. To prepare this solution, 500 µL of **ATTO@Glc-NCs** (40 µM concentration based on Au) was diluted with 500 µL of growth medium and 50 µL of 10x PBS. The diluted **ATTO@Glc-NCs** were incubated with the parasites for 15 min under shaking and protected from light. The parasites were then thoroughly washed 3 times with PBS (300*g*, 5 min) and finally fixed by incubation with 500 µL of PBS containing 4% PFA for 15 min. Parasites were then centrifuged one more time and resuspended in 30 µL of PBS. To this suspension, 30 µL of mounting solution containing DAPI was added and carefully mixed. Finally, 10 µL of this mixture was put on a glass slide, covered with a glass cover and fixed with nail polish. Non-infected RBCs (treated and not treated with **ATTO@Glc-NCs**), as well as iRBC not treated with **ATTO@Glc-NCs** were used as control.

### 3.4.3.6. Hemolysis assay

The parasitemia of a synchronized culture (rings, trophozoites or schizonts) was determined as previously described to adjust it to 1 and 10% parasitemia by adding fresh RBC. The experiment was performed using both % parasitemia. Then, 500 µL of a resuspended culture (containing 5 µL of RBCs) as well as 5 µL non-infected RBC were centrifuged (300*g*, 5 min) and further washed with PBS. Different concentrations of 300 µL of **Glc-NCs** in PBS (50, 25, 12.5, 2.5, 0.25, 0.025 and 0.0025 µM concentration based on Au) were incubated with the cultures for 15 min. The different samples were then centrifuged (300*g*, 5 min) and 50 µL of the supernatants were put in a Greiner 96 V Bottom Transparent Polystyrol in triplicates. The absorbance at 540 nm was read using a plate reader. Supernatants of RBC and iRBC treated with PBS (negative control) and saponin (positive control) were also measured.

# 4. Breakable mesoporous silica nanodiscs for drug delivery

This chapter has been modified in part from the following article:

Reshaping silica particles: Mesoporous nanodiscs for bimodal delivery and improved cellular uptake. V. Giglio, S. Varela-Aramburu, L. Travaglini, F. Fiorini, P. H. Seeberger, L. Maggini, L. de Cola, *Chem. Eng. J.* 2018, 340, 148-154.[182] https://doi.org/10.1016/j.cej.2018.01.059

# 5. Synthesis of multivalent glycosylated nanoparticles for imaging

## 5.1. Introduction

Glycosylated nanoparticles are used to mimic multivalent systems in nature and give information about biological processes that occur through carbohydrate-carbohydrate (CCIs) and carbohydrate-protein interactions (CPIs). There are three main conjugation strategies used to glycosylate nanoparticles: covalent bond formation through amides or ester bonds, direct conjugation to metal surfaces (i.e. thiol chemistry), and [3+2] cycloaddition (click) chemistry (Figure 5.1).[216]

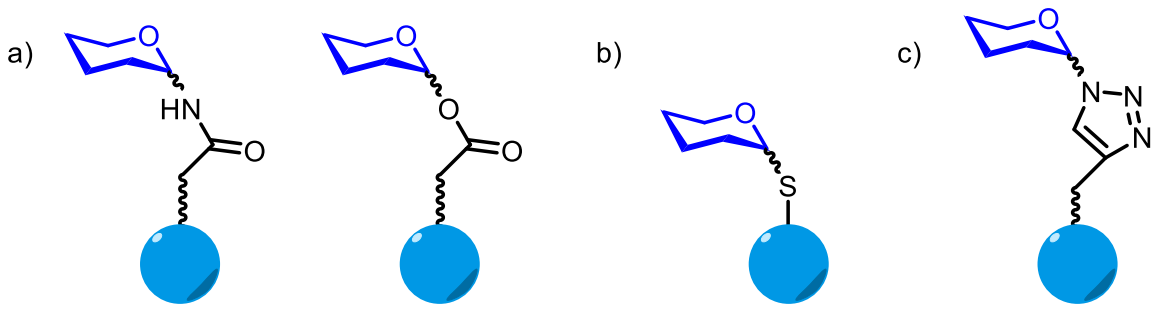


**Figure 5.1.** Conjugation strategies for glycosylation of nanoparticles through a) coupling reaction to form amides or esters, b) thiol conjugation to metals, and c) click chemistry.

Coupling reactions to form amides and esters are common methods to functionalize surfaces, as there are orthogonal to other strategies, such as click chemistry.[216]

Direct conjugation of thiols to metal nanoparticles has been exploited for plasmonic assays such as surface plasmon resonance (SPR) or surface-enhanced Raman spectroscopy (SERS), as it provides a stable bond that can be further utilized for biomolecular interactions studies. The addition of mixed thiol ligands allows for multiple functionalization, but the exact control of the nanoparticle loading remains a challenge.[216]

Click reactions are an attractive surface functionalization strategy due to the orthogonality to other conjugation strategies. Nevertheless, the use of copper as a catalyst is often problematic to purify as it can be trapped at the surface or even bind triazoles. Moreover, terminal alkynes are also able to bind metal surfaces through non-specific interactions.[217]

In this chapter, glycosylation of nanoparticles was performed to promote the blood brain barrier crossing and to monitor the CPIs between cyanobacteria and microalgae. Glucose was conjugated through a coupling reaction to the surface of ultrasmall silicon nanoparticles (SiNPs) in order to enable the blood brain barrier (BBB) crossing. Ultrasmall SiNPs have already been used as multivalent glycosylated scaffolds as they can be exploited for multivalent conjugation, they exhibit fluorescent properties for imaging and they provide easy conjugation and low cytotoxicity.[54-55] The double conjugation of glucose and a chelator that hosts a radiotracer was carried out for further *in vivo* studies in mice.

Gold nanoparticles (AuNPs) functionalized with different carbohydrates were also synthesized in order to study CPIs between microalgae and cyanobacteria as they form cell-cell aggregates. Green algae express mannosides on the surface and cyanobacteria contain external lectins.[218] To further explore the CPIs between the mannosides and the cyanobacteria, a collection of different carbohydrates was synthesized and conjugated to gold nanoparticles through thiol conjugation. The glycosylated nanoparticles will be further tested using confocal microscopy to analyze the structure that provides the highest affinity to the lectin.

# 5.2. Results

## 5.2.1. Glucose-functionalized silicon nanoparticles for brain imaging

Fluorescent ultrasmall silicon nanoparticles (SiNPs)[g] that have a size of 4 nm, can be used for brain targeting and imaging. SiNPs were functionalized with glucose, to target the brain, and the chelator 1,4,7-triazacyclononane-1,4,7-trisacetic acid (NOTA), for radiolabeling.

[g] **SiNPs** were synthesized by Mr. John Ddungu and Ms. Alessandra Tassoni from the group of Prof. Luisa De Cola, Université de Strasbourg, CNRS, ISIS, Strasbourg, France.

As SiNPs were stabilized with amines, compound **4** was equipped with a carboxylic acid (**5**),[h] using succinic anhydride in the presence of *N,N*-diisopropylethylamine (DIPEA) (Scheme 5.1).

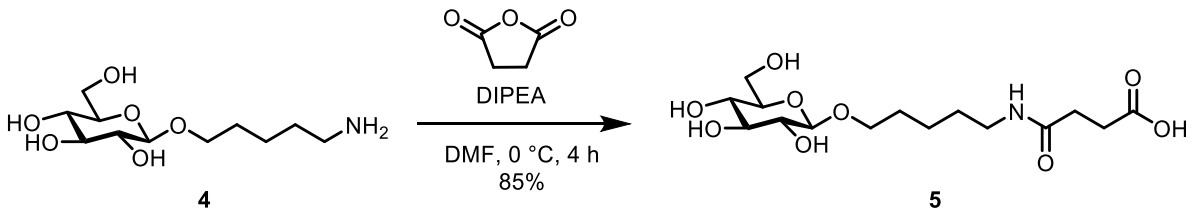


**Scheme 5.1.** Synthesis of carboxylic acid functionalized glucoside **5.**

SiNPs functionalized with a NOTA chelator (**SiNPs-NOTA**)[i] were conjugated to the carboxylic acid modified glucoside **5** through an amide coupling reaction using EDC/NHS activation, in PBS buffer to yield **Glc@SiNPs-NOTA** (Scheme 5.2). The product was further purified, firstly by dialysis against MilliQ water for two days, and afterwards by size exclusion column to remove unreacted glucosides.

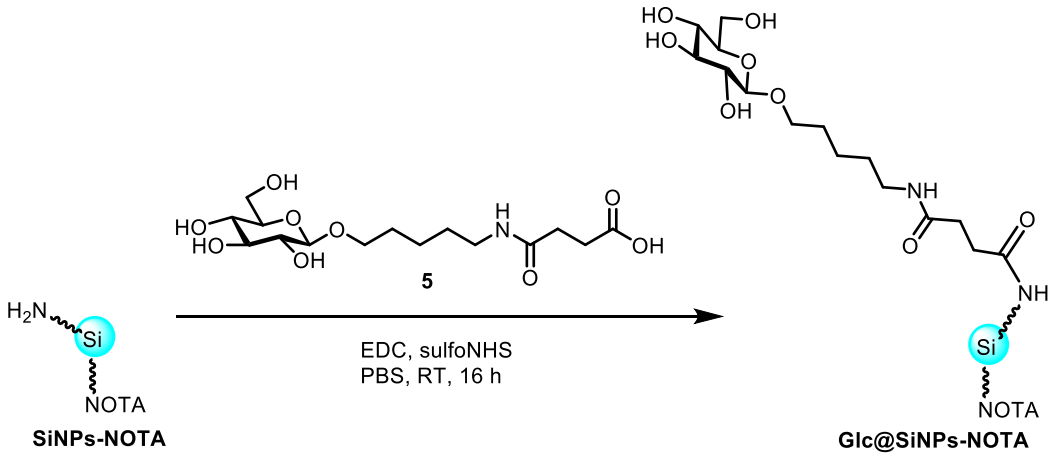


**Scheme 5.2.** Conjugation of **SiNPs-NOTA** to the glucoside **5** using EDC/NHS activation to yield **Glc@SiNPs-NOTA.**

Dynamic light scattering (DLS) showed a slight increase in the size of **Glc@SiNPs-NOTA** (Figure 5.2 b), when compared to **SiNPs-NOTA** due to the sugar functionalization (Figure

[h] Compound **4** was synthesized by Dr. Chian-Hui Lai

[i] **SiNPs-NOTA** were functionalized by Ms. Garima Singh, from the group of Dr. Holger Stephan, Institute of Radiopharmaceutical Cancer Research, Helmholtz-Zentrum Dresden - Rossendorf (HZDR), Germany.

5.2 a). The zeta (ζ) potential decreased slightly for **Glc@SiNPs-NOTA** compared to **SiNPs-NOTA** due to glucose functionalization (Figure 5.2).

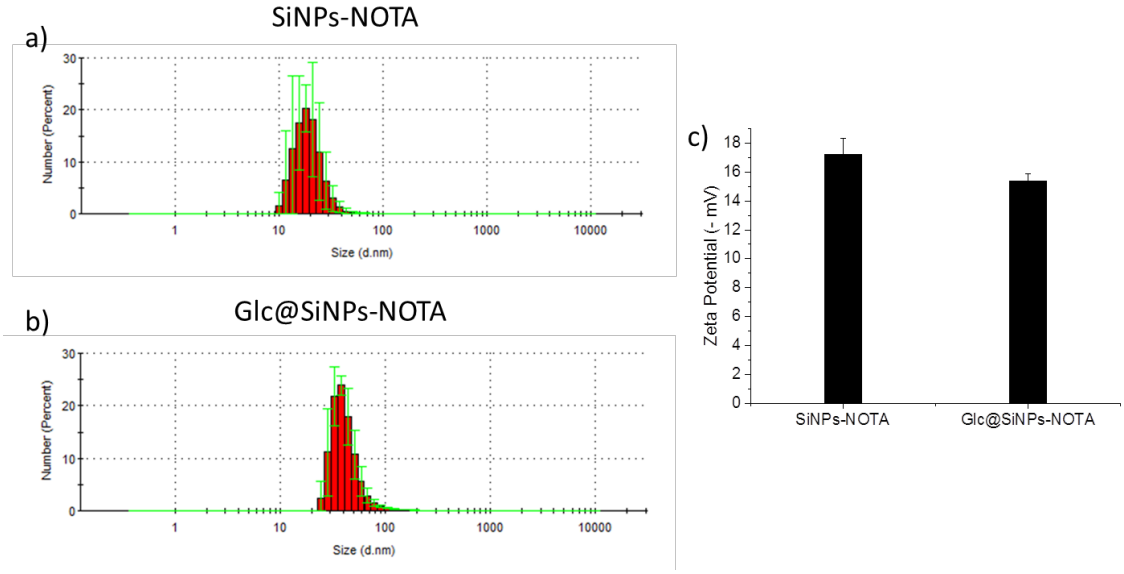


**Figure 5.2.** Dynamic light scattering of a) **SiNPs-NOTA** and b) **Glc@SiNPs-NOTA**, and c) Zeta potential of **SiNPs-NOTA** and **Glc@SiNPs-NOTA**.

Infrared spectroscopy (IR) confirmed the functionalization of **Glc@SiNPs-NOTA** as the spectrum showed the appearance of characteristic bands (Figure 5.3). **SiNPs-NOTA** had still available amine groups as stabilizer, which were detected by the N-H bending at 1600 $cm^{-1}$. In **Glc@SiNPs-NOTA** the band at 1640-1690 $cm^{-1}$ corresponds to the C-O stretch and the band at 1550 $cm^{-1}$ is a result of the N-H bending by the amide formation. Moreover, the hydroxyl groups of the glucose can be seen through the band at 1050-1150 $cm^{-1}$ (C-O stretch).

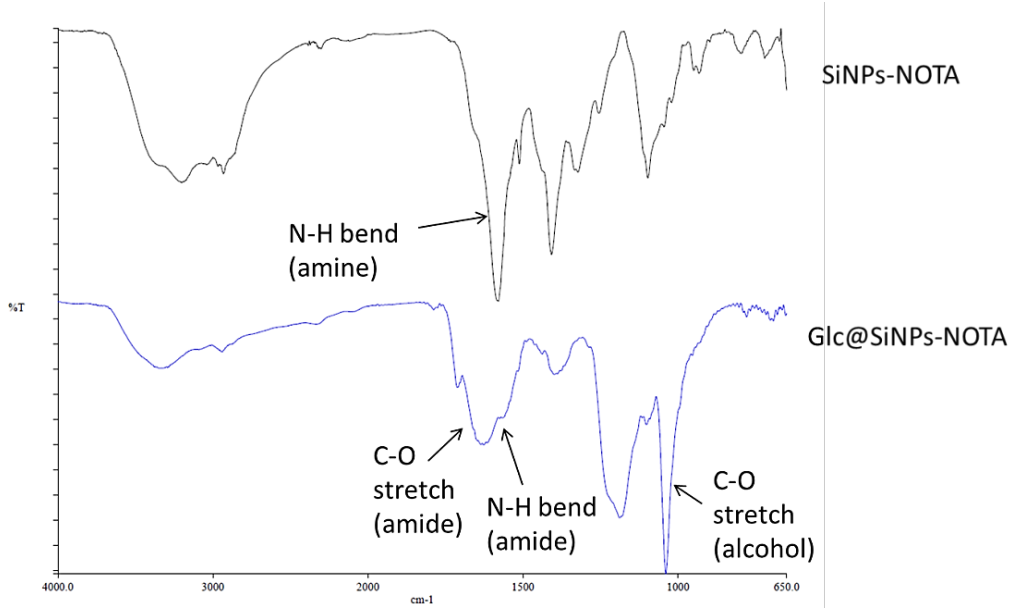


**Figure 5.3.** IR spectra of **SiNPs-NOTA** (above) and **Glc@SiNPs-NOTA** (below).

The loading of glucose on **Glc@SiNPs-NOTA** was quantified by using the anthrone method.[112] Anthrone reacts with hexoses in the presence of sulfuric acid, to form a colored compound that can be detected by UV spectroscopy (Scheme 5.3). The reaction is concentration dependent and can be monitored by measuring the absorbance at 620 nm.

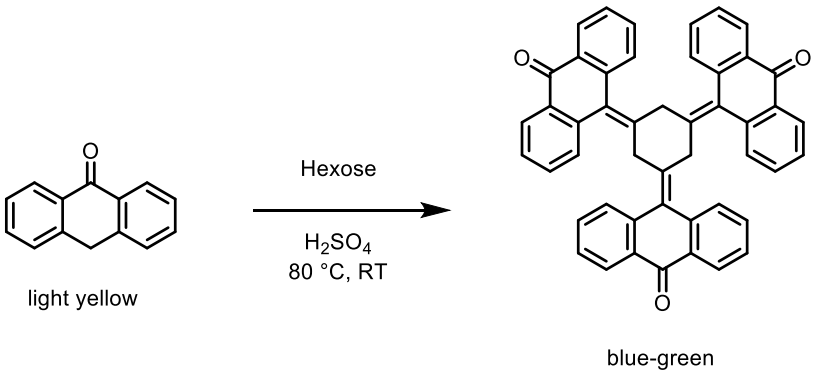


**Scheme 5.3.** Colorimetric reaction between anthrone and hexoses in acidic conditions.

Stock solutions of glucose in water (0.25 - 0 mg/mL) were prepared and allowed to react with anthrone under acidic conditions. The absorbance was then measured at 620 nm to obtain a calibration curve (Figure 5.4). Interpolation of the absorbance values of **Glc@SiNPs-NOTA**, after subtracting the value of **SiNPs-NOTA**, gave the loading of glucose, which was found to be 0.3 μmol glucose per mg **SiNPs-NOTA**.

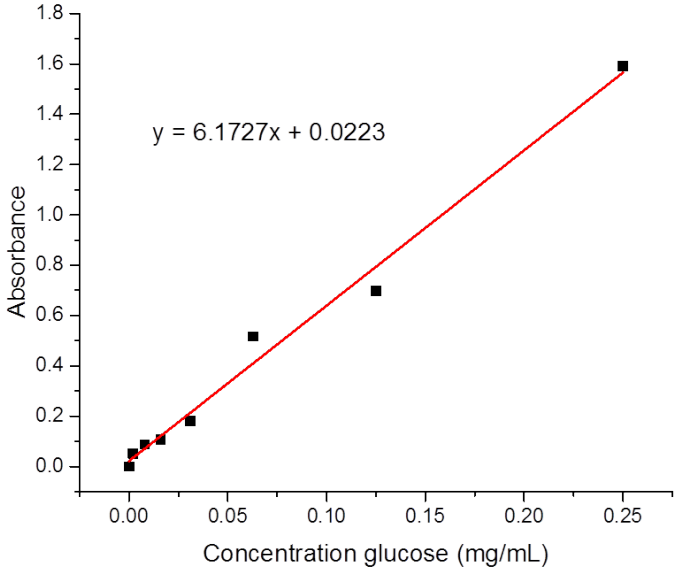


**Figure 5.4.** Calibration curve for glucose quantification in **Glc@SiNPs-NOTA**.

The fully characterized **Glc@SiNPs-NOTA** were sent to the group of Dr. Holger Stephan at Institute of Radiopharmaceutical Cancer Research, Helmholtz-Zentrum Dresden - Rossendorf (HZDR), Germany. Radiolabeling and *in vivo* studies in mice are currently under investigation to test whether the nanoparticles are able to cross the blood brain barrier.

## 5.2.2 Glycosylated gold nanoparticles for CPIs studies

Gold nanoparticles (AuNPs) with a plasmon band can be used as a multivalent platform for interactions studies using confocal microscopy.[219] Citrate stabilized nanoparticles (**Cit-AuNPs**) were synthesized[j] as they show a plasmon band at ~520 nm that can be imaged with confocal microscopy. A collection of different carbohydrates[k] (Figure 5.5) were synthesized and conjugated to **Cit-AuNPs** in order to monitor the structure that has more affinity to the lectin exposed on cyanobacteria. Mannoside **6** and **8** were selected to understand whether there is a difference in monosaccharide vs disaccharide binding. The galactoside **7** was chosen as a control as it should not bind the lectin.

[j] Synthesis of **Cit-AuNPs** is shown in Chapter 3.

[k] Collection of carbohydrates **6**, **7** and **8** were synthesized by Dr Martina Delbianco.

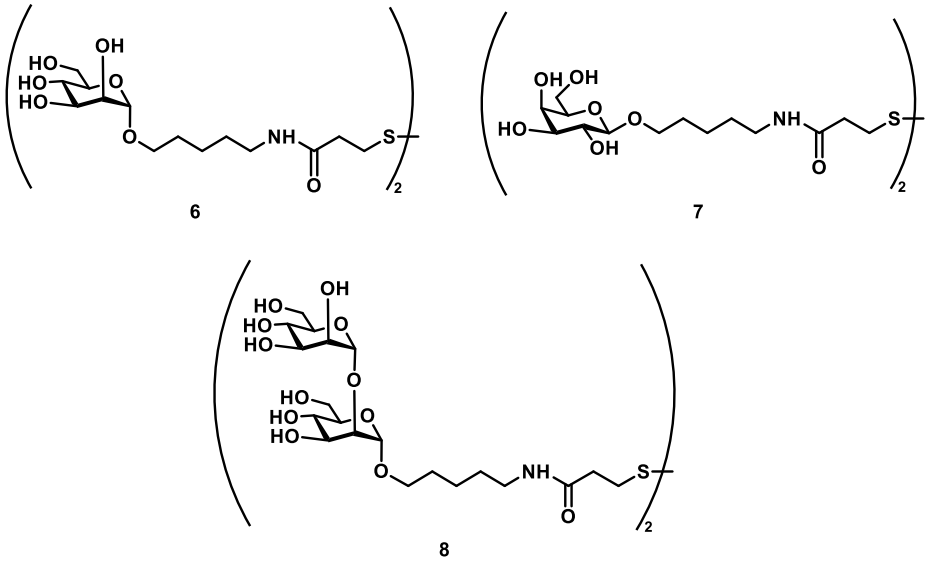


**Figure 5.5.** Selection of thiolated carbohydrates conjugated to **Cit-AuNPs** for CPIs studies between green algae and cyanobateria.

Conjugation of carbohydrates **6**, **7** and **8** to **Cit-AuNPs** was carried out by adding an excess of the compounds at room temperature and was allowed to react for 24 h to ensure complete functionalization (Scheme 5.4). The products (**Man@AuNPs**, **DiMan@AuNPs** and **Gal@AuNPs**) were purified by dialysis against MilliQ water.

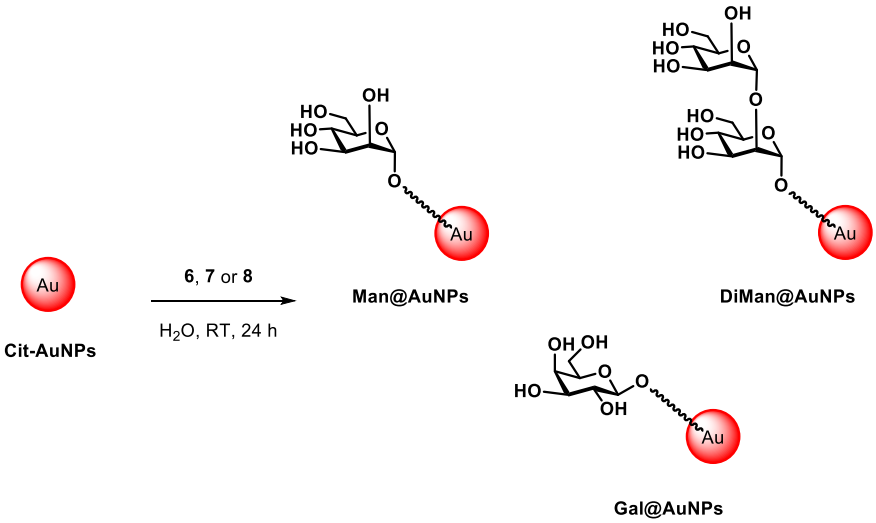


**Scheme 5.4.** Conjugation of compoiunds **6**, **7** and **8** to **Cit-AuNPs** to yield **Man@AuNPs**, **Gal@AuNPs** and **DiMan@AuNPs**, respectively.

After conjugation of the different carbohydrates, plasmon resonance was measured with UV and the size and morphology was assessed with transmision electron microscopy (TEM) in order to see if the reaction conditions affected the physical properties of the

nanoparticles (Figure 5.6). The plasmon band was detected in the three samples at 527 nm and the particle size was found to be ~20 nm.

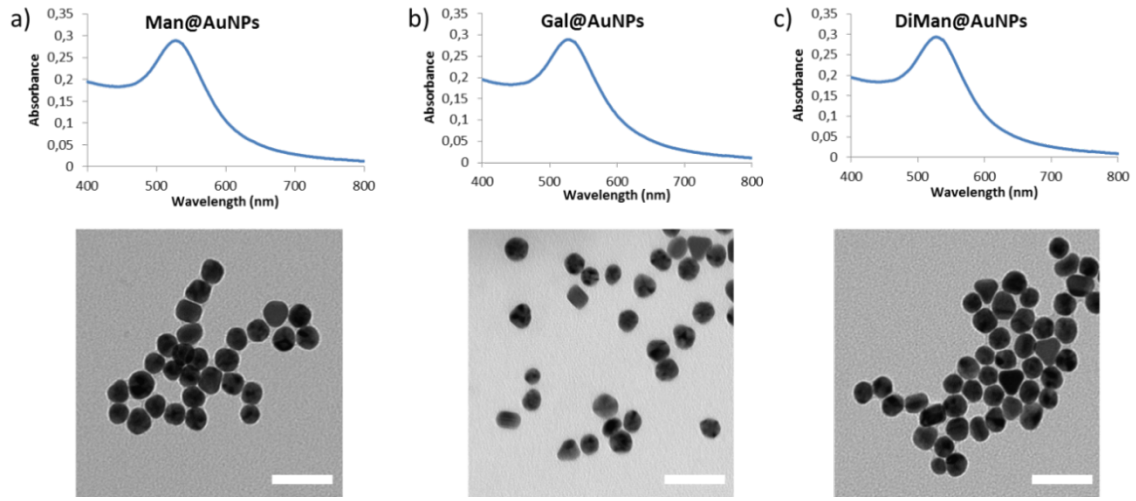


**Figure 5.6.** UV spectra (above) and transmission electron microscopy (below) of a) **Man@AuNPs**, b) **Gal@AuNPs**, and c) **DiMan@AuNPs**. Scale bar = 50 nm

ζ potential was measured in order to analyze the surface charge difference after nanoparticle functionalization. The ζ potential values became significantly more negative after carbohydrate conjugation, as **Cit-AuNPs** showed a ζ potential of -20 mV and after carbohydrate conjugation the surface ζ potential decreased to values between -30 and -40 mV. This suggests an increase in the stability of the carbohydrate functionalized nanoparticles (Figure 5.7).

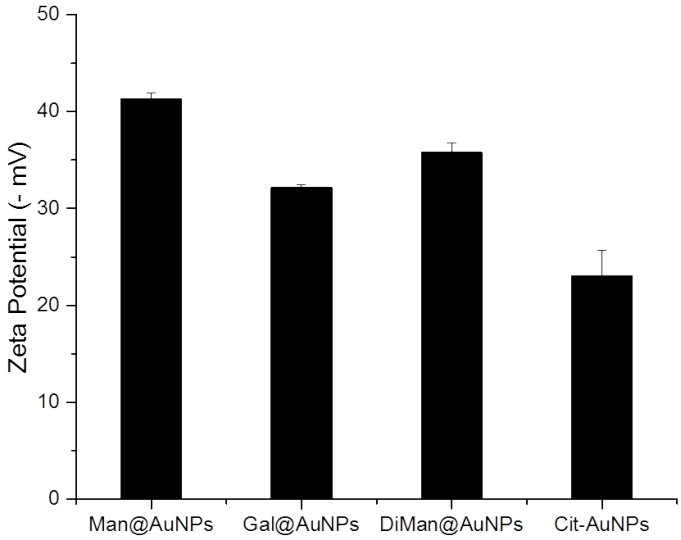


**Figure 5.7.** Zeta potential of **Man@AuNPs**, **Gal@AuNPs**, **DiMan@AuNPs** and **Cit-AuNPs**.

The difference in the ζ potential between the three carbohydrate-conjugated samples could be explained due to difference in the loading of the glycoconjugates. Carbohydrate loading was calculated by using the previously described anthrone method (Section 5.2). For this, two calibration curves were obtained: one using a monosaccharide as standard and the other using a disaccharide as standard. (Figure 5.8)

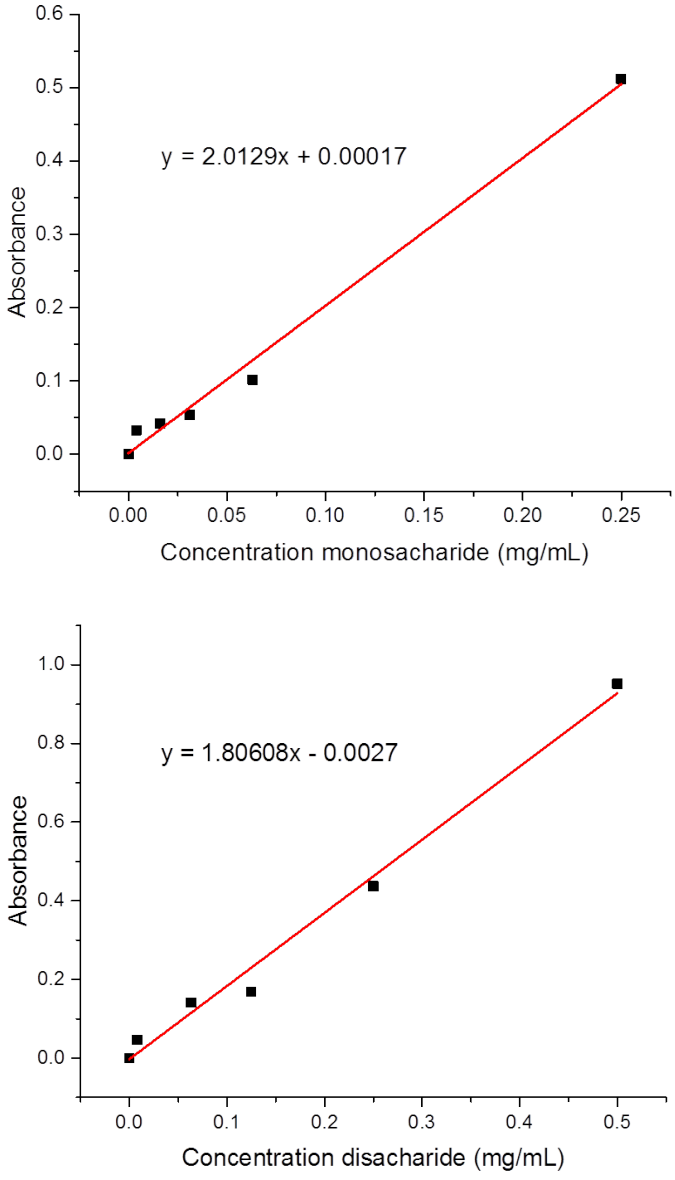


**Figure 5.8.** Calibration curve for the sugar quantification of **Man@AuNPs**, **Gal@AuNPs**, using monosaccharide standards (above) and **DiMan@AuNPs** using disaccharide standards (below).

Interpolation in the calibration curves gave the loading of the different carbohydrates that was expressed by μg carbohydrate per μmol of atomic gold (Table 5.1). These results are in agreement with Zeta potential, as less loading shows a lower zeta potential value.

**Table 5.1.** Carbohydrate loading on **Man@AuNPs**, **Gal@AuNPs** and **DiMan@AuNPs** calculated from the calibration curves.

| | **Man@AuNPs** | **Gal@AuNPs** | **DiMan@AuNPs** |
|---|---|---|---|
| **Loading (μg/μmol)** | 61.5 | 36.9 | 49.3 |

The three samples (**Man@AuNPs**, **Gal@AuNPs** and **DiMan@AuNPs**) were sent to the group of Dr. Thomas R. Neu, Department of River Ecology at Helmholtz Centre for Environmental Research Magdeburg, Germany. CPIs studies with confocal microscopy are currently under investigation.

# 5.3. Conclusion and outlook

Glycosylated nanoparticles were used to create multivalent platforms to gain a better insight into complex biological processes that involve carbohydrates. In particular, ultrasmall silicon nanoparticles have the proper size to potentially cross the BBB. For this purpose, silicon nanoparticles were functionalized with glucose to target the brain, and a chelator to host a radiotracer for imaging. The fully characterized material is currently being studied in a mouse model. Conjugation of pharmaceuticals to glycosylated ultrasmall nanoparticles can open opportunities to treat severe brain diseases such as brain tumors, cerebral malaria, Parkinson's disease or Alzheimer's disease.

Plasmonic nanoparticles were conjugated to different carbohydrates for binding studies between green microalgae and cyanobacteria using CLSM. The adhesion process is known to occur though CPIs, but the exact structure of the carbohydrate epitope involved in the binding is unknown. Synthesis of a collection of carbohydrates can give information of the structure that gives the highest affinity to the lectin.

# 5.4. Experimental section

## 5.4.1. General methods

All **reagents** were commercially purchased and used without further purification. Anhydrous solvents were obtained from a Dry Solvent System (jcmeyer-solvent system). Air sensitive reactions were carried out using oven-dried glassware and under an atmosphere of argon or nitrogen.

Thin-layer **chromatography** (TLC) was carried out on ALUGRAM® Xtra SIL plates pre-coated with silica gel of 0.20 mm thickness (Macherey-Nagel). TLC spots were visualized either under UV irradiation (254/366 nm) or by dipping the TLC in sugar stain (0.1% (v/v) 3-methoxyphenol, 2.5% (v/v) sulfuric acid in EtOH).

**Lyophilized** water containing samples were performed using an Alpha 2-4 LD Lyophilizer (Christ, Osterode am Harz, Germany)

**$^{1}$H and $^{13}$C** and two dimensional **NMR** data were obtained on Bruker ECX 400 MHz, amd Varian 400 MHz NMR spectrometers.

**FTIR** spectra were recorded on a Spectrum 100 FT-IR spectrometer (Perkin Elmer). The samples were spotted as a solid on the detector before measurements.

**Transmission electron microscopy** (TEM) measurements were performed on a Zeiss EM 912 Omega. The samples were prepared by immersion of grids into a small volume of the sample and subsequent solvent evaporation in a dust protected atmosphere.
**UV/Vis** spectra were recorded on Shimadzu UV-3600 spectrophotometer double-beam UV–VIS–NIR spectrometer and baseline corrected.

**Dynamic light scattering (**DLS) measurements were carried out at a scattering angle of 173° with a Malvern Zeta Nanosizer working at 4-mW He–Ne laser (633 nm). The **Glc-NCs** were measured in MilliQ water.

**ζ potential** was measured using a Malvern Zetasizer instrument in order to obtain the electrophoretic mobility of nanoparticles at different times of dialysis against MilliQ water. The Helmholtz-Smoluchowski equation was used to correlate the measured electrophoretic

mobilities to the zeta potentials. Three replicates of each sample were measured six times at 25 °C in MilliQ water.

## 5.4.2. Synthetic chemistry methods

**4-oxo-4-((5-(((2R,3R,4S,5S,6R)-3,4,5-trihydroxy-6-(hydroxymethyl)tetrahydro-2*H*-pyran-2-yl)oxy)pentyl)amino)butanoic acid (5)**

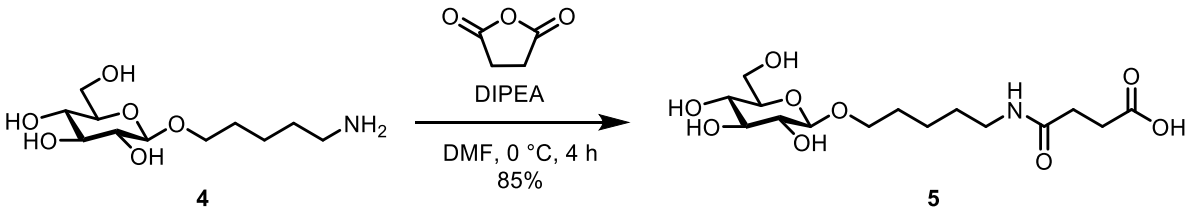


**4** **5**

Compound **4** (15 mg, 57 µmol) was dissolved in 2 mL DMF and DIPEA (10 µL, 57 µmol) was added at 0 °C. Then, succinic anhydride (5.7 mg, 57 µmol) was added and the mixture was allowed to stir for 4 h at 0 °C. The reaction mixture was diluted with water and concentrated in vacuum. The crude compound was purified using a Chromafix® C18 column (water/MeOH 1:4) to obtain the desired compound **5** (17.5 mg, 85% yield).

$^{1}$H NMR (400 MHz, $D_2O$) δ 4.32 (d, *J* = 8.0 Hz, 1H), 3.82 – 3.78 (m, 1H), 3.77 (q, *J* = 2.2, 1.5 Hz, 1H), 3.62 – 3.50 (m, 2H), 3.38 – 3.28 (m, 2H), 3.24 (dd, *J* = 9.8, 8.9 Hz, 1H), 3.12 (dd, *J* = 9.3, 8.0 Hz, 1H), 3.06 (t, *J* = 6.8 Hz, 2H), 2.52 – 2.47 (m, 2H), 2.38 (t, *J* = 6.6 Hz, 2H), 1.51 (dq, *J* = 14.4, 6.8 Hz, 2H), 1.40 (p, *J* = 7.0 Hz, 2H), 1.29 – 1.20 (m, 2H). $^{13}$C NMR (101 MHz, $D_2O$) δ 177.58, 174.70, 102.06, 75.80, 75.70, 73.04, 70.28, 69.56, 60.65, 39.09, 30.64, 30.00, 28.25, 27.90, 22.29. LC MS calculated for $[M-H]^-$ 364.2 $C_5H_{27}NO_9$, found 364.2.

**Glucose functionalized silicon nanoparticles containing NOTA (Glc@SiNPs-NOTA)**

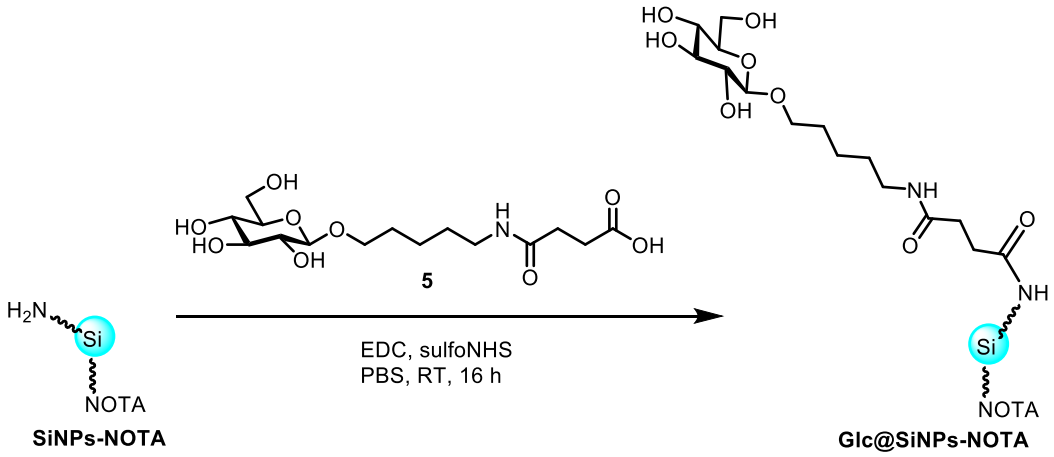


Compound **5** (9 mg, 23 µmol) was dissolved with 20 mL MilliQ water. To this solution, 1-ethyl-3-(3-dimethylaminopropyl)carbodiimide (EDC, 20 mg, 129 µmol) and *N*-hydroxysulfosuccinimide (sulfo-NHS, 25 mg, 129 µmol) in PBS were added dropwise and allowed to stir for 5 min. Subsequently, an aqueous solution of **SiNPs-NOTA** (5 mg, 2 mL) was added and allowed to react for 24 h. The resulting **Glc@SiNPs-NOTA** were dialyzed against 1.5 L MilliQ water three times and purified with size exclusion column PD10 (Sephadex) using MilliQ water.

**Mannose functionalized gold nanoparticles (Man@AuNPs)**

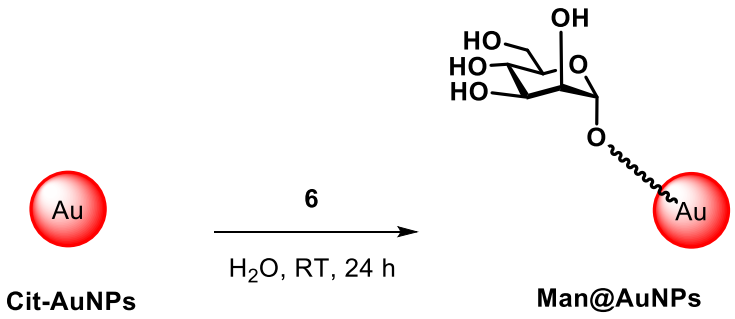


An aqueous solution of **Cit-AuNPs** (135 µmol, 2 mL) was mixed with compound **6** (0.2 mg, 0.3 µmol) in water and allowed to stir for 24 h at room temperature. The **Man@AuNPs** were then dialyzed against 1.5 L MilliQ water three times.

**Galactose functionalized gold nanoparticles (Gal@AuNPs)**

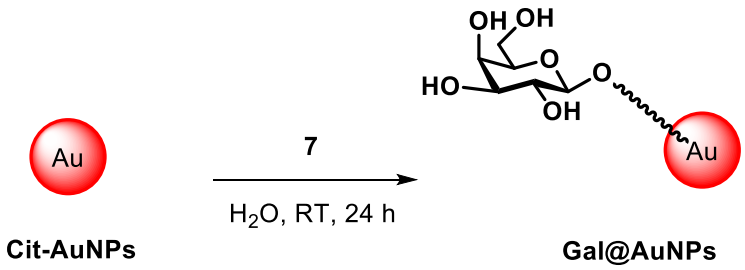


An aqueous solution of **Cit-AuNPs** (135 µmol, 2 mL) was mixed with compound **7** (0.2 mg, 0.3 µmol) in water and allowed to stir for 24 h at room temperature. The **Gal@AuNPs** were then dialyzed against 1.5 L MilliQ water three times.

**Di-mannose functionalized gold nanoparticles (DiMan@AuNPs)**

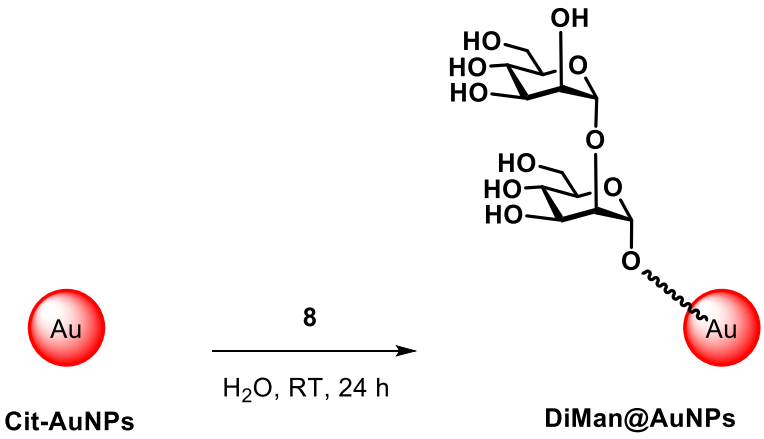


An aqueous solution of **Cit-AuNPs** (135 µmol, 2 mL) was mixed with compound **8** (0.3 mg, 0.3 µmol) in water and allowed to stir for 24 h at room temperature. The Di**Man@AuNPs** were then dialyzed against 1.5 L MilliQ water three times.

**Carbohydrate quantification on nanoparticles**

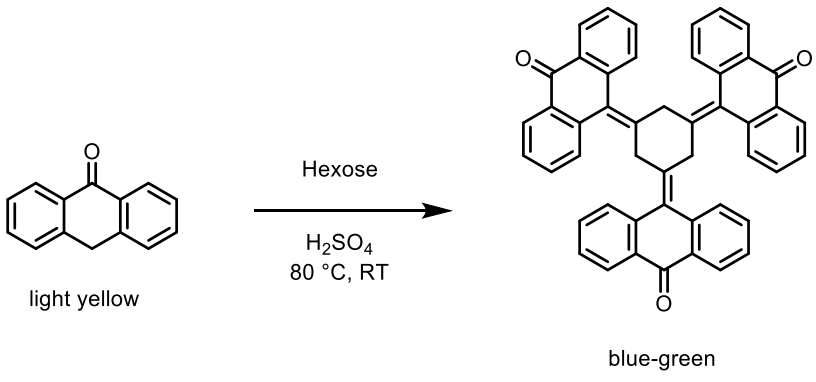

A freshly prepared solution of anthrone (0.5%, w/w) in sulfuric acid was added slowly to 0.5 mL the stock solutions or the nanoparticle samples. The resulting solution was gently mixed and heated to 80 ºC for 10 min. The absorption was recorded at 620 nm to make the calibration curve and interpolation of the samples.

# 6. Conclusions and perspectives

In this dissertation, a different method to obtain ultrasmall gold nanoparticles (2 nm) using a thio-glycoside as a reducing and stabilizing agent was developed. These nanoparticles were tested in biological media and showed high biocompatibility both *in vitro* and *in vivo*. Due to the surface chemistry of the protozoan parasites *Plasmodium falciparum* and *Toxoplasma gondii*, gold nanoparticles were used for binding studies, as the cysteine-rich domains present on the surface proteins of these protozoan parasites were targeted, through the well-known thiol-gold linkage. The high binding efficiency of gold nanoparticles to all of the blood stages of *P. falciparum*, as well as extracellular and intracellular *T. gondii*, shows promising applications for drug delivery discoveries. Drug conjugation was carried out for *in vitro* and *in vivo* inhibition studies by comparing the therapeutic activity of drug-loaded nanoparticles to same concentration of free drug. Targeted delivery can reduce the drug dosage needed, which reduces drug resistance that is a major problem in the treatment of parasite-related diseases. In order to prove that the binding of gold nanoparticles to the protozoan parasites occurs through cysteine-rich domains, cysteine blocking experiments can be further carried out to protect the thiol group and avoid conjugation to gold. To enhance the targeting efficiency for further therapeutic studies, especially in intracellular *T. gondii*, single domain antibodies can be conjugated to the gold nanoparticles. These types of antibodies exhibit better stability, functionality, epitope binding and therapeutic applications compared to conventional antibodies. The conjugation of single domain antibodies, for targeting and for a certain therapeutic activity, to nanoparticles can provide a multimodal nanoparticle for theranostics of parasitic infectious diseases. The application of these multimodal nanoparticles can be further extended to other targeting diseases such as cancer.

Mesoporous silica nanoparticles have been used in cancer drug delivery due to the mesoporous framework that can capture and release cargo. Flat discs were synthesized to increase the surface contact with the cells. This novel shape showed improved cellular uptake compared to conventional spherical mesoporous silica nanoparticles. The silica

nanodiscs were doped with different percentages of cleavable moieties within the framework in order to hold the cargo until the particles are internalized by the cells. The doped particles showed a more controlled release of the cargo compared to non-doped particles, which is an important feature in order to avoid nonspecific release of drugs. The particles underwent classical endocytosis through endosomes and the silica debris underwent exocytosis once the particles were degraded. A study on the breakability of the particles showed that the higher the percentage of cleavable bonds, the higher the hydrophobicity of the particles. Nevertheless, without the introduction of cleavable bonds that would selectively break the particles only once they are internalized, cargo release would occur dependent on time and not location. Therefore, introduction of carbohydrates as cleavable moieties would solve the problem of hydrophobicity and also provide responsiveness under certain conditions (such as a specific pH, or the presence of enzymes).

For targeted drug delivery, it is important to introduce available targeting biomolecules that could bind overexpressed receptors on targeted cells. Functionalization of breakable nanodiscs with carbohydrates could provide a fully engineered responsive nanocarrier that would be taken up only by the targeted cells and ensure the cargo release only upon particle internalization. This allows for using a lower dosage of drug, as the therapeutic activity is localized, which results in decreased side effects.

The use of glycosylated nanoparticles for targeting and binding studies was further assessed. Ultrasmall fluorescent silicon nanoparticles were functionalized with a glucoside to facilitate the blood brain barrier crossing. The glucose-functionalized nanoparticles containing a radiotracer are being tested *in vivo*. The possibility to enable the blood brain barrier crossing will open up opportunities for targeted delivery of common brain diseases such as brain tumors or Alzheimer's disease, and also severe brain infections such as cerebral malaria or toxoplasmosis.

Carbohydrate-protein interactions occur through a certain carbohydrate epitope. Knowing the smallest epitope that is able to effect an interaction with proteins in high affinity is important to understand these processes and to build up nanotechnology tools. For this purpose, different glycosylated plasmonic nanoparticles were synthesized in order to analyze carbohydrate-protein interactions between green microalgae and cyanobacteria.

Further studies on this topic will give information on biological processes that are still unknown due to the structural complexity.

# 7. References


1. Tay, C. Y.; Setyawati, M. I.; Xie, J.; Parak, W. J.; Leong, D. T. Back to Basics: Exploiting the Innate Physico-Chemical Characteristics of Nanomaterials for Biomedical Applications. *Adv. Funct. Mater.* **2014,** *24*, 5936-5955.

2. Katz, E.; Willner, I. Integrated Nanoparticle–Biomolecule Hybrid Systems: Synthesis, Properties, and Applications. *Angew. Chem. Int. Ed.* **2004,** *43*, 6042-6108.

3. Roduner, E. Size Matters: Why Nanomaterials Are Different. *Chem. Soc. Rev.* **2006,** *35*, 583-592.

4. Volokitin, Y.; Sinzig, J.; de Jongh, L. J.; Schmid, G.; Vargaftik, M. N.; Moiseevi, I. I. Quantum-Size Effects in the Thermodynamic Properties of Metallic Nanoparticles. *Nature* **1996,** *384*, 621.

5. Zarschler, K.; Rocks, L.; Licciardello, N.; Boselli, L.; Polo, E.; Garcia, K. P.; De Cola, L.; Stephan, H.; Dawson, K. A. Ultrasmall Inorganic Nanoparticles: State-of-the-Art and Perspectives for Biomedical Applications. *Nanomedicine: NBM* **2016,** *12*, 1663-1701.

6. Longmire, M.; Choyke, P. L.; Kobayashi, H. Clearance Properties of Nano-Sized Particles and Molecules as Imaging Agents: Considerations and Caveats. *Nanomedicine* **2008,** *3*, 703-717.

7. Lin, Z.; Monteiro-Riviere, N. A.; Riviere, J. E. Pharmacokinetics of Metallic Nanoparticles. *Wiley Interdiscip. Rev. Nanomed. Nanobiotechnol.* **2015,** *7*, 189-217.

8. Boisselier, E.; Astruc, D. Gold Nanoparticles in Nanomedicine: Preparations, Imaging, Diagnostics, Therapies and Toxicity. *Chem. Soc. Rev.* **2009,** *38*, 1759-1782.

9. Rai, M.; Yadav, A.; Gade, A. Silver Nanoparticles as a New Generation of Antimicrobials. *Biotechnol. Adv.* **2009,** *27*, 76-83.

10. Li, Z.; Barnes, J. C.; Bosoy, A.; Stoddart, J. F.; Zink, J. I. Mesoporous Silica Nanoparticles in Biomedical Applications. *Chem. Soc. Rev.* **2012,** *41*, 2590-2605.

11. Park, J.-H.; Gu, L.; von Maltzahn, G.; Ruoslahti, E.; Bhatia, S. N.; Sailor, M. J. Biodegradable Luminescent Porous Silicon Nanoparticles for in Vivo Applications. *Nat. Mater.* **2009,** *8*, 331.

12. Kostarelos, K.; Bianco, A.; Prato, M. Promises, Facts and Challenges for Carbon Nanotubes in Imaging and Therapeutics. *Nat. Nanotechnol.* **2009,** *4*, 627.

13. Dellinger, A.; Zhou, Z.; Connor, J.; Madhankumar, A. B.; Pamujula, S.; Sayes, C. M.; Kepley, C. L. Application of Fullerenes in Nanomedicine: An Update. *Nanomedicine* **2013,** *8*, 1191-1208.

14. Mao, H. Y.; Laurent, S.; Chen, W.; Akhavan, O.; Imani, M.; Ashkarran, A. A.; Mahmoudi, M. Graphene: Promises, Facts, Opportunities, and Challenges in Nanomedicine. *Chem. Rev.* **2013,** *113*, 3407-3424.

15. Elsabahy, M.; Wooley, K. L. Design of Polymeric Nanoparticles for Biomedical Delivery Applications. *Chem. Soc. Rev.* **2012,** *41*, 2545-2561.

16. Mintzer, M. A.; Grinstaff, M. W. Biomedical Applications of Dendrimers: A Tutorial. *Chem. Soc. Rev.* **2011,** *40*, 173-190.

17. Reddy, L. H.; Arias, J. L.; Nicolas, J.; Couvreur, P. Magnetic Nanoparticles: Design and Characterization, Toxicity and Biocompatibility, Pharmaceutical and Biomedical Applications. *Chem. Rev.* **2012,** *112*, 5818-5878.

18. Klostranec, J. M.; Chan, W. C. W. Quantum Dots in Biological and Biomedical Research: Recent Progress and Present Challenges. *Adv. Mater.* **2006,** *18*, 1953-1964.

19. Daniel, M.-C.; Astruc, D. Gold Nanoparticles: Assembly, Supramolecular Chemistry, Quantum-Size-Related Properties, and Applications toward Biology, Catalysis, and Nanotechnology. *Chem. Rev.* **2004,** *104*, 293-346.

20. Liz-Marzán, L. M. Nanometals: Formation and Color. *Mater. Today* **2004,** *7*, 26-31.

21. Yeh, Y.-C.; Creran, B.; Rotello, V. M. Gold Nanoparticles: Preparation, Properties, and Applications in Bionanotechnology. *Nanoscale* **2012,** *4*, 1871-1880.

22. Delbianco, M.; Bharate, P.; Varela-Aramburu, S.; Seeberger, P. H. Carbohydrates in Supramolecular Chemistry. *Chem. Rev.* **2016,** *116*, 1693-1752.

23. Dreaden, E. C.; Alkilany, A. M.; Huang, X.; Murphy, C. J.; El-Sayed, M. A. The Golden Age: Gold Nanoparticles for Biomedicine. *Chem. Soc. Rev.* **2012,** *41*, 2740-2779.

24. Richards, S.-J.; Otten, L.; Gibson, M. I. Glycosylated Gold Nanoparticle Libraries for Label-Free Multiplexed Lectin Biosensing *J. Mater. Chem. B* **2016,** *4*, 3046-3053.

25. Sardar, R.; Shumaker-Parry, J. S. Spectroscopic and Microscopic Investigation of Gold Nanoparticle Formation: Ligand and Temperature Effects on Rate and Particle Size. *J. Am. Chem. Soc.* **2011,** *133*, 8179-8190.

26. Hussain, I.; Graham, S.; Wang, Z.; Tan, B.; Sherrington, D. C.; Rannard, S. P.; Cooper, A. I.; Brust, M. Size-Controlled Synthesis of near-Monodisperse Gold Nanoparticles in the 1−4 Nm Range Using Polymeric Stabilizers. *J. Am. Chem. Soc.* **2005,** *127*, 16398-16399.

27. Jana, N. R.; Gearheart, L.; Murphy, C. J. Seeding Growth for Size Control of 5−40 Nm Diameter Gold Nanoparticles. *Langmuir* **2001,** *17*, 6782-6786.

28. Grzelczak, M.; Perez-Juste, J.; Mulvaney, P.; Liz-Marzan, L. M. Shape Control in Gold Nanoparticle Synthesis. *Chem. Soc. Rev.* **2008,** *37*, 1783-1791.

29. Riley, R. S.; Day, E. S. Gold Nanoparticle-Mediated Photothermal Therapy: Applications and Opportunities for Multimodal Cancer Treatment. *Wiley Interdiscip. Rev. Nanomed. Nanobiotechnol.* **2017,** *9*.

30. Weissleder, R. A Clearer Vision for in Vivo Imaging. *Nat. Biotechnol.* **2001,** *19*, 316.

31. Morton, J. G.; Day, E. S.; Halas, N. J.; West, J. L., Nanoshells for Photothermal Cancer Therapy. In *Cancer Nanotechnology: Methods and Protocols*, Grobmyer, S. R.; Moudgil, B. M., Eds. Humana Press: Totowa, NJ, **2010**, pp 101-117.

32. Huang, X.; El-Sayed, I. H.; El-Sayed, M. A., Applications of Gold Nanorods for Cancer Imaging and Photothermal Therapy. In *Cancer Nanotechnology: Methods and Protocols*, Grobmyer, S. R.; Moudgil, B. M., Eds. Humana Press: Totowa, NJ, **2010**, pp 343-357.

33. Cobley, C. M.; Au, L.; Chen, J.; Xia, Y. Targeting Gold Nanocages to Cancer Cells for Photothermal Destruction and Drug Delivery. *Expert Opin. Drug Deliv.* **2010,** *7*, 577-587.

34. Wang, X.; Li, G.; Ding, Y.; Sun, S. Understanding the Photothermal Effect of Gold Nanostars and Nanorods for Biomedical Applications. *RSC Adv.* **2014,** *4*, 30375-30383.

35. Templeton, A. C.; Wuelfing, W. P.; Murray, R. W. Monolayer-Protected Cluster Molecules. *Acc. Chem. Res.* **2000,** *33*, 27-36.

36. Varela-Aramburu, S.; Wirth, R.; Lai, C.-H.; Orts-Gil, G.; Seeberger, P. H. Straightforward and Robust Synthesis of Monodisperse Surface-Functionalized Gold Nanoclusters. *Beilstein J. Nanotechnol.* **2016,** *7*, 1278-1283.

37. Drechsler, U.; Fischer, N. O.; Frankamp, B. L.; Rotello, V. M. Highly Efficient Biocatalysts Via Covalent Immobilization of Candida Rugosa Lipase on Ethylene Glycol-Modified Gold–Silica Nanocomposites. *Adv. Mater.* **2004,** *16*, 271-274.

38. Li, X.; Guo, J.; Asong, J.; Wolfert, M. A.; Boons, G.-J. Multifunctional Surface Modification of Gold-Stabilized Nanoparticles by Bioorthogonal Reactions. *J. Am. Chem. Soc.* **2011,** *133*, 11147-11153.

39. Jiang, X.; Housni, A.; Gody, G.; Boullanger, P.; Charreyre, M.-T.; Delair, T.; Narain, R. Synthesis of Biotinylated A-D-Mannoside or N-Acetyl B-D-Glucosaminoside Decorated Gold Nanoparticles: Study of Their Biomolecular Recognition with Con a and Wga Lectins. *Bioconjugate Chem.* **2010,** *21*, 521-530.

40. Ghosh, P.; Yang, X.; Arvizo, R.; Zhu, Z.-J.; Agasti, S. S.; Mo, Z.; Rotello, V. M. Intracellular Delivery of a Membrane-Impermeable Enzyme in Active Form Using Functionalized Gold Nanoparticles. *J. Am. Chem. Soc.* **2010,** *132*, 2642-2645.

41. Cárdenas, M.; Barauskas, J.; Schillén, K.; Brennan, J. L.; Brust, M.; Nylander, T. Thiol-Specific and Nonspecific Interactions between DNA and Gold Nanoparticles. *Langmuir* **2006,** *22*, 3294-3299.

42. Liberman, A.; Mendez, N.; Trogler, W. C.; Kummel, A. C. Synthesis and Surface Functionalization of Silica Nanoparticles for Nanomedicine. *Surf. Sci. Rep.* **2014,** *69*, 132-158.

43. Wang, Y.; Zhao, Q.; Han, N.; Bai, L.; Li, J.; Liu, J.; Che, E.; Hu, L.; Zhang, Q.; Jiang, T.; Wang, S. Mesoporous Silica Nanoparticles in Drug Delivery and Biomedical Applications. *Nanomedicine* **2015,** *11*, 313-327.

44. Stöber, W.; Fink, A.; Bohn, E. Controlled Growth of Monodisperse Silica Spheres in the Micron Size Range. *J. Colloid Interface Sci.* **1968,** *26*, 62-69.

45. Caruso, F.; Caruso, R. A.; Möhwald, H. Nanoengineering of Inorganic and Hybrid Hollow Spheres by Colloidal Templating. *Science* **1998,** *282*, 1111-1114.

46. Bharti, C.; Nagaich, U.; Pal, A. K.; Gulati, N. Mesoporous Silica Nanoparticles in Target Drug Delivery System: A Review. *Int. J. Pharma. Investig.* **2015,** *5*, 124-133.

47. Tang, F.; Li, L.; Chen, D. Mesoporous Silica Nanoparticles: Synthesis, Biocompatibility and Drug Delivery. *Adv. Mater.* **2012,** *24*, 1504-1534.

48. Koenderink, G. H.; Sacanna, S.; Pathmamanoharan, C.; Raşa, M.; Philipse, A. P. Preparation and Properties of Optically Transparent Aqueous Dispersions of Monodisperse Fluorinated Colloids. *Langmuir* **2001,** *17*, 6086-6093.

49. Viarbitskaya, S.; Ryderfors, L.; Mikaelsson, T.; Mukhtar, E.; Johansson, L. B. Å. Luminescence Enhancement from Silica-Coated Gold Nanoparticle Agglomerates Following Multi-Photon Excitation. *J. Fluoresc.* **2011,** *21*, 257-264.

50. Lee, K.; Moon, H.-Y.; Park, C.; Kim, O. R.; Ahn, E.; Lee, S. Y.; Park, H. E.; Ihm, S.-H.; Seung, K.-B.; Chang, K.; Yoon, T.-J.; Lee, C.; Cheong, C.; Hong, K. S. Magnetic Resonance Imaging of Macrophage Activity in Atherosclerotic Plaques of Apolipoprotein E-Deficient Mice by Using Polyethylene Glycolated Magnetic Fluorescent Silica-Coated Nanoparticles. *Curr. Appl. Phys.* **2009,** *9*, S15-S18.

51. Yuan, J.; Zhou, S.; Gu, G.; Wu, L. Encapsulation of Organic Pigment Particles with Silica Via Sol-Gel Process. *J. Sol-Gel Sci. Technol.* **2005,** *36*, 265-274.

52. Hagura, N.; Ogi, T.; Shirahama, T.; Iskandar, F.; Okuyama, K. Highly Luminescent Silica-Coated Zno Nanoparticles Dispersed in an Aqueous Medium. *J. Lumin.* **2011,** *131*, 921-925.

53. O'Farrell, N.; Houlton, A.; Horrocks, B. R. Silicon Nanoparticles: Applications in Cell Biology and Medicine. *Int. J. Nanomed.* **2006,** *1*, 451-472.

54. Rosso-Vasic, M.; Spruijt, E.; van Lagen, B.; De Cola, L.; Zuilhof, H. Alkyl-Functionalized Oxide-Free Silicon Nanoparticles: Synthesis and Optical Properties. *Small* **2008,** *4*, 1835-1841.

55. Lai, C.-H.; Hütter, J.; Hsu, C.-W.; Tanaka, H.; Varela-Aramburu, S.; De Cola, L.; Lepenies, B.; Seeberger, P. H. Analysis of Carbohydrate–Carbohydrate Interactions Using

Sugar-Functionalized Silicon Nanoparticles for Cell Imaging. *Nano Lett.* **2016,** *16*, 807-811.

56. Cha, C.; Shin, S. R.; Annabi, N.; Dokmeci, M. R.; Khademhosseini, A. Carbon-Based Nanomaterials: Multifunctional Materials for Biomedical Engineering. *ACS Nano* **2013,** *7*, 2891-2897.

57. Bianco, A.; Kostarelos, K.; Partidos, C. D.; Prato, M. Biomedical Applications of Functionalised Carbon Nanotubes. *Chem. Commun.* **2005**, 571-577.

58. Alshehri, R.; Ilyas, A. M.; Hasan, A.; Arnaout, A.; Ahmed, F.; Memic, A. Carbon Nanotubes in Biomedical Applications: Factors, Mechanisms, and Remedies of Toxicity. *J. Med. Chem.* **2016,** *59*, 8149-8167.

59. Bianco, A.; Kostarelos, K.; Prato, M. Applications of Carbon Nanotubes in Drug Delivery. *Curr. Opin. Chem. Biol.* **2005,** *9*, 674-679.

60. Kroto, H. W.; Heath, J. R.; O'Brien, S. C.; Curl, R. F.; Smalley, R. E. C60: Buckminsterfullerene. *Nature* **1985,** *318*, 162.

61. Partha, R.; Conyers, J. L. Biomedical Applications of Functionalized Fullerene-Based Nanomaterials. *Int. J. Nanomed.* **2009,** *4*, 261-275.

62. Montellano, A.; Da Ros, T.; Bianco, A.; Prato, M. Fullerene C60 as a Multifunctional System for Drug and Gene Delivery. *Nanoscale* **2011,** *3*, 4035-4041.

63. Zhang, Y.; Nayak, T. R.; Hong, H.; Cai, W. Graphene: A Versatile Nanoplatform for Biomedical Applications. *Nanoscale* **2012,** *4*, 3833-3842.

64. Yang, Y.; Asiri, A. M.; Tang, Z.; Du, D.; Lin, Y. Graphene Based Materials for Biomedical Applications. *Mater. Today* **2013,** *16*, 365-373.

65. Goenka, S.; Sant, V.; Sant, S. Graphene-Based Nanomaterials for Drug Delivery and Tissue Engineering. *J. Controlled Release* **2014,** *173*, 75-88.

66. Alarcon, C. d. l. H.; Pennadam, S.; Alexander, C. Stimuli Responsive Polymers for Biomedical Applications. *Chem. Soc. Rev.* **2005,** *34*, 276-285.

67. Lee, C. C.; MacKay, J. A.; Fréchet, J. M. J.; Szoka, F. C. Designing Dendrimers for Biological Applications. *Nat. Biotechnol.* **2005,** *23*, 1517.

68. Laurent, S.; Forge, D.; Port, M.; Roch, A.; Robic, C.; Vander Elst, L.; Muller, R. N. Magnetic Iron Oxide Nanoparticles: Synthesis, Stabilization, Vectorization, Physicochemical Characterizations, and Biological Applications. *Chem. Rev.* **2008,** *108*, 2064-2110.

69. Lu, A.-H.; Salabas, E. L.; Schüth, F. Magnetic Nanoparticles: Synthesis, Protection, Functionalization, and Application. *Angew. Chem. Int. Ed.* **2007,** *46*, 1222-1244.

70. Gupta, A. K.; Gupta, M. Synthesis and Surface Engineering of Iron Oxide Nanoparticles for Biomedical Applications. *Biomaterials* **2005,** *26*, 3995-4021.

71. Medintz, I. L.; Uyeda, H. T.; Goldman, E. R.; Mattoussi, H. Quantum Dot Bioconjugates for Imaging, Labelling and Sensing. *Nat. Mater.* **2005,** *4*, 435.

72. de la Fuente, J. M.; Penadés, S. Glyconanoparticles: Types, Synthesis and Applications in Glycoscience, Biomedicine and Material Science. *Biochim. Biophys. Acta* **2006,** *1760*, 636-651.

73. Cho, E. J.; Holback, H.; Liu, K. C.; Abouelmagd, S. A.; Park, J.; Yeo, Y. Nanoparticle Characterization: State of the Art, Challenges, and Emerging Technologies. *Mol. Pharm.* **2013,** *10*, 2093-2110.

74. Li, T.; Senesi, A. J.; Lee, B. Small Angle X-Ray Scattering for Nanoparticle Research. *Chem. Rev.* **2016,** *116*, 11128-11180.

75. Brian Richard, P. Everything Saxs: Small-Angle Scattering Pattern Collection and Correction. *J. Phys.: Condens. Matter* **2013,** *25*, 383201.

76. Lin, P.-C.; Lin, S.; Wang, P. C.; Sridhar, R. Techniques for Physicochemical Characterization of Nanomaterials. *Biotechnol. Adv.* **2014,** *32*, 711-726.

77. Tiede, K.; Boxall, A. B. A.; Tear, S. P.; Lewis, J.; David, H.; Hassellöv, M. Detection and Characterization of Engineered Nanoparticles in Food and the Environment. *Food Addit. Contam.* **2008,** *25*, 795-821.

78. Williams, D. B.; Carter, C. B., *Transmission Electron Microscopy*. Springer: Boston, **1996**.

79. Hall, J. B.; Dobrovolskaia, M. A.; Patri, A. K.; McNeil, S. E. Characterization of Nanoparticles for Therapeutics. *Nanomedicine* **2007,** *2*, 789-803.

80. Bogner, A.; Thollet, G.; Basset, D.; Jouneau, P. H.; Gauthier, C. Wet Stem: A New Development in Environmental Sem for Imaging Nano-Objects Included in a Liquid Phase. *Ultramicroscopy* **2005,** *104*, 290-301.

81. Bai, X.-c.; McMullan, G.; Scheres, S. H. W. How Cryo-Em Is Revolutionizing Structural Biology. *Trends Biochem. Sci* **2015,** *40*, 49-57.

82. Hong, R.; Fischer, N. O.; Verma, A.; Goodman, C. M.; Emrick, T.; Rotello, V. M. Control of Protein Structure and Function through Surface Recognition by Tailored Nanoparticle Scaffolds. *J. Am. Chem. Soc.* **2004,** *126*, 739-743.

83. Zhang, B.; Yan, B. Analytical Strategies for Characterizing the Surface Chemistry of Nanoparticles. *Anal. Bioanal. Chem.* **2010,** *396*, 973-982.

84. Murakami, Y.; Konishi, K. Remarkable Co-Catalyst Effect of Gold Nanoclusters on Olefin Oxidation Catalyzed by a Manganese−Porphyrin Complex. *J. Am. Chem. Soc.* **2007,** *129*, 14401-14407.

85. Gibson, J. D.; Khanal, B. P.; Zubarev, E. R. Paclitaxel-Functionalized Gold Nanoparticles. *J. Am. Chem. Soc.* **2007,** *129*, 11653-11661.

86. Du, F.; Zhang, B.; Zhou, H.; Yan, B.; Chen, L. Structure Elucidation of Nanoparticle-Bound Organic Molecules by 1h Nmr. *TrAC, Trends Anal. Chem.* **2009,** *28*, 88-95.

87. Learn Xps. https://xpssimplified.com/whatisxps.php.

88. Brown, M.; Wittwer, C. Flow Cytometry: Principles and Clinical Applications in Hematology. *Clin. Chem.* **2000,** *46*, 1221-1229.

89. Haag, R. Multivalency as a Chemical Organization and Action Principle. *Beilstein J. Org. Chem.* **2015,** *11*, 848-849.

90. Fasting, C.; Schalley, C. A.; Weber, M.; Seitz, O.; Hecht, S.; Koksch, B.; Dernedde, J.; Graf, C.; Knapp, E.-W.; Haag, R. Multivalency as a Chemical Organization and Action Principle. *Angew. Chem. Int. Ed.* **2012,** *51*, 10472-10498.

91. Varki, A.; Cummings, R. D.; Esko, J. D.; Freeze, H. H.; Stanley, P.; Bertozzi, C. R.; Hart, G. W.; Extler, M. E., *Essentials of Glycobiology*. 2nd ed.; Cold Spring Harbor Laboratory Press: New York, **2009**.

92. Muller, C.; Despras, G.; Lindhorst, T. K. Organizing Multivalency in Carbohydrate Recognition. *Chem. Soc. Rev.* **2016,** *45*, 3275-3302.

93. Ebong, E. E.; Macaluso, F. P.; Spray, D. C.; Tarbell, J. M. Imaging the Endothelial Glycocalyx in Vitro by Rapid Freezing/Freeze Substitution Transmission Electron Microscopy. *Arterioscler., Thromb., Vasc. Biol.* **2011,** *31*, 1908-1915.

94. Lee, Y. C.; Lee, R. T. Carbohydrate-Protein Interactions: Basis of Glycobiology. *Acc. Chem. Res.* **1995,** *28*, 321-327.

95. Lahmann, M., Architectures of Multivalent Glycomimetics for Probing Carbohydrate–Lectin Interactions. In *Glycoscience and Microbial Adhesion*, Lindhorst, T. K.; Oscarson, S., Eds. Springer Berlin Heidelberg: Berlin, Heidelberg, **2009**, pp 183-165.

96. Jimenez Blanco, J. L.; Ortiz Mellet, C.; Garcia Fernandez, J. M. Multivalency in Heterogeneous Glycoenvironments: Hetero-Glycoclusters, -Glycopolymers and -Glycoassemblies. *Chem. Soc. Rev.* **2013,** *42*, 4518-4531.

97. Chabre, Y. M.; Roy, R. Multivalent Glycoconjugate Syntheses and Applications Using Aromatic Scaffolds. *Chem. Soc. Rev.* **2013,** *42*, 4657-4708.

98. Lundquist, J. J.; Toone, E. J. The Cluster Glycoside Effect. *Chem. Rev.* **2002,** *102*, 555-578.

99. Fulton, D. A.; Stoddart, J. F. Neoglycoconjugates Based on Cyclodextrins and Calixarenes. *Bioconjugate Chem.* **2001,** *12*, 655-672.

100. Sansone, F.; Casnati, A. Multivalent Glycocalixarenes for Recognition of Biological Macromolecules: Glycocalyx Mimics Capable of Multitasking. *Chem. Soc. Rev.* **2013,** *42*, 4623-4639.

101. Roy, R.; Shiao, T. C.; Rittenhouse-Olson, K. Glycodendrimers: Versatile Tools for Nanotechnology. *Braz. J. Pharm. Sci.* **2013,** *49*, 85-108.

102. Marradi, M.; Chiodo, F.; Garcia, I.; Penades, S. Glyconanoparticles as Multifunctional and Multimodal Carbohydrate Systems. *Chem. Soc. Rev.* **2013,** *42*, 4728-4745.

103. Kiessling, L. L.; Grim, J. C. Glycopolymer Probes of Signal Transduction. *Chem. Soc. Rev.* **2013,** *42*, 4476-4491.

104. Bao, G.; Mitragotri, S.; Tong, S. Multifunctional Nanoparticles for Drug Delivery and Molecular Imaging. *Annu. Rev. Biomed. Eng.* **2013,** *15*, 253-282.

105. Euliss, L. E.; DuPont, J. A.; Gratton, S.; DeSimone, J. Imparting Size, Shape, and Composition Control of Materials for Nanomedicine. *Chem. Soc. Rev.* **2006,** *35*, 1095-1104.

106. Greish, K. Enhanced Permeability and Retention of Macromolecular Drugs in Solid Tumors: A Royal Gate for Targeted Anticancer Nanomedicines. *J. Drug Targeting* **2007,** *15*, 457-464.

107. Kottari, N.; Chabre, Y. M.; Sharma, R.; Roy, R., Applications of Glyconanoparticles as "Sweet" Glycobiological Therapeutics and Diagnostics. In *Multifaceted Development and Application of Biopolymers for Biology, Biomedicine and Nanotechnology*, Dutta, P. K.; Dutta, J., Eds. Springer Berlin Heidelberg: Berlin, Heidelberg, **2013**, pp 297-341.

108. Chen, X.; Ramström, O.; Yan, M. Glyconanomaterials: Emerging Applications in Biomedical Research. *Nano Research* **2014,** *7*, 1381-1403.

109. Eggeling, C.; Widengren, J.; Rigler, R.; Seidel, C. A. M. Photobleaching of Fluorescent Dyes under Conditions Used for Single-Molecule Detection: Evidence of Two-Step Photolysis. *Anal. Chem.* **1998,** *70*, 2651-2659.

110. Yan, J.; Estévez, M. C.; Smith, J. E.; Wang, K.; He, X.; Wang, L.; Tan, W. Dye-Doped Nanoparticles for Bioanalysis. *Nano Today* **2007,** *2*, 44-50.

111. Wang, X.; Ramstrom, O.; Yan, M. Dye-Doped Silica Nanoparticles as Efficient Labels for Glycans. *Chem. Commun.* **2011,** *47*, 4261-4263.

112. Qi, Z.; Bharate, P.; Lai, C.-H.; Ziem, B.; Böttcher, C.; Schulz, A.; Beckert, F.; Hatting, B.; Mülhaupt, R.; Seeberger, P. H.; Haag, R. Multivalency at Interfaces: Supramolecular Carbohydrate-Functionalized Graphene Derivatives for Bacterial Capture, Release, and Disinfection. *Nano Lett.* **2015,** *15*, 6051-6057.

113. Farr, T. D.; Lai, C.-H.; Grünstein, D.; Orts-Gil, G.; Wang, C.-C.; Boehm-Sturm, P.; Seeberger, P. H.; Harms, C. Imaging Early Endothelial Inflammation Following Stroke by Core Shell Silica Superparamagnetic Glyconanoparticles That Target Selectin. *Nano Lett.* **2014,** *14*, 2130-2134.

114. Slowing, I. I.; Vivero-Escoto, J. L.; Wu, C.-W.; Lin, V. S. Y. Mesoporous Silica Nanoparticles as Controlled Release Drug Delivery and Gene Transfection Carriers. *Adv. Drug Delivery Rev.* **2008,** *60*, 1278-1288.

115. Torchilin, V. P. Drug Targeting. *Eur. J. Pharm. Sci.* **2000,** *11*, S81-S91.

116. Bae, Y. H.; Park, K. Targeted Drug Delivery to Tumors: Myths, Reality and Possibility. *J. Controlled Release* **2011,** *153*, 198-205.

117. Irache, J. M.; Salman, H. H.; Gamazo, C.; Espuelas, S. Mannose-Targeted Systems for the Delivery of Therapeutics. *Expert Opin. Drug Deliv.* **2008,** *5*, 703-724.

118. Lai, C.-H.; Lin, C.-Y.; Wu, H.-T.; Chan, H.-S.; Chuang, Y.-J.; Chen, C.-T.; Lin, C.-C. Galactose Encapsulated Multifunctional Nanoparticle for Hepg2 Cell Internalization. *Adv. Funct. Mater.* **2010,** *20*, 3948-3958.

119. Kaur, I. P.; Bhandari, R.; Bhandari, S.; Kakkar, V. Potential of Solid Lipid Nanoparticles in Brain Targeting. *J. Controlled Release* **2008,** *127*, 97-109.

120. Vannucci, S. J.; Maher, F.; Simpson, I. A. Glucose Transporter Proteins in Brain: Delivery of Glucose to Neurons and Glia. *Glia* **1997,** *21*, 2-21.

121. Jubeli, E.; Moine, L.; Vergnaud-Gauduchon, J.; Barratt, G. E-Selectin as a Target for Drug Delivery and Molecular Imaging. *J. Controlled Release* **2012,** *158*, 194-206.

122. Kneuer, C.; Ehrhardt, C.; Radomski, M. W.; Bakowsky, U. Selectins – Potential Pharmacological Targets? *Drug Discovery Today* **2006,** *11*, 1034-1040.

123. Iravani, S.; Korbekandi, H.; Mirmohammadi, S. V.; Zolfaghari, B. Synthesis of Silver Nanoparticles: Chemical, Physical and Biological Methods. *Res. Pharm. Sci.* **2014,** *9*, 385-406.

124. Hao, R.; Xing, R.; Xu, Z.; Hou, Y.; Gao, S.; Sun, S. Synthesis, Functionalization, and Biomedical Applications of Multifunctional Magnetic Nanoparticles. *Adv. Mater.* **2010,** *22*, 2729-2742.

125. Rao, J. P.; Geckeler, K. E. Polymer Nanoparticles: Preparation Techniques and Size-Control Parameters. *Prog. Polym. Sci.* **2011,** *36*, 887-913.

126. Shukla, R.; Bansal, V.; Chaudhary, M.; Basu, A.; Bhonde, R. R.; Sastry, M. Biocompatibility of Gold Nanoparticles and Their Endocytotic Fate inside the Cellular Compartment: A Microscopic Overview. *Langmuir* **2005,** *21*, 10644-10654.

127. Dykman, L.; Khlebtsov, N. Gold Nanoparticles in Biomedical Applications: Recent Advances and Perspectives. *Chem. Soc. Rev.* **2012,** *41*, 2256-2282.

128. Sperling, R. A.; Rivera Gil, P.; Zhang, F.; Zanella, M.; Parak, W. J. Biological Applications of Gold Nanoparticles. *Chem. Soc. Rev.* **2008,** *37*, 1896-1908.

129. Calzolai, L.; Franchini, F.; Gilliland, D.; Rossi, F. Protein−Nanoparticle Interaction: Identification of the Ubiquitin−Gold Nanoparticle Interaction Site. *Nano Lett.* **2010,** *10*, 3101-3105.

130. El-Sayed, I. H.; Huang, X.; El-Sayed, M. A. Selective Laser Photo-Thermal Therapy of Epithelial Carcinoma Using Anti-Egfr Antibody Conjugated Gold Nanoparticles. *Cancer Lett.* **2006,** *239*, 129-135.

131. Mirkin, C. A.; Letsinger, R. L.; Mucic, R. C.; Storhoff, J. J. A DNA-Based Method for Rationally Assembling Nanoparticles into Macroscopic Materials. *Nature* **1996,** *382*, 607-609.

132. Sherman, A. I.; Ter-Pogossian, M. Lymph-Node Concentration of Radioactive Colloidal Gold Following Interstitial Injection. *Cancer* **1953,** *6*, 1238-1240.

133. Brown, S. D.; Nativo, P.; Smith, J.-A.; Stirling, D.; Edwards, P. R.; Venugopal, B.; Flint, D. J.; Plumb, J. A.; Graham, D.; Wheate, N. J. Gold Nanoparticles for the Improved Anticancer Drug Delivery of the Active Component of Oxaliplatin. *J. Am. Chem. Soc.* **2010,** *132*, 4678-4684.

134. Liao, Y.-H.; Chang, Y.-J.; Yoshiike, Y.; Chang, Y.-C.; Chen, Y.-R. Negatively Charged Gold Nanoparticles Inhibit Alzheimer's Amyloid-B Fibrillization, Induce Fibril Dissociation, and Mitigate Neurotoxicity. *Small* **2012,** *8*, 3631-3639.

135. Turkevich, J.; Stevenson, P. C.; Hillier, J. A Study of the Nucleation and Growth Processes in the Synthesis of Colloidal Gold. *Disc. Faraday Soc.* **1951,** *11*, 55-75.

136. Brust, M.; Walker, M.; Bethell, D.; Schiffrin, D. J.; Whyman, R. Synthesis of Thiol-Derivatised Gold Nanoparticles in a Two-Phase Liquid-Liquid System. *Chem. Commun.* **1994**, 801-802.

137. Brust, M.; Fink, J.; Bethell, D.; Schiffrin, D. J.; Kiely, C. Synthesis and Reactions of Functionalised Gold Nanoparticles. *Chem. Commun.* **1995**, 1655-1656.

138. de la Fuente, J. M.; Barrientos, A. G.; Rojas, T. C.; Rojo, J.; Cañada, J.; Fernández, A.; Penadés, S. Gold Glyconanoparticles as Water-Soluble Polyvalent Models to Study Carbohydrate Interactions. *Angew. Chem. Int. Ed.* **2001,** *40*, 2257-2261.

139. Watanabe, S.; Yoshida, K.; Shinkawa, K.; Kumagawa, D.; Seguchi, H. Thioglucose-Stabilized Gold Nanoparticles as a Novel Platform for Colorimetric Bioassay Based on Nanoparticle Aggregation. *Colloids Surf., B* **2010,** *81*, 570-577.

140. Richards, S.-J.; Fullam, E.; Besra, G. S.; Gibson, M. I. Discrimination between Bacterial Phenotypes Using Glyco-Nanoparticles and the Impact of Polymer Coating on Detection Readouts. *J. Mater. Chem. B* **2014,** *2*, 1490-1498.

141. Kim, B. H.; Hackett, M. J.; Park, J.; Hyeon, T. Synthesis, Characterization, and Application of Ultrasmall Nanoparticles. *Chem. Mater.* **2014,** *26*, 59-71.

142. Zhu, M.; Lanni, E.; Garg, N.; Bier, M. E.; Jin, R. Kinetically Controlled, High-Yield Synthesis of Au25 Clusters. *J. Am. Chem. Soc.* **2008,** *130*, 1138-1139.

143. Wu, Z.; Suhan, J.; Jin, R. One-Pot Synthesis of Atomically Monodisperse, Thiol-Functionalized Au25 Nanoclusters. *J. Mater. Chem.* **2009,** *19*, 622-626.

144. Meng, X.; Liu, Z.; Zhu, M.; Jin, R. Controlled Reduction for Size Selective Synthesis of Thiolate-Protected Gold Nanoclusters Aun(N = 20, 24, 39, 40). *Nanoscale Res. Lett.* **2012,** *7*, 1-7.

145. Duff, D. G.; Baiker, A.; Edwards, P. P. A New Hydrosol of Gold Clusters. 1. Formation and Particle Size Variation. *Langmuir* **1993,** *9*, 2301-2309.

146. Sau, T. K.; Murphy, C. J. Room Temperature, High-Yield Synthesis of Multiple Shapes of Gold Nanoparticles in Aqueous Solution. *J. Am. Chem. Soc.* **2004,** *126*, 8648-8649.

147. Haiss, W.; Thanh, N. T. K.; Aveyard, J.; Fernig, D. G. Determination of Size and Concentration of Gold Nanoparticles from Uv−Vis Spectra. *Anal. Chem.* **2007,** *79*, 4215-4221.

148. Lin, C.-C.; Yeh, Y.-C.; Yang, C.-Y.; Chen, C.-L.; Chen, G.-F.; Chen, C.-C.; Wu, Y.-C. Selective Binding of Mannose-Encapsulated Gold Nanoparticles to Type 1 Pili in Escherichia Coli. *J. Am. Chem. Soc.* **2002,** *124*, 3508-3509.

149. Bowers, C. M.; Carlson, D. A.; Rivera, M.; Clark, R. L.; Toone, E. J. Effect of Compressive Force on Unbinding Specific Protein–Ligand Complexes with Force Spectroscopy. *J. Phys. Chem. B.* **2013,** *117*, 4755-4762.

150. Barltrop, J. A.; Owen, T. C.; Cory, A. H.; Cory, J. G. 5-(3-Carboxymethoxyphenyl)-2-(4,5-Dimethylthiazolyl)-3-(4-Sulfophenyl)Tetrazolium, Inner Salt (Mts) and Related Analogs of 3-(4,5-Dimethylthiazolyl)-2,5-Diphenyltetrazolium Bromide (Mtt) Reducing to Purple Water-Soluble Formazans as Cell-Viability Indicators. *Biorg. Med. Chem. Lett.* **1991,** *1*, 611-614.

151. Shokeen, M.; Anderson, C. J. Molecular Imaging of Cancer with Copper-64 Radiopharmaceuticals and Positron Emission Tomography (Pet). *Acc. Chem. Res.* **2009,** *42*, 832-841.

152. Campos-Martorell, M.; Cano-Sarabia, M.; Simats, A.; Hernández-Guillamon, M.; Rosell, A.; Maspoch, D.; Montaner, J. Charge Effect of a Liposomal Delivery System Encapsulating Simvastatin to Treat Experimental Ischemic Stroke in Rats. *Int. J. Nanomed.* **2016,** *11*, 3035-3048.

153. Pant, K.; Pufe, J.; Zarschler, K.; Bergmann, R.; Steinbach, J.; Reimann, S.; Haag, R.; Pietzsch, J.; Stephan, H. Surface Charge and Particle Size Determine the Metabolic Fate of Dendritic Polyglycerols. *Nanoscale* **2017,** *9*, 8723-8739.

154. Kadam, R. S.; Bourne, D. W. A.; Kompella, U. B. Nano-Advantage in Enhanced Drug Delivery with Biodegradable Nanoparticles: Contribution of Reduced Clearance. *Drug Metab. Dispos.* **2012,** *40*, 1380-1388.

155. World malaria report 2016 (World Health Organization, Geneva, op. 2016).

156. Cowman, A. F.; Crabb, B. S. Invasion of Red Blood Cells by Malaria Parasites. *Cell* **2006,** *124*, 755-766.

157. Pasvol, G. Protective Hemoglobinopathies and Plasmodium Falciparum Transmission. *Nat. Genet.* **2010,** *42*, 284.

158. Bannister, L.; Mitchell, G. The Ins, Outs and Roundabouts of Malaria. *Trends Parasitol.* **2003,** *19*, 209-213.

159. Josling, G. A.; Llinás, M. Sexual Development in Plasmodium Parasites: Knowing When It'S Time to Commit. *Nat. Rev. Microbiol.* **2015,** *13*, 573.

160. Dixon, M. W. A.; Thompson, J.; Gardiner, D. L.; Trenholme, K. R. Sex in Plasmodium: A Sign of Commitment. *Trends Parasitol.* **2008,** *24*, 168-175.

161. Killeen, G. F.; Seyoum, A.; Sikaala, C.; Zomboko, A. S.; Gimnig, J. E.; Govella, N. J.; White, M. T. Eliminating Malaria Vectors. *Parasit Vectors* **2013,** *6*, 172.

162. White, N. J. Qinghaosu (Artemisinin): The Price of Success. *Science* **2008,** *320*, 330-334.

163. Lévesque, F.; Seeberger, P. H. Continuous-Flow Synthesis of the Anti-Malaria Drug Artemisinin. *Angew. Chem. Int. Ed.* **2012,** *51*, 1706-1709.

164. Sanders, P. R.; Gilson, P. R.; Cantin, G. T.; Greenbaum, D. C.; Nebl, T.; Carucci, D. J.; McConville, M. J.; Schofield, L.; Hodder, A. N.; Yates, J. R.; Crabb, B. S. Distinct Protein Classes Including Novel Merozoite Surface Antigens in Raft-Like Membranes of Plasmodium Falciparum. *J. Biol. Chem.* **2005,** *280*, 40169-40176.

165. Volz, Jennifer C.; Yap, A.; Sisquella, X.; Thompson, Jenn K.; Lim, Nicholas T. Y.; Whitehead, Lachlan W.; Chen, L.; Lampe, M.; Tham, W.-H.; Wilson, D.; Nebl, T.; Marapana, D.; Triglia, T.; Wong, W.; Rogers, Kelly L.; Cowman, Alan F. Essential Role of the Pfrh5/Pfripr/Cyrpa Complex During Plasmodium Falciparum Invasion of Erythrocytes. *Cell Host Microbe* **2016,** *20*, 60-71.

166. Reddy, K. S.; Amlabu, E.; Pandey, A. K.; Mitra, P.; Chauhan, V. S.; Gaur, D. Multiprotein Complex between the Gpi-Anchored Cyrpa with Pfrh5 and Pfripr Is Crucial for Plasmodium Falciparum Erythrocyte Invasion. *Proc. Natl. Acad. Sci.* **2015,** *112*, 1179-1184.

167. van Dijk, M. R.; Janse, C. J.; Thompson, J.; Waters, A. P.; Braks, J. A. M.; Dodemont, H. J.; Stunnenberg, H. G.; van Gemert, G.-J.; Sauerwein, R. W.; Eling, W. A Central Role for P48/45 in Malaria Parasite Male Gamete Fertility. *Cell* **2001,** *104*, 153-164.

168. Ishino, T.; Chinzei, Y.; Yuda, M. Two Proteins with 6-Cys Motifs Are Required for Malarial Parasites to Commit to Infection of the Hepatocyte. *Mol. Microbiol.* **2005,** *58*, 1264-1275.

169. Häkkinen, H. The Gold–Sulfur Interface at the Nanoscale. *Nat. Chem.* **2012,** *4*, 443.

170. Fang, C.; Chungang, W.; Tingting, W.; Zhanfang, M.; Zhongmin, S. L-Cysteine Functionalized Gold Nanoparticles for the Colorimetric Detection of Hg 2+ Induced by Ultraviolet Light. *Nanotechnology* **2010,** *21*, 025501.

171. Connor, E. E.; Mwamuka, J.; Gole, A.; Murphy, C. J.; Wyatt, M. D. Gold Nanoparticles Are Taken up by Human Cells but Do Not Cause Acute Cytotoxicity. *Small* **2005,** *1*, 325-327.

172. Aryal, S.; B.K.C, R.; Dharmaraj, N.; Bhattarai, N.; Kim, C. H.; Kim, H. Y. Spectroscopic Identification of Sau Interaction in Cysteine Capped Gold Nanoparticles. *Spectrochim. Acta A* **2006,** *63*, 160-163.

173. Kuo, Y.-L.; Wang, S.-G.; Wu, C.-Y.; Lee, K.-C.; Jao, C.-J.; Chou, S.-H.; Chen, Y.-C. Functional Gold Nanoparticle-Based Antibacterial Agents for Nosocomial and Antibiotic-Resistant Bacteria. *Nanomedicine* **2016,** *11*, 2497-2510.

174. Watkins, W. M.; Mosobo, M. Treatment of <Em>Plasmodium Falciparum</Em> Malaria with Pyrimethamine-Sulfadoxine: Selective Pressure for Resistance Is a Function of Long Elimination Half-Life. *Trans. Royal Soc. Trop. Med. Hyg. 87*, 75-78.

175. Leport, C.; Raffi, F.; Matheron, S.; Katlama, C.; Regnier, B.; Saimot, A. G.; Marche, C.; Vedrenne, C.; Vilde, J. L. Treatment of Central Nervous System Toxoplasmosis with Pyrimethamine/Sulfadiazine Combination in 35 Patients with the Acquired Immunodeficiency Syndrome. *Am. J. Med. 84*, 94-100.

176. Lambros, C.; Vanderberg, J. P. Synchronization of Plasmodium Falciparum Erythrocytic Stages in Culture. *J. Parasitol.* **1979**, 418-420.

177. Susan E. Francis; David J. Sullivan, J., and; Goldberg, a. D. E. Hemoglobin Metabolism in the Malaria Parasite Plasmodium Falciparum. *Annu. Rev. Microbiol.* **1997,** *51*, 97-123.

178. Duffy, S.; Loganathan, S.; Holleran, J. P.; Avery, V. M. Large-Scale Production of Plasmodium Falciparum Gametocytes for Malaria Drug Discovery. *Nat. Protoc.* **2016,** *11*, 976.

179. Dubey, J. P.; Lindsay, D. S.; Speer, C. A. Structures of Toxoplasma Gondii Tachyzoites, Bradyzoites, and Sporozoites and Biology and Development of Tissue Cysts. *Clin. Microbiol. Rev.* **1998,** *11*, 267-299.

180. Pastoriza-Santos, I.; Liz-Marzán, L. M., Reliable Methods for Silica Coating of Au Nanoparticles. In *Nanomaterial Interfaces in Biology: Methods and Protocols*, Bergese, P.; Hamad-Schifferli, K., Eds. Humana Press: Totowa, NJ, **2013**, pp 75-93.

181. Radfar, A.; Méndez, D.; Moneriz, C.; Linares, M.; Marín-García, P.; Puyet, A.; Diez, A.; Bautista, J. M. Synchronous Culture of Plasmodium Falciparum at High Parasitemia Levels. *Nat. Protoc.* **2009,** *4*, 1899.

182. Giglio, V.; Varela-Aramburu, S.; Travaglini, L.; Fiorini, F.; Seeberger, P. H.; Maggini, L.; De Cola, L. Reshaping Silica Particles: Mesoporous Nanodiscs for Bimodal Delivery and Improved Cellular Uptake. *Chem. Eng. J.* **2018,** *340*, 148-154.

183. Wang, Y.; Zhao, Q.; Han, N.; Bai, L.; Li, J.; Liu, J.; Che, E.; Hu, L.; Zhang, Q.; Jiang, T.; Wang, S. Mesoporous Silica Nanoparticles in Drug Delivery and Biomedical Applications. *Nanomedicine : nanotechnology, biology, and medicine* **2015,** *11*, 313-327.

184. He, Q.; Shi, J. Msn Anti-Cancer Nanomedicines: Chemotherapy Enhancement, Overcoming of Drug Resistance, and Metastasis Inhibition. *Adv. Mater.* **2014,** *26*, 391-411.

185. Slowing, I. I.; Trewyn, B. G.; Giri, S.; Lin, V. S. Y. Mesoporous Silica Nanoparticles for Drug Delivery and Biosensing Applications. *Adv. Funct. Mater.* **2007,** *17*, 1225-1236.

186. Yang, P.; Gai, S.; Lin, J. Functionalized Mesoporous Silica Materials for Controlled Drug Delivery. *Chem. Soc. Rev.* **2012,** *41*, 3679-3698.

187. Tarn, D.; Ashley, C. E.; Xue, M.; Carnes, E. C.; Zink, J. I.; Brinker, C. J. Mesoporous Silica Nanoparticle Nanocarriers: Biofunctionality and Biocompatibility. *Acc. Chem. Res.* **2013,** *46*, 792-801.

188. Lu, F.; Wu, S.-H.; Hung, Y.; Mou, C.-Y. Size Effect on Cell Uptake in Well-Suspended, Uniform Mesoporous Silica Nanoparticles. *Small* **2009,** *5*, 1408-1413.

189. Trewyn, B. G.; Nieweg, J. A.; Zhao, Y.; Lin, V. S. Y. Biocompatible Mesoporous Silica Nanoparticles with Different Morphologies for Animal Cell Membrane Penetration. *Chem. Eng. J.* **2008,** *137*, 23-29.

190. Slowing, I.; Trewyn, B. G.; Lin, V. S. Y. Effect of Surface Functionalization of Mcm-41-Type Mesoporous Silica Nanoparticles on the Endocytosis by Human Cancer Cells. *J. Am. Chem. Soc.* **2006,** *128*, 14792-14793.

191. Huang, X.; Li, L.; Liu, T.; Hao, N.; Liu, H.; Chen, D.; Tang, F. The Shape Effect of Mesoporous Silica Nanoparticles on Biodistribution, Clearance, and Biocompatibility in Vivo. *ACS Nano* **2011,** *5*, 5390-5399.

192. Huang, X.; Teng, X.; Chen, D.; Tang, F.; He, J. The Effect of the Shape of Mesoporous Silica Nanoparticles on Cellular Uptake and Cell Function. *Biomaterials* **2010,** *31*, 438-448.

193. Chauhan, V. P.; Popović, Z.; Chen, O.; Cui, J.; Fukumura, D.; Bawendi, M. G.; Jain, R. K. Fluorescent Nanorods and Nanospheres for Real-Time in Vivo Probing of Nanoparticle Shape-Dependent Tumor Penetration. *Angew. Chem. Int. Ed.* **2011,** *50*, 11417-11420.

194. Agarwal, R.; Singh, V.; Jurney, P.; Shi, L.; Sreenivasan, S. V.; Roy, K. Mammalian Cells Preferentially Internalize Hydrogel Nanodiscs over Nanorods and Use Shape-Specific Uptake Mechanisms. *Proc. Natl. Acad. Sci. U. S. A.* **2013,** *110*, 17247-17252.

195. Godin, B.; Chiappini, C.; Srinivasan, S.; Alexander, J. F.; Yokoi, K.; Ferrari, M.; Decuzzi, P.; Liu, X. Discoidal Porous Silicon Particles: Fabrication and Biodistribution in Breast Cancer Bearing Mice. *Adv. Funct. Mater.* **2012,** *22*, 4225-4235.

196. Quignard, S.; Masse, S.; Laurent, G.; Coradin, T. Introduction of Disulfide Bridges within Silica Nanoparticles to Control Their Intra-Cellular Degradation. *Chem. Commun.* **2013,** *49*, 3410-3412.

197. Xu, Z.; Zhang, K.; Liu, X.; Zhang, H. A New Strategy to Prepare Glutathione Responsive Silica Nanoparticles. *RSC Adv.* **2013,** *3*, 17700-17702.

198. Maggini, L.; Cabrera, I.; Ruiz-Carretero, A.; Prasetyanto, E. A.; Robinet, E.; De Cola, L. Breakable Mesoporous Silica Nanoparticles for Targeted Drug Delivery. *Nanoscale* **2016,** *8*, 7240-7247.

199. Croissant, J.; Cattoën, X.; Man, M. W. C.; Gallud, A.; Raehm, L.; Trens, P.; Maynadier, M.; Durand, J.-O. Biodegradable Ethylene-Bis(Propyl)Disulfide-Based Periodic Mesoporous Organosilica Nanorods and Nanospheres for Efficient in-Vitro Drug Delivery. *Adv. Mater.* **2014,** *26*, 6174-6180.

200. Chen, Y.; Meng, Q.; Wu, M.; Wang, S.; Xu, P.; Chen, H.; Li, Y.; Zhang, L.; Wang, L.; Shi, J. Hollow Mesoporous Organosilica Nanoparticles: A Generic Intelligent Framework-Hybridization Approach for Biomedicine. *J. Am. Chem. Soc.* **2014,** *136*, 16326-16334.

201. Prasetyanto, E. A.; Bertucci, A.; Septiadi, D.; Corradini, R.; Castro-Hartmann, P.; De Cola, L. Breakable Hybrid Organosilica Nanocapsules for Protein Delivery. *Angew. Chem. Int. Ed.* **2016,** *55*, 3323-3327.

202. Corma, A.; Díaz, U.; Arrica, M.; Fernández, E.; Ortega, Í. Organic–Inorganic Nanospheres with Responsive Molecular Gates for Drug Storage and Release. *Angew. Chem. Int. Ed.* **2009,** *48*, 6247-6250.

203. Patarin, J.; Lebeau, B.; Zana, R. Recent Advances in the Formation Mechanisms of Organized Mesoporous Materials. *Curr. Opin. Colloid Interface Sci.* **2002,** *7*, 107-115.

204. Wan, Y.; Zhao On the Controllable Soft-Templating Approach to Mesoporous Silicates. *Chem. Rev.* **2007,** *107*, 2821-2860.

205. Anderson, M. T.; Martin, J. E.; Odinek, J. G.; Newcomer, P. P. Effect of Methanol Concentration on Ctab Micellization and on the Formation of Surfactant-Templated Silica (Sts). *Chem. Mater.* **1998,** *10*, 1490-1500.

206. Li, W.; Han, Y.-C.; Zhang, J.-L.; Wang, B.-G. Effect of Ethanol on the Aggregation Properties of Cetyltrimethylammonium Bromide Surfactant. *Colloid J.* **2005,** *67*, 159-163.

207. Leberman, R. The Hofmeister Series and Ionic Strength. *FEBS Lett.* **1991,** *284*, 293-294.

208. Gamcsik, M. P.; Kasibhatla, M. S.; Teeter, S. D.; Colvin, O. M. Glutathione Levels in Human Tumors. *Biomarkers* **2012,** *17*, 671-691.

209. Jang, H.; Ryoo, S.-R.; Kostarelos, K.; Han, S. W.; Min, D.-H. The Effective Nuclear Delivery of Doxorubicin from Dextran-Coated Gold Nanoparticles Larger Than Nuclear Pores. *Biomaterials* **2013,** *34*, 3503-3510.

210. Zeman, S. M.; Phillips, D. R.; Crothers, D. M. Characterization of Covalent Adriamycin-DNA Adducts. *Proc. Natl. Acad. Sci.* **1998,** *95*, 11561-11565.

211. Lucey, B. P.; Nelson-Rees, W. A.; Hutchins, G. M. Henrietta Lacks, Hela Cells, and Cell Culture Contamination. *Arch. Pathol. Lab. Med.* **2009,** *133*, 1463-1467.

212. Stayton, I.; Winiarz, J.; Shannon, K.; Ma, Y. Study of Uptake and Loss of Silica Nanoparticles in Living Human Lung Epithelial Cells at Single Cell Level. *Anal. Bioanal. Chem.* **2009,** *394*, 1595-1608.

213. Greco, A.; Maggini, L.; De Cola, L.; De Marco, R.; Gentilucci, L. Diagnostic Implementation of Fast and Selective Integrin-Mediated Adhesion of Cancer Cells on Functionalized Zeolite L Monolayers. *Bioconjugate Chem.* **2015,** *26*, 1873-1878.

214. Sun, C.; Sze, R.; Zhang, M. Folic Acid-Peg Conjugated Superparamagnetic Nanoparticles for Targeted Cellular Uptake and Detection by Mri. *J. Biomed. Mater. Res. A* **2006,** *78A*, 550-557.

215. Wu, J.-M.; Zhang, T.-W. Photodegradation of Rhodamine B in Water Assisted by Titania Films Prepared through a Novel Procedure. *J. Photochem. Photobiol.* **2004,** *162*, 171-177.

216. Kennedy, D. C.; Grünstein, D.; Lai, C.-H.; Seeberger, P. H. Glycosylated Nanoscale Surfaces: Preparation and Applications in Medicine and Molecular Biology. *Chem. – Eur. J.* **2013,** *19*, 3794-3800.

217. Kennedy, D. C.; McKay, C. S.; Tay, L.-l.; Rouleau, Y.; Pezacki, J. P. Carbon-Bonded Silver Nanoparticles: Alkyne-Functionalized Ligands for Sers Imaging of Mammalian Cells. *Chem. Commun.* **2011,** *47*, 3156-3158.

218. Kehr, J.-C.; Zilliges, Y.; Springer, A.; Disney, M. D.; Ratner, D. D.; Bouchier, C.; Seeberger, P. H.; De Marsac, N. T.; Dittmann, E. A Mannan Binding Lectin Is Involved in Cell–Cell Attachment in a Toxic Strain of Microcystis Aeruginosa. *Mol. Microbiol.* **2006,** *59*, 893-906.

219. Thompson, K. J.; Harley, C. M.; Barthel, G. M.; Sanders, M. A.; Mesce, K. A. Plasmon Resonance and the Imaging of Metal-Impregnated Neurons with the Laser Scanning Confocal Microscope. *eLife* **2015,** *4*, e09388.